

Algorithm Theoretical Basis Document Version 2 (ATBDv2)



glaciers
cci

Prepared by: Glaciers_cci consortium
Contract: 4000101778/10/I-AM
Name: Glaciers_cci-D3.7_ATBDv2
Version: 1.3
Date: 17.09. 2013

Contact:
Frank Paul
Department of Geography
University of Zurich
Winterthurerstr. 190
CH-8057 Zurich
frank.paul@geo.uzh.ch

Technical Officer:
Stephen Plummer
ESA ESRIN



**University of
Zurich**^{UZH}



**UNIVERSITY
OF OSLO**



**University of
BRISTOL**



Document status sheet

Version	Date	Changes	Approval
0.3	07.07. 2012	Copy of ATBDv0 with thematic extensions	
0.4	24.07. 2012	Draft example of elevation change (ALT)	
0.5	28.08. 2012	All updates for each product included	
0.8	12.12. 2012	First feedback from TO integrated	
0.9	01.02. 2013	All contributions and TO feedback updated	
1.0	13.02. 2013	Final editing and approval	F. Paul
1.1	23.04. 2013	Copy of ATBDv1 with changes marked	
1.2	04.05. 2013	Revised version with edits integrated	F. Paul
1.3	17.09. 2013	Comments to revised version integrated	

The work described in this report was done under ESA contract 4000101778/10/I-AM. Responsibility for the contents resides with the authors that prepared it.

Author team:

Frank Paul (GIUZ), Francesca Ticconi, Andrew Shepherd (SEEL), Andreas Kääb, Christopher Nuth (GUIO), Thomas Nagler, Helmut Rott, Kilian Scharrer (Enveo), Tazio Strozzi (Gamma)

Glaciers_cci Technical Officer at ESA:
Stephen Plummer

Table of Contents

1. Executive Summary	4
2. Introduction	5
2.1 Purpose of this document	5
2.2 Background to the approaches	5
2.3 General remarks	6
3. Glacier area.....	7
3.1 Introduction.....	7
3.2 Scientific background	8
3.3 Description of available algorithms	12
3.4 Description of the algorithm chosen	17
3.5 Required input data and generated output.....	19
3.6 Error budget estimates and expected accuracy	19
3.7 Expected performance gains by future developments	20
4. Elevation changes from repeat altimetry	22
4.1 Introduction.....	22
4.2 Scientific background	22
4.3 Justification on the algorithm chosen.....	32
4.4 Mathematical algorithm development description.....	33
4.5 Description of the processing line.....	36
4.6 Input data and algorithm output	37
4.8 Error budget estimates	38
4.9 Practical considerations for implementation.....	39
5. Elevation changes from DEM differencing.....	40
5.1 Introduction.....	40
5.2 Scientific background on DEM generation.....	40
5.3 Elevation changes from multi-temporal DEMs	42
5.4 Description of the algorithm chosen	43
5.5. Input data and algorithm output	47
5.6 Error budget estimates	47
5.7 Expected accuracy.....	47
5.8 Practical considerations for implementation.....	48
6. Algorithms for Glacier Velocity	49
6.1 Introduction.....	49
6.2 Scientific background	51
6.3 Justification on the algorithm chosen.....	59
6.4 Processing line for optical data	61
6.5 Processing line for microwave data (SAR).....	66
6.6 Input data and algorithm output	69
6.7 Error budget estimates	70
6.8 Expected accuracy.....	71
6.9 Practical considerations for implementation.....	71
References	72
Abbreviations.....	80

1. Executive Summary

This document is the Algorithm Theoretical Basis Document version 2 (ATBDv2) of the Glaciers_cci project. It is an update of the former ATBDv1 with a focus of the algorithms applied in the prototype system. There were no changes applied for the glacier area product, but some small modifications were made for the other two products. For the elevation change from altimetry product we removed the description of radar altimeters and for the velocity product the InSAR method was removed. In each Chapter we provide an Introduction, a scientific background and a justification of the algorithm selected, before the algorithms are described in detail. A short description of the input and output data, error budget estimates, and practical considerations for their implementation are also given. More detailed descriptions of these topics can be found in the IODDv1 (Glaciers_cci, 2013b), the DPMv1 (Glaciers_cci, 2013c) and the UCRv1 (Glaciers_cci, 2013d).

For glacier area it was confirmed in the round robin that band-ratio based algorithms work best for glacier mapping and that the different interpretation of debris-covered glacier parts cause the largest uncertainties. To reduce the latter, the creation of illustrated guidelines is encouraged. Glacier elevation changes from DEM differencing highlights the importance of proper co-registration of the two DEMs and that care must be taken when different software products are used for the analysis as the interpretation of geolocation information might differ. Elevation changes from altimeters are best obtained along repeat tracks and from the optical (higher resolution) GLAS sensor. The radar altimeters have only poor spatial coverage and cannot be properly corrected in steeper terrain and were thus removed in this version. Glacier velocity can be derived from both optical and microwave sensors using in principle the same method (tracking). In particular the selection of an appropriate image matching window size and the subsequent filtering of the results requires attention in the pre- and post-processing stage. The tracking itself works more or less automatically and can be applied globally. InSAR techniques were disregarded for global-scale velocity determination, and have thus been removed from this version. For using this technique to create coherence images (for identification of debris-covered glaciers) we refer to the ATBDv1 (Glaciers_cci, 2013a).

2. Introduction

2.1 Purpose of this document

The document provides a detailed description of the selected algorithms chosen to generate FCDRs of the data products requested by the end-users. As the ATBDv1, the document is mainly structured along the Glacier_cci product types, i.e. glacier area mapping, glacier elevation change and glacier velocity. While glacier area and elevation changes from DEM differencing and altimetry have individual chapters, velocity as derived from optical and microwave data are summarized in one Chapter. There is thus some repetition of statements and the structure is not fully similar for both sensors. According to the Statement of Work (SoW), the ATBDv2 is an updated version of the ATBDv1 which provides a detailed description of the scientific background and theoretical justification for the algorithms developed and implemented. It includes:

- a description of the physics of the problem
- a definition of the scope of the algorithm
- a detailed mathematical description of the algorithm including error budget estimates
- the assumptions made for the design of the algorithm, and its limitations
- a definition of the input data required and the outputs generated
- an analysis of the computation resources needed
- practical considerations for algorithm test and validation, quality control and diagnostics,
- approaches for exception handling.

Due to the large methodological differences in generating the four products, the topics listed above are described differently for each product. However, all Chapters follow the same principle structure (section headings) to keep them comparable to some extent.

2.2 Background to the approaches

Using satellite data to derive **glacier outlines** over large regions or on a global scale from automated image classification techniques is a key recommendation (Tier 5) of the tiered glacier monitoring strategy of GTN-G (e.g. Haeberli, 2006). In view of the demand to further transform these outlines (contiguous ice masses) into a glacier inventory (individual glaciers with topographic attribute information), the application of modern geoinformatic techniques (using a GIS and DEMs) is required for efficient data processing (e.g. Käab et al., 2002; Paul et al., 2002). With the free availability (and in the case of Landsat already accurately orthorectified) satellite data from USGS combined with the free DEMs from SRTM, the ASTER GDEM, or national DEMs (e.g. NED, CDED), the principle accomplishment of this task is feasible (Paul, 2010). As clearly expressed in the URD (Glaciers_cci, 2011a), the most important task is to complete the global glacier inventory. Since the required technical specifications for the sensors used is described in the DARD (Glaciers_cci, 2011c), we here focus on the processing methods and what is required to understand their physical background.

Multi-temporal satellite elevation data provides an effective approach to continuously monitor glacier surfaces. Glacier **elevation changes** are often used to characterize glacier mass

balance variations, especially in remote areas where field measurements are difficult. Indeed, it is the large spatial and temporal coverage of satellite-derived elevation changes that increase the desirability and potential of this method for glacier monitoring. Elevation change of a glacier surface is, however, not directly transferrable into mass changes because the surface change is the result of both surface mass balance processes (accumulation, ablation or firn layer variability) and dynamical ice flux components: general downward flow, submergence in the accumulation area, and emergence in the ablation area. This makes the interpretation of short-term glacier elevation changes complicated. Therefore, the products created by `Glaciers_cci` will focus on uncorrected elevation change measurements as requested in the URD (`Glaciers_cci`, 2011a). However, a mean elevation change value per glacier entity is a product that is also requested and will thus be generated as well. Elevation changes are derived by two general approaches; (1) repeat altimetry (lidar) with a focus on repeat track measurements that have small spatial offsets, and (2) DEM differencing with a focus on the pre-processing of the DEM pairs. In both approaches, the detection of bias is essential and required corrections should be determined.

The generation of **glacier velocity** measurements from repeat satellite data is highly desirable in the glaciological community to better characterize glacier dynamics and potential changes in the dynamic behaviour of glaciers. Since in-situ measurements of velocity are limited in space due to logistical constraints of deploying GPS instruments, satellite derived velocities provide an significantly larger spatial data set, both in terms of the number of glaciers that can be measured but also providing the spatial distribution of velocity within an individual glacier. Tracking methods based on repeat optical or SAR satellite images are efficient approaches to derive surface displacements on glaciers. A large variety of tracking algorithms were investigated in the round robin (e.g. normalized cross-correlation, cross-correlation operated in the Fourier domain, least squares matching, phase correlation, orientation correlation) and two of them were finally selected as the most appropriate. Based on the results of the round robin, also the key pre- and post-processing steps are described for both sensor types.

2.3 General remarks

A major guideline for the algorithms and processing chains described in this document is a high potential for automation. However, it should be mentioned that in many cases at least some degree of human interaction is required to derive glaciologically meaningful and reliable data of glacier areas, elevation changes and velocities. For instance, automatic glacier outlines have to be checked and corrected for debris-covered glacier parts, or some remaining velocity outliers have to be corrected manually, depending on the purpose of the application. In these cases, the goal of the algorithms and processing chains included here is to minimize the degree of human interaction and to support this interaction as much as possible. In the round robin, some of these interactions from analysts were evaluated for their impact on the quality of the result. Whenever we refer to the round robin, please check the [PVASR](#) (`Glaciers_cci`, 2012b) for details. As mentioned in section 1, version 2 of the ATBD has been shortened compared to v1 to focus on the algorithms selected for the prototype. If information on other processing algorithms is required, we refer the reader to version 0 and 1 of the ATBD.

3. Glacier area

3.1 Introduction

Compared to the use of aerial photography for glacier mapping in the World Glacier Inventory (WGMS, 1989), the application of satellite data has the special advantage of the much larger area covered combined with a sensor in the shortwave infrared (SWIR) that allows the automated classification of clean to slightly dirty (i.e. optically thin) glacier ice (e.g. Paul and Kääb, 2005). Of course, the spatial resolution is an order of magnitude lower (10 to 30 m) compared to aerial photography (about 1 m), but the smallest glacier entity that can still be called glacier (about 0.01 km² in size according to Paul et al., 2009) can still be mapped under good conditions (Andreassen et al., 2008). So in times of rapidly shrinking glaciers the gain in processing speed is really an asset. Under special circumstances it might even be possible to map nearly all glaciers of an entire mountain range within a few weeks, like for the Alps in the summer of 2003 (Paul et al., 2011) or for the western Himalaya within 3 years (Frey et al., 2012). Compared to the 30-year time span that was required to map all glaciers in the Alps in the previous inventory (Zemp et al., 2008), this is an important benefit, in particular for large scale hydrologic modelling (e.g. Zappa and Kan, 2007; Huss, 2011). So the most efficient means for repeat mapping of glaciers on a global scale is indeed provided by satellite data.

So far, 'satellite data' refers to optical data with a number of multispectral bands in various parts of the electromagnetic spectrum (from the visible to the thermal infrared). Though the SWIR band (e.g. TM5 on Landsat) allows discrimination of snow from clouds, none of the optical bands can penetrate through clouds, i.e. apart from seasonal snow cover, clouds are a major bottleneck in the operational application of satellite data for glacier mapping. If a scene has clouds over the glaciers to be analysed, the scene has to be excluded or can only partly be processed. In the latter case, the use of multi-temporal datasets might help, as usually the clouds in two, otherwise very good images are often not located at the same position. This gives the possibility to merge two data sets to get a (more or less) cloud free coverage (e.g. Le Bris et al., 2011). However, when cloud boundaries cover only parts of a glacier the issue can get rather complicated as the outline of one glacier entity might then refer to different years.

The other bottleneck is debris cover on glaciers that has the same spectral properties as the surrounding terrain and can thus not be discriminated from multispectral data alone. Though a number of techniques for debris-cover mapping have been developed in the recent past (e.g. Paul et al., 2004; Shukla et al. 2011), they all require manual post-processing to give sufficiently accurate results. With microwave data cloud penetration is not a problem, but the dielectric properties of ice and snow are not sufficiently different from other terrain to precisely map glacier extent automatically (e.g. Hall et al., 2000). However, the recent application of coherence images from ALOS PALSAR acquired during the summer months have revealed new possibilities to precisely delineate debris-covered glaciers in regions where image contrast is poor (e.g. Strozzi et al., 2010; Frey et al., 2012). For a part of Alaska even the entire delineation of glaciers from PALSAR coherence worked largely automatically (Atwood et al., 2010).

So in regard to clouds and debris-cover there is still potential for important algorithm improvements by considering also microwave data. When seasonal snow is present (and

hiding parts of the glacier perimeter), the only feasible option is to use a scene from another date. In some regions of the world this reduces the number of useful satellite scenes considerably (Paul et al., 2011), but in our experience product quality would otherwise be below acceptable standards.

Indeed, the best algorithms for automated classification of snow and ice produce results that are only different at the level of individual pixels (e.g. Paul and Kääb, 2005; Paul and Hendriks, 2010). The quality of the generated outlines does thus largely depend on the experience and qualification of the analysts responsible for the post-processing. Errors introduced by the wrong interpretation of debris cover, snow fields, or glacier parts in shadow are much larger than differences in the algorithms (Gjermundsen et al., 2011). For this reason a major task towards improved product quality and consistency is the generation of illustrated guidelines for the analyst. This should not exclude further advances in the automated classification and hence reduce the required post-processing, but in the end the analyst has to decide whether a glacier outline is acceptable or not. Statistical tests or standard error assessments do not provide this information.

3.2 Scientific background

In the following we focus on the main-processing stage, i.e. the glacier mapping algorithm to be applied. To find a most suitable algorithm, one has to be aware of what a glacier looks like, i.e. the spectral properties of the typical surface characteristics as seen from space. As glaciers result from the metamorphosis and compression of snow, their spectral properties are very similar to snow (e.g. Hall et al., 1988). Of course, dust, debris and liquid water on the surface alter the spectral response and can be found nearly anywhere on the glacier (Fig. 3.1). In this regard the spectral information of a satellite image pixel (in the 10-30 m range) is in most cases a mixed signal with the respective deviations from a pure (laboratory) signal. In Fig. 3.2a and 3.2b a comparison of the spectral reflectance for snow of varying grain size from theoretical considerations (Dozier, 1989) with field-based measurements from Quanzhu et al. (1983) is shown. Besides the high reflectance of snow in the visible part (VIS) of the spectrum (independent of grain size), the strong reflectance drop in the near infrared (NIR) can be seen (Fig. 3.2a). The dependence of the reflectance on grain size is very high in the NIR (with smaller grains having the higher reflectance), indicating the potential to map snow grain size from the reflectance value in this spectral range. In the SWIR the reflectance increases slightly again and is still strongly dependent on grain size (Fig. 3.2). On the other hand, clouds still have a rather high reflectance in the SWIR and thus can be easily discriminated from snow with a SWIR sensor (Dozier, 1989).

In a spectral sense, glacier ice can be seen as snow with very large grain sizes, so that the spectral reflectance curve of pure glacier ice follows the curve of snow very closely. However, impurities in and on the ice (e.g. dust and soot) shift the curve of spectral reflectance downwards (Fig. 3.2b). The spectral reflectance curve of debris is based on the lithology of the material and can thus have any shape.

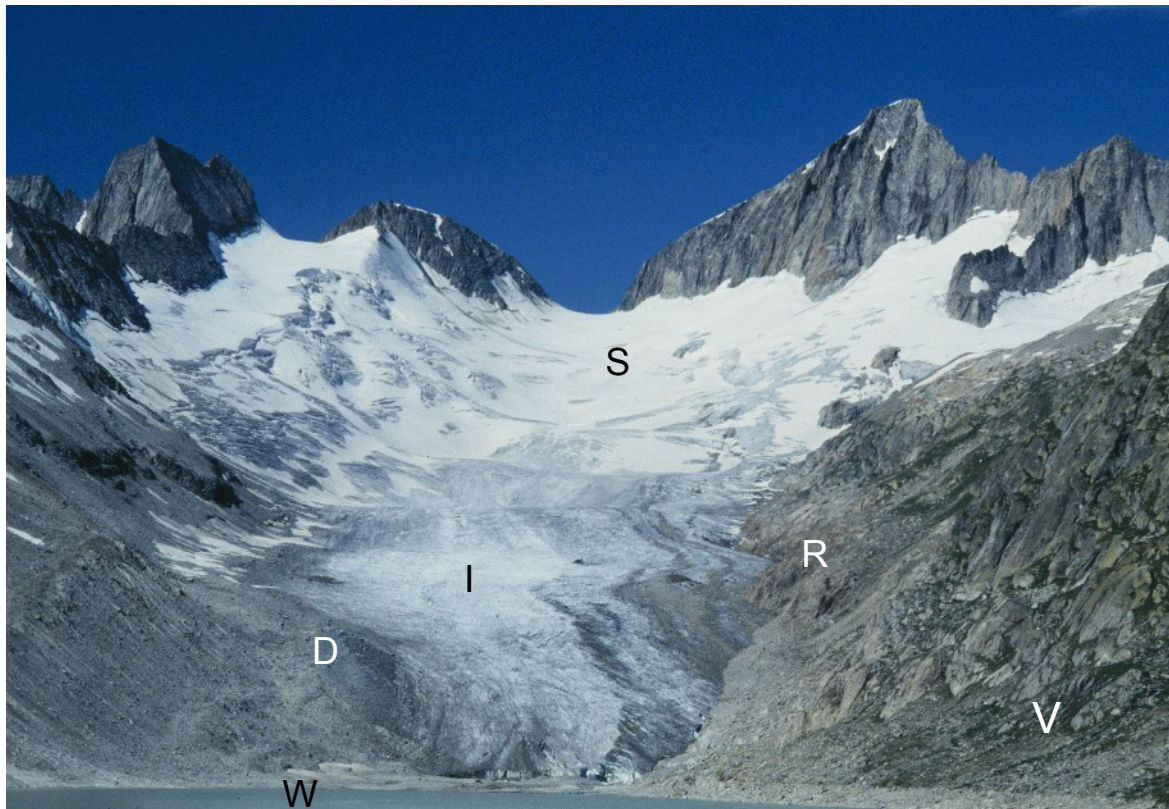


Fig. 3.1: Oberaarglacier in Switzerland. The picture illustrates the spectral reflectance of bare ice (I), debris-covered ice (D), snow (S), rock (R), vegetation (V) and turbid water (W) in the visible part of the spectrum. A spectral discrimination of the debris cover on the glacier and from the lateral moraine (in the lower left of the image) is not possible.

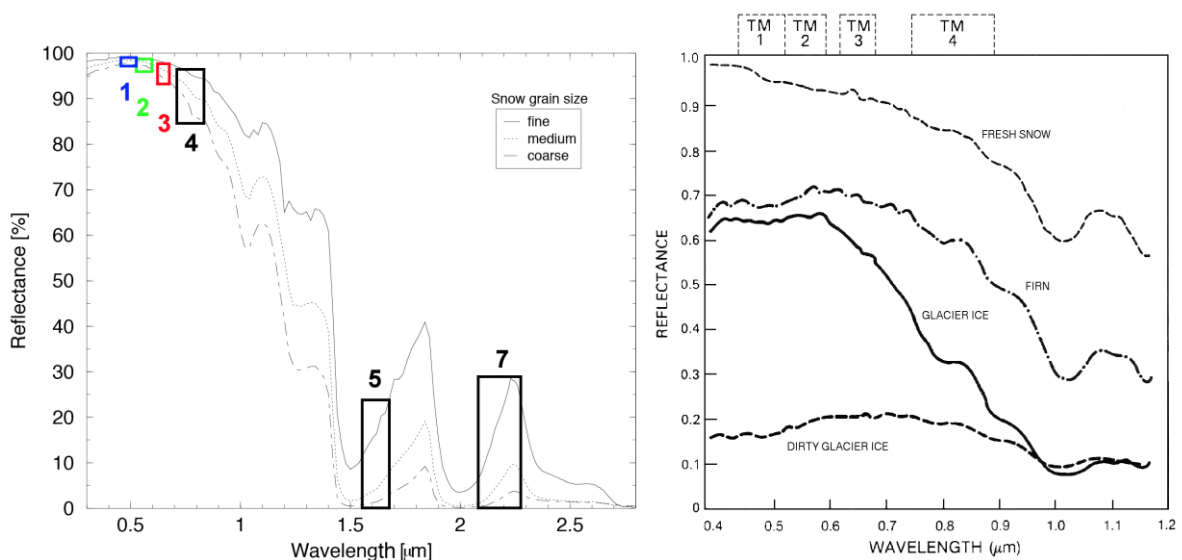


Fig. 3.2: Modelled spectral reflectance curves of snow with three different grain sizes and position of TM spectral bands (left). Spectral reflectance of snow, firn, ice and dirty glacier ice according to field measurements (right). The data for the left figure are taken from the ASTER spectral library (JPL, 2002), the right figure is adapted from Hall et al. (1988).

Apart from the above components, shadow on the glacier surface alters its spectral response as atmospheric scattering (brightening these regions) is dependent on wavelength. The same is true for thin clouds (cirrus or fog). A high impact on the absolute reflectance values results from illumination differences due to the topography (i.e. the sun - target - sensor geometry) and to a lesser extent from atmospheric conditions. The use of absolute reflectance values for glacier classification therefore requires topographic and atmospheric corrections (e.g. Rott and Markl, 1989).

The spectral reflectance of glaciers in the individual spectral bands is shown in Fig. 3.3 for the Landsat TM sensor (ASTER and SPOT look similar, but do not have a TM band 1 equivalent band in the blue part of the spectrum) for a typical high-mountain region with glaciers (cf. Paul, 2002). In agreement with the spectral curves shown in Fig. 3.2, the high reflectance over snow in the VIS to NIR (VNIR) bands (TM1, TM2, TM3, TM4) and the lower reflectance over glacier ice can be seen. In the NIR the low reflectance of water and the higher reflectance of vegetation become obvious. The very low reflectance of glacier ice and snow in the SWIR can be seen in TM 5 and TM 7 (not shown here). The reflectance of water is also very low and vegetation and rock have a very high surface reflectance. Finally, the digital numbers (DNs) in the thermal infrared band (TIR) of TM6 depend on surface temperature. They are thus related to surface emission rather than reflectance. The higher the temperature is, the higher the DNs are and vice versa. Hence, glacier ice and snow (at the melting point) have rather low DNs, whereas sunlit mountain slopes are already warmed at the time of image acquisition and appear much brighter. Terrain in shadow is also cooler and thus appears somewhat darker. Most noticeable is the much coarser resolution (120 m) of TM band 6 (ETM+: 60 m, ASTER: 90 m) compared to the other bands.

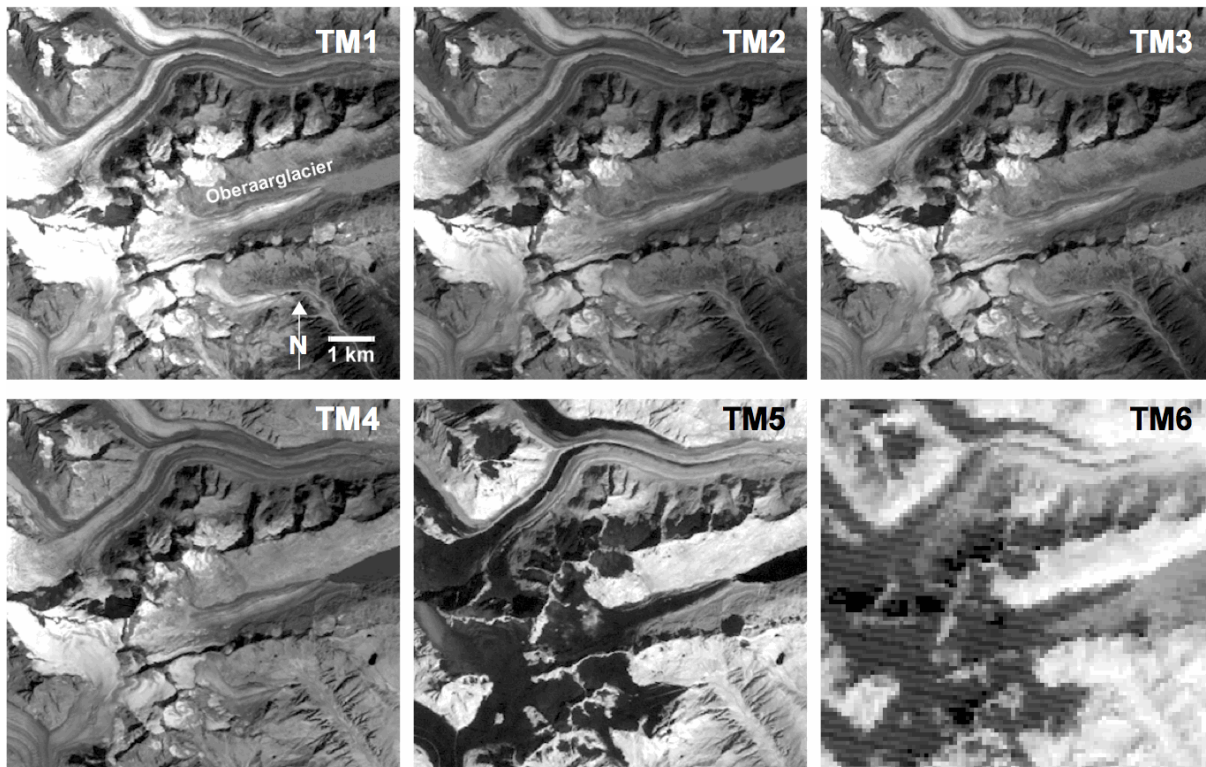


Fig. 3.3: Visualization of reflectance values in TM bands 1 (TM1) to 6 (TM6) for a subset of a Landsat TM scene around Oberaarglacier in the Swiss Alps (image size is 9.5 km by 9 km).

The thermal band was proposed in various publications as being useful to delineate debris-covered glacier parts, due to the cooling of the rocks on the surface from the underlying ice (e.g. Shukla et al., 2011 and references therein). However, we are sceptical that this really works for alpine type glaciers. In most cases some bare ice is included in the related mixed pixels (strongly reducing the temperature of the respective pixel) and the effect of differential thermal heating of the rocks by the sun is rather obvious. However, in the case of a (thin) volcanic ash layer and comparably large glaciers (e.g. the Vatnajökull icecap on Iceland), the thermal band could be used as an alternative to the SWIR band (Bishop et al., 2004), i.e. all glacier ice and snow has a similar low reflectance (independent of the ash cover).

The different spectral responses of ice and snow compared to other surface types (water, rock, vegetation) or clouds, allows them to be classified automatically (see section 3.3). However, in the post-processing stage omission and commission errors have to be corrected (e.g. adding debris cover or glacier parts in shadow, removing lakes). For this purpose contrast enhanced RGB composites are created from the different spectral bands that are used in the background to guide the correction process (see examples in Fig. 3.4). The most useful combinations in this regard are the classical band 3, 2, 1 (natural colours with TM) and 4, 3, 2 (false colour infrared) combination, as well as the band 5, 4, 3 false colour composite (FCC). While the 321 composite is best suited to identify ice and snow in shadow, the 432 composite has best contrast to identify water surfaces, vegetation trimlines, snow cover and drainage divides in the accumulation region. The 543 FCC allows a clear identification of glaciers (they appear in light blue), helps to identify clouds (which appear white) and provide good contrast for debris cover identification. Thus all three band combinations are useful and should be generated in the pre-processing stage from the raw data using digital image processing software.

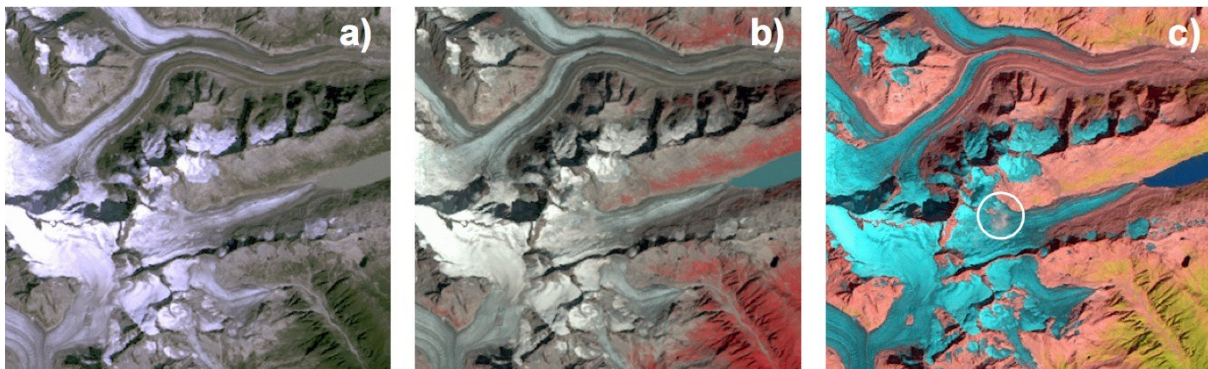


Fig. 3.4: RGB composites of the region shown in Fig. 3.3 with a) bands TM 3, 2, and 1, b) 4, 3, 2, and c) 5, 4, 3. The small cloud is only visible in this image (white circle).

The algorithms presented in the following sections are based on raw DN_s, i.e. they are not converted to top-of-atmosphere (TOA) reflectance values or corrected for topographic or atmospheric effects. The main reasons are: (a) the latter requires a DEM that has no artefacts and is perfectly aligned with the satellite image. This is nearly impossible to achieve, as the registration error of satellite images is seldom better than ± 1 pixel (RMSE), in particular in steep high-mountain terrain. Without a proper coregistration, artefacts are introduced to the reflectance values during topographic correction (e.g. due to over correction), which reduce the quality of the classification. At the same time a 'perfect' topographic correction would

remove subtle reflectance differences that are important to classify glaciers accurately (e.g. in shadow). (b) Atmospheric correction requires a number of atmospheric parameters being available (at least visibilities at different altitudes) which is often not the case in remote regions where glaciers are found. (c) The most accurate mapping methods are based on band ratios. They partially normalize topographic and atmospheric conditions within a scene and thus work without this pre-processing step. Using TOA reflectance instead of DN_s does not improve the classification so this conversion is not required either (Paul, 2001).

3.3 Description of available algorithms

A wide range of glacier classification methods have been developed and compared in the past two decades (e.g. Albert, 2002; Paul et al. 2003; Sidjak and Wheate, 1999). They range from manual delineation to simple band ratios (e.g. Bayr et al., 1994; Jacobs et al., 1997; Paul 2002), to more complex band ratios such as the Normalized Difference Snow Index (NDSI) (e.g. Racoviteanu, 2008), and supervised classification techniques like spectral end members (Klein and Isacks, 1999), maximum likelihood classifiers (Aniya et al., 1996), principal component analysis (PCA) (Sidjak and Wheate, 1999) or fuzzy set theory (e.g. Binaghi et al., 1997). For (operational) glacier mapping on a global scale, the algorithm to be applied must be simple (in terms of the required pre-processing), accurate (compared to a reference data set and/or other algorithms), and robust (transferable to other regions without changing too many of the parameters). Hence, a high pre-processing workload is only justifiable when the results are much better than with less demanding algorithms. In this regard all supervised (e.g. selection of training areas or end members) or scene dependent methods (e.g. PCA) mentioned above are too demanding (see Albert (2002) for a detailed comparison) and are not considered further.

For the same reason, band ratios have become a quasi-standard for glacier mapping in the past decade (e.g. Racoviteanu et al. 2008), given that a SWIR band is available. When only panchromatic or false colour infrared images are available, only manual delineation of the glacier outlines can be applied. However, despite the often much higher resolution of the related panchromatic images (e.g. from aerial photography or high resolution satellite sensors), this could be much more error prone than glacier mapping with a lower resolution SWIR band. The example in [Fig. 3.5](#) illustrates this problem for the Waxeggkees in the Zillertaler Alps (Austria), where the surrounding rock has the same spectral reflectance in the VIS as bare ice. As manual delineation needs to be applied in the post-processing stage in any case, we focus in the following on the description of the band ratios. The characteristics of the three most often applied band ratio classifiers is provided in [Table 3.1](#).

The band ratio method is based on the division of the (high) DN_s over ice and snow in the red band by the low DN_s in the SWIR yielding high values over glaciers and low values elsewhere. Using a simple threshold the resulting ratio image can be segmented into glacier (black) and other terrain (white). This works for all ratios, either red/SWIR, NIR/SWIR or the NDSI: $(\text{green} + \text{SWIR}) / (\text{green} - \text{SWIR})$. As an example for the red/SWIR band ratio (e.g. TM3/TM5) the algorithm in pseudo code is:

```
IF (red/SWIR) > thr THEN glacier ELSE other
```

The threshold ‘thr’ is often close to 1.8 (+/-0.2) for this band combination. Depending on the software used, the implementation of the algorithm might look slightly different.



Fig. 3.5: Screenshot from GoogleMaps showing the Waxeggkees in the Zillertaler Alps (Austria). The glacier is nearly invisible in this natural colour image, indicating that a high spatial resolution alone is not always sufficient to accurately map glaciers.

Unfortunately, certain adjustments have to be made to all band ratios. An additional threshold in the blue (TM1) or green (AST1) band is required to improve the often occurring misclassification of rocks in shadow when using the red/SWIR ratio. The latter is due to the atmospheric scattering that is still present in the red band and brightens bare rock in shadow similar to ice in shadow. Band 1 is highly sensitive to atmospheric scattering and is strongly reflected from snow. Snow and ice in shadow is thus in general much brighter than rock in shadow and can be separated by a threshold (Paul and Kääb, 2005).

This correction is not required for the NIR/SWIR ratio as atmospheric scattering (or path radiance) is very low in the NIR. However, the high reflectivity of vegetation in the NIR often results in a misclassification of vegetation in shadow. This can be removed by additionally classifying vegetation, for example using the Normalized Difference Vegetation Index (NDVI). Of course, this step might not apply in regions without vegetation and it has to be considered on a case-by-case basis if red/SWIR or NIR/SWIR gives the better results (e.g. Andreassen et al., 2008; Paul and Kääb, 2005).

The NDSI has problems in regions with cast shadow as the high path radiance present in the green band needs to be subtracted before the NDSI is applied. The lowest DN in the respective scene can be found by histogram analysis and must then be subtracted from all DNs. This method is also named Dark Object Subtraction (DOS) in the literature (Chavez et al., 1988). The results are then very similar to the red/SWIR ratio (cf. Paul and Kääb, 2005).

<i>Abbreviation</i>	BR RS
<i>Algorithm</i>	Band Ratio with the red and SWIR bands (e.g. TM3/TM5)
<i>Reference</i>	Paul et al. (2003)
<i>Applications</i>	Paul and Kääb (2005), Andreassen et al. (2008), Paul et al. (2009)
<i>Description</i>	Strong differences in spectral reflectance of ice and snow in the SWIR compared to other terrain and the VNIR bands allows their automated classification (clean to slightly dirty glacier ice) from a simple band ratio.
<i>Advantages</i>	- The algorithm is very simple and the thresholds are robust, i.e. the result is not very sensitive on the exact value and a best value can easily be found.
<i>Disadvantages</i>	- Rock in shadow and turbid lakes are also mapped - An additional threshold in band TM1 is required to improve the shadow classification and wrong lakes need to be removed
<i>Improvements</i>	The thresholds have to be determined interactively, an automated determination of both thresholds should be developed
<i>Abbreviation</i>	BR NS
<i>Algorithm</i>	Band Ratio with the NIR and SWIR bands (e.g. TM4/TM5)
<i>Reference</i>	Paul et al. (2003), Paul and Kääb (2005)
<i>Applications</i>	Paul et al. (2002), Paul (2002), Jacobs et al. (1997), Bayr et al. (1994)
<i>Description</i>	Strong differences in spectral reflectance of ice and snow in the SWIR compared to other terrain and the VNIR bands allows their automated classification (clean to slightly dirty glacier ice) from a simple band ratio.
<i>Advantages</i>	- The algorithm is very simple and the thresholds are robust, i.e. the result is not very sensitive on the exact value and a best value can easily be found. - Is less sensitive to lakes
<i>Disadvantages</i>	- also maps vegetation (in shadow) that requires an additional threshold - sometimes misses ice in shadow
<i>Improvements</i>	The threshold has to be determined interactively, might be merged with BR RS
<i>Abbreviation</i>	NDSI
<i>Algorithm</i>	Ratio with the green and SWIR bands (e.g. (TM2+TM5)/(TM2-TM5))
<i>Reference</i>	Paul and Kääb (2005)
<i>Applications</i>	Racoviteanu et al. (2008)
<i>Description</i>	Strong differences in spectral reflectance of ice and snow in the SWIR compared to other terrain and the VNIR bands allows their automated classification (clean to slightly dirty glacier ice) from a simple band ratio.
<i>Advantages</i>	None compared to BR RS and BR NS (i.e. results are the same)
<i>Disadvantages</i>	- All rock in shadow and turbid lakes are also mapped when DOS is not applied to the green band before the ratio - Histogram analysis has to be performed manually
<i>Improvements</i>	All thresholds have to be determined interactively, an automated determination of both thresholds should be developed

Table 3.1: Details of the algorithms used for glacier mapping. Glaciers_cci will preferably use BR RS and sometimes also BR NS for data production.

To a variable extent, all of the above methods misclassify turbid lakes as glaciers. While there is some potential to also classify lakes automatically from multispectral information alone (e.g. Huggel et al., 2002) and thus remove them from the glacier map, there is some overlap with glaciers that can remove correctly classified glacier pixels. In this regard, the safest way is to manually select (by visual inspection of the satellite image) and delete the lake polygons at the post-processing stage (after vectorization of the outlines).

Finally, in some cases a correct spectral classification does not result in a correct classification of the object. For example, lakes on the surface of a glacier need to be included in the glacier area, whereas ice bergs or sea ice have to be excluded. This is currently most effectively performed in the vector domain of the post-classification stage.

From the comparison of the algorithms listed in [Table 3.1](#) it becomes clear that the threshold selection is the most critical step for the classification. Currently, the advice is (e.g. Racoviteanu et al., 2009) to select this threshold in a most sensitive region (shadow) in a way that the workload for post-processing is minimized. In most cases this means that a rather low value for the TM1 threshold is used to get all ice and snow in shadow properly included. At the same time this increases noise or misclassification at other places. However, these additional (often isolated pixels) either do not matter (e.g. over water) or can be later removed by a noise filter. In some cases it is not possible to include the ice in shadow in one part of the image without including all bare rock in shadow in another part of the image. This can happen as a consequence of special atmospheric conditions (e.g. haze or fog), that locally increases path radiance. In such a case two glacier masks with two different thresholds were created and digitally combined afterwards. In [Fig. 3.6](#) an example of such a dual classification from the Canadian Rockies is shown. The decision is based on visual inspection.

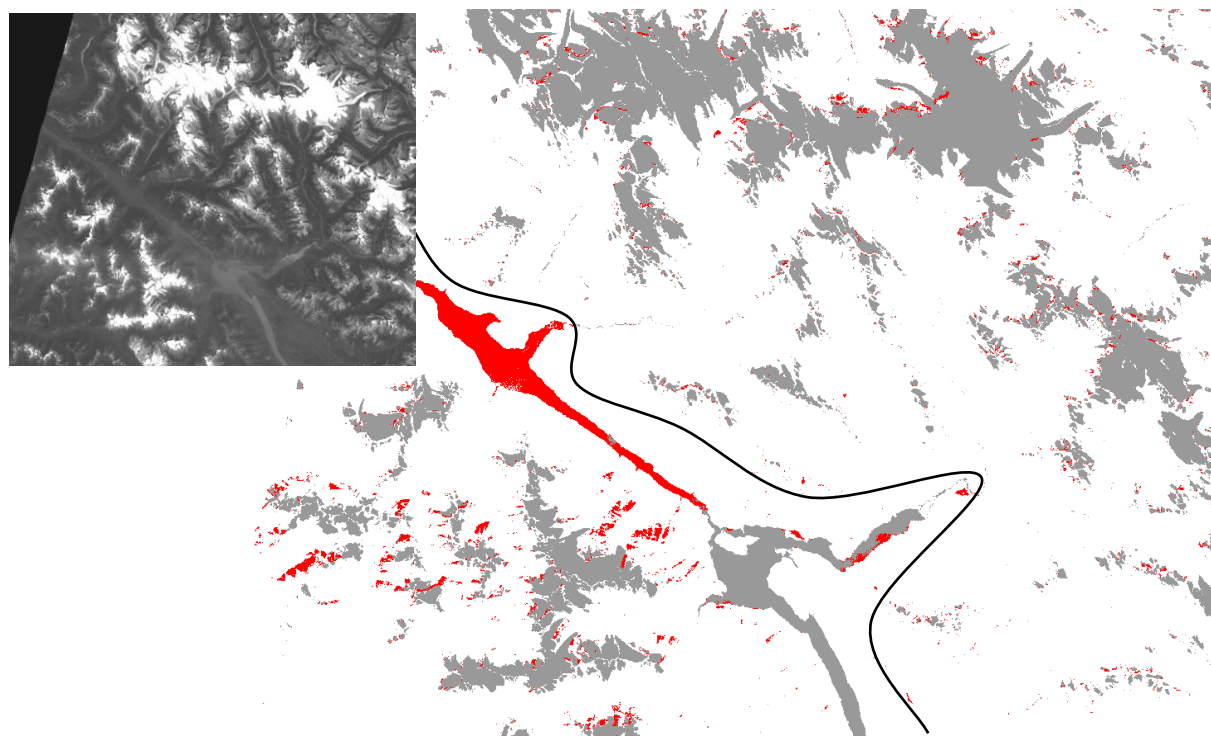


Fig. 3.6: Glaciers as mapped by two different thresholds. Red pixels were included below and excluded above the black line. The inset (TM 1) illustrates the subtle haze conditions.

A final processing step is the application of a noise filter (e.g. 3 by 3 median) to eliminate isolated pixels (e.g. snow patches) and close small gaps on a glacier (e.g. in shadow). Whether the application of this filter is really a benefit for the mapping or not has to be decided on a case-by-case basis. In Fig. 3.7 we demonstrate the sensitivity of the algorithm on the threshold value applied and the changes of the glacier map due to the application of a median filter (3 by 3 kernel size). The number of pixels added by lowering the threshold in steps of 0.1 is very small. Moreover they appear in regions that have to be carefully checked and often corrected anyway (debris-cover and shadow). In this regard the threshold value can be considered as robust and good results were likely achieved even with a fixed threshold value (around 1.9 in this case). With a threshold of 1.8 (all colours) already some isolated noisy pixels (red) appear. This indicates that the threshold value should not be much lower than this. The median filter efficiently closes isolated gaps (blue pixels in the right image of Fig. 3.7) but at the same time also deletes isolated pixels or small pixel clusters (red). As the latter are often related to isolated (seasonal) snow patches, this consequence is rather beneficial. However, in regions with many very small glaciers and no seasonal snow, it might be better to proceed with the raw glacier map (e.g. Paul et al., 2012).

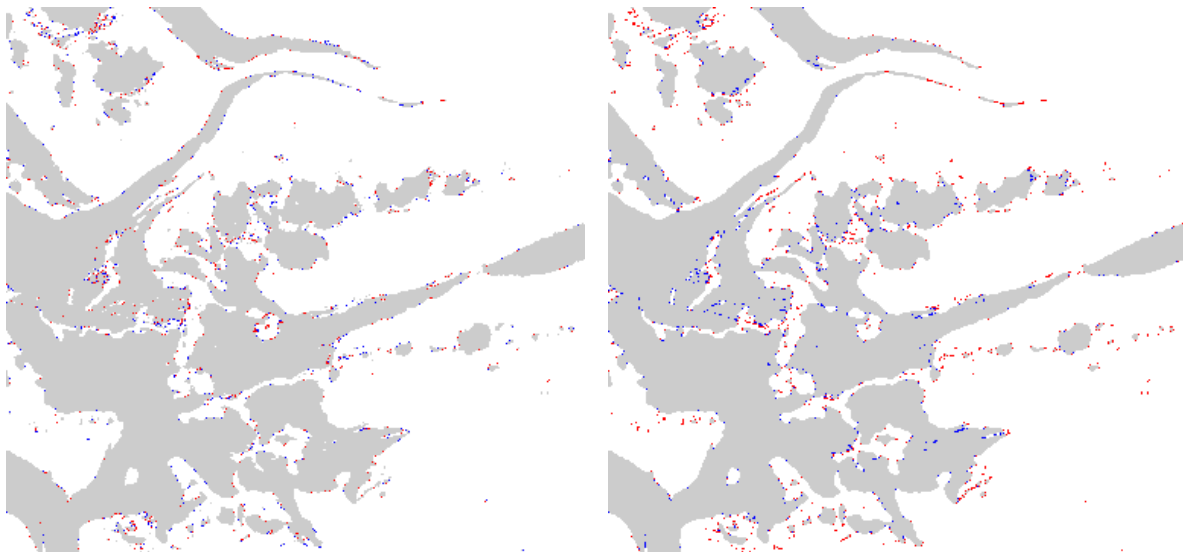


Fig. 3.7: Left: Three glacier maps combined resulting from three threshold values: 1.8 (all colours), 1.9: (grey and blue), 2.0 (grey). Right: Effect of a 3×3 median filter: red pixels are removed and blue pixels are added (shown here for the map with the threshold 1.9).

Applications in various regions of the world have shown that also glaciers under thin cirrus clouds (e.g. from aircraft contrails) or other optically thin clouds can be mapped with the TM3/TM5 band ratio (Paul and Andreassen, 2009). More difficult to map is bare ice in the shadow of convective clouds or deeply crevassed zones creating local shadows. For all these regions careful visual inspection and maybe correction of the generated outlines is required, using one of the above mentioned RGB composites in the background. The quality of this step depends on the contrast of the image and the skills of the analyst to interpret subtle features. In any case, the application of one of the above automated methods to map clean glacier ice is strongly recommended compared to a full manual digitization. The latter should be restricted to applying edits to the initial mapping.

3.4 Description of the algorithm chosen

3.4.1 Justification on the algorithm chosen

All algorithms described in [Table 3.1](#) were applied for glacier mapping by the participants of the round robin. Additionally, an ISODATA clustering algorithm was applied on the first 5 principal components. The overlay of the generated glacier outlines (Figs. 2.12 and 2.13 in [RD-9](#)) demonstrate that all of the applied algorithms perform equally well, i.e. they can only be discriminated at the level of individual pixels. In this regard, no preference can be given to any of the algorithms and the choice has to be made according to other criteria. For Glaciers_cci the BR RS method is chosen, i.e. a threshold applied to a band ratio with the red and shortwave infrared band (e.g. TM3/TM5) combined with an additional threshold in a blue or green band (e.g. TM1) to improve classification in cast shadow where required. A key reason for this selection is also the fast and easy processing and the related implementation in simple scripts. Three decisions have to be taken by an operator: (1) the threshold for the band ratio, (2) if an additional blue or green band should be applied and if yes, the threshold, and (3) if a median filter should be applied for smoothing or not. Once these have been determined, the algorithm can be applied to the raw data.

As the round robin clearly demonstrated, product quality for debris-covered glaciers is driven by the manual corrections applied. These differ largely among the analysts (in particular for debris cover and shadow) and will be difficult to homogenize. The way forward might be in the compilation of illustrated guidelines demonstrating for various examples around the world where to place the glacier boundary. Together with the engaged community, Glaciers_cci will aim at preparing such guidelines. They will be supported by examples from coherence images, which have demonstrated their potential to identify glacier ice under debris cover and persistent orographic clouds in high mountain regions (Atwood et al., 2010; Frey et al., 2012). As appropriate coherence images are not available for all regions and the processing is much more complex than the simple band ratio applied to the optical images for the mapping of clean ice, Glaciers_cci will process a larger number of them to control product quality in critical regions.

3.4.2 Mathematical description of the algorithm

Product generation from the raw data requires a pre-, main and post-processing stage (see [3.4.3](#)). We focus in this section on the main processing stage that is largely automatic. As described in section [3.3](#), the mathematical core of the algorithm is very simple, as just the raw DN's (converted to floating point for at least one of the bands) of two image bands have to be divided by each other (resulting in a ratio image) and a threshold has to be applied to convert the ratio image into a binary image (following the rule to minimize workload for manual editing). Together with the conversion of the original geotif (*etm230009_010820b1.tif*) to the grid format of the software (*imagegrid*), a ratio applied to the blue band (*k1gr*), the application of a median filter (*focalmedian*) to the resulting binary image and the subsequent raster to vector conversion (*gridpoly*), a script performing these steps (here in Arc Macro Language or AML coding for illustration) is looking like this:

```
imagegrid etm230009_010820b1.tif k1gr
imagegrid etm230009_010820b3.tif k3gr
imagegrid etm230009_010820b5.tif k5gr
grid
t = con((float(k3gr) / k5gr) > 1.8, 0, 255)
```

```

tt = con(t == 0 and k1gr > 45, 0, 255)
tmed = focalmedian(tt)
ttt = setnull(tmed == 255, 0)
q
gridpoly ttt glmap1
  
```

The analyst has to adjust the red numbers (1.8 and 45) in a text editor and run the script again until a satisfying result is achieved. Satisfying means that the workload for post-processing (i.e. correction of regions in cast shadow) is minimized. By writing the outlines to different filenames (*glmap1*, *glmap2*, ...), the improvements can be monitored (compared to a contrast enhanced version of the original satellite image) and the most appropriate threshold selected. When Landsat 7 ETM+ scenes in scanline corrector off mode are processed, a couple of scenes with missing lines located at different places can be processed and the resulting grids merged at the *tt* or *tmed* level (for a smooth transition) before the raster vector conversion.

3.4.3 Description of the processing line

A schematic overview of the entire processing line is presented in Fig. 3.8. In the pre-processing step appropriate satellite scenes (in regard to snow and cloud conditions) have to be selected from the quicklook catalogue, downloaded, converted to the file formats of the digital image processing software applied, and RGB composites (see Fig. 3.4) might be created. Then the algorithm is applied, the thresholds selected and the raw vector outlines are exported for post-processing at three further levels (L0, L1, L2) and GLIMS conversion.

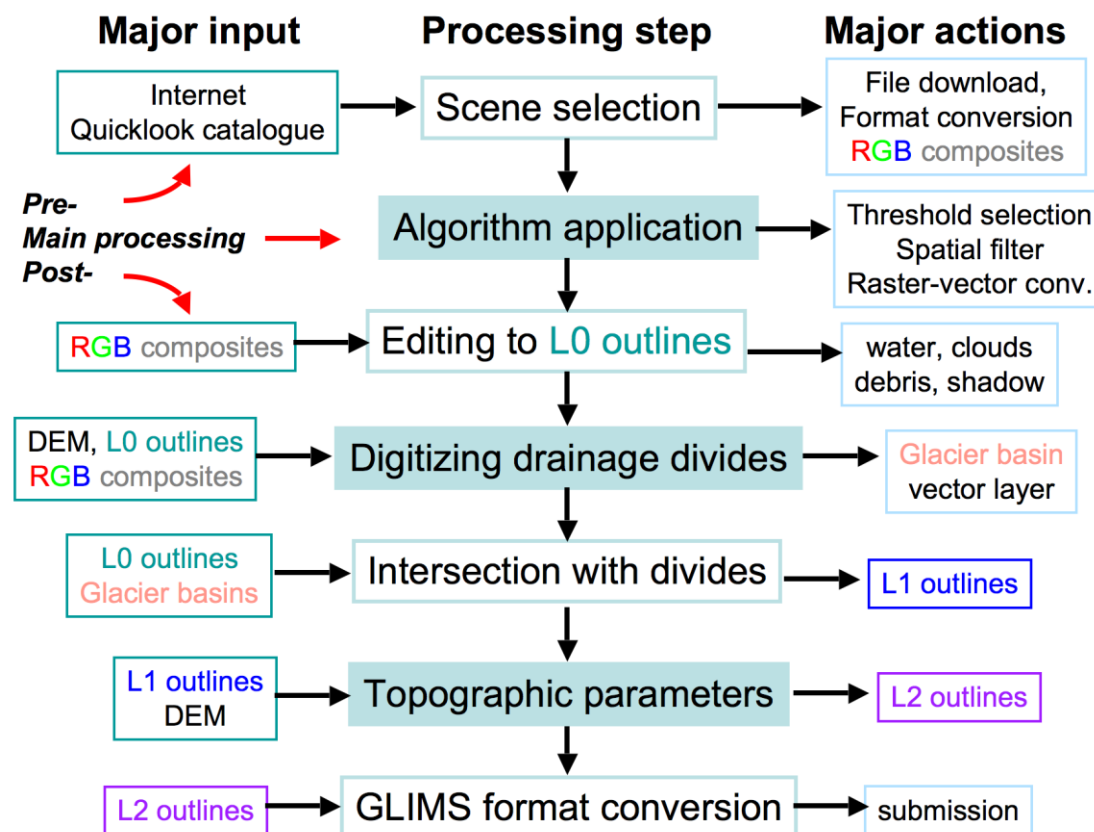


Fig. 3.8: Generalised processing work flow including the key steps of the pre- and post-processing. The main processing step ('Algorithm application') is described in section 3.3.

The post-processing of the raw glacier outlines is divided into four major steps: (a) correction of the outlines to L0 (e.g. wrongly classified, debris, water, shadow and clouds), (b) intersection with drainage divides to obtain glacier entities to L1, (c) calculation of topographic parameters for each glacier entity (L3), and (d) the conversion to the GLIMS format (and upload of the data to the GLIMS database). For steps (b) and (c) a DEM is required and additional scripts have to be applied.

3.5 Required input data and generated output

The input data required to generate the output with the algorithms described above are an orthorectified satellite scene (with at least the geometric accuracy of the L1T product from USGS) and a DEM. Further details are described in the DARD (Glaciers_cci, 2011c). While the satellite data are normally provided in Geotiff format, the DEMs use a variety of formats (bil, geotif, ascii, grid, etc.). As a starting point, these formats have to be converted to the storage format of the digital image processing and GIS software used. The next step is related to pre-processing work (e.g. creation of true and false colour composites, deriving hillshades, contour lines and drainage divides from the DEM), before one of the algorithms described above is applied in the main processing stage. The output is a binary raster map that is converted to the vector format before the editing in the post-processing stage can start. For this purpose the entire dataset is still in the UTM projection of the satellite scene(s) used as an input. The further processing follows the above four steps as in the GlobGlacier project.

To facilitate internal communication, a tiered terminology was developed to discriminate different levels of processing. These levels are not related to the processing levels of satellite data in general (e.g. as used by ESA), but just to help to be precise and short. The raw glacier outlines have level 0 (L0), outlines corrected for gross errors (e.g. water, sea ice, clouds) have L0a, and fully corrected outlines (debris, shadow and all other issues) have L0b. Deriving individual glaciers (L1) from the L0b outlines requires to digitally intersect the L0b outlines with drainage divides that need to be derived beforehand from the DEM. The digitization of drainage divides is time consuming as it requires manual work, but it has to be done only once. For the glacier inventory, the L1 outlines are digitally combined with a DEM to have topographic parameters for each glacier (L2 product). Finally, the outlines are converted to the GLIMS format and submitted.

Although the details of the data processing work-flow will vary with the software used to process the data, the major steps described in Fig. 3.8 are common to nearly all software products. While the main processing algorithm works largely automatically, the other steps require more intense intervention by the analyst. However, some automated (script-based) processing is available for some of them as well (e.g. deriving L2 from L1 outlines). It has to be noted that the intermediate products of Level 0 and 1 are also useful for some applications (e.g. computing the sea-level contribution of glaciers).

3.6 Error budget estimates and expected accuracy

3.6.1 Contributions to the error budget

When considering the final glacier outline product, errors are introduced at the pre, main and post-processing stage. The quantification of the respective errors require different measures and are sometimes difficult to assess. As a first step, we provide an overview on the potential error sources in [Table 3.2](#). From this table it becomes clear that the largest errors are

introduced in the post-classification stage. They could be up to one order of magnitude larger than errors caused by the algorithm or the mosaicing of scenes in UTM projection (e.g. when debris-cover is not included). This is indeed not the error that occurs when the debris cover is manually corrected. However, in this case other errors occur (generalization, inconsistent interpretation of mixed pixels) that can be determined by multiple digitizations. The magnitude of these errors was assessed in the round robin (Glaciers_cci, 2012b). The geolocation error has no direct effect on glacier size, but needs to be considered when the outlines are combined with a different DEM (e.g. drainage divides).

Step	Uncertainty	Typical	Measure	Comment
Pre-processing	geolocation	+/- 1 pixel	GCPs (provided with the Metadata information)	only relevant for L1/L2 outlines (DEM fusion)
Main-processing	algorithm	< 3%	validation data	accuracy is for debris-free ice
	threshold	< 5%	overlay of binary maps	see Gjermundsen et al. (2011)
	median filter	<2%	RGB composites filtered vs. unfiltered	could be larger for very small glaciers
Post-processing	water	> 100%	visual inspection (432)	should be removed
	other ice	> 100%	visual inspection (432)	should be removed
	debris	> 50%	comp. with ground truth	requires manual digitization
	shadow	< 50%	visual inspection (321)	can be locally difficult to identify
	projection	<2%	comparison with equal area projection	error <2% for +/-2 scenes combined in UTM projection

Table 3.2: Uncertainties contributing to the overall error budget.

When assessing an error against a reference data set, several issues have to be considered to derive the correct conclusions: The area of the glacier (polygon) changes with pixel size (e.g. Paul et al., 2003), at a much higher spatial resolution different features become visible, and without a band in the shortwave infrared (e.g. panchromatic imagery) the determination of the outline could be much more complicated (see Fig. 3.5). Moreover, some care has to be taken that the projection of the data used for comparison is the same. The reference data set that is used for comparison (or validation) must be acquired at the same point in time (week is sufficient in most cases) or at least the snow conditions must be the same.

3.6.2 Overall accuracy

The round robin for glacier area clearly revealed (cf. Paul et al., 2012), that product accuracy depends on the correct interpretation of the debris-covered glacier parts by the analyst and that it is difficult to determine the accuracy correctly, as potential reference datasets have about the same precision (a few percent). So the automated mapping with the band ratio method is as precise as manual digitization on the same (Landsat) or higher resolution imagery when applied to clean ice. Illustrated guidelines should be prepared to improve the consistency of the glacier mapping for glacier ice under debris cover.

3.7 Expected performance gains by future developments

As data availability and technical development is a continuous process, new algorithms and further improved products are expected in the future. The Glaciers_cci consortium will monitor the ongoing efforts and actively participate in related activities. Key technical issues that might be improved in the near future are:

- (a) higher consistency of the generated products globally (through illustrated guidelines)
- (b) improved outlines for debris-covered glaciers (by integrating coherence images)
- (c) better geo-location accuracy of the products (orthorectification with improved DEMs)
- (d) a reduced workload for post-processing once glacier outlines are available
- (e) a more easy conversion of outlines to the GLIMS format (development of scripts)
- (f) availability of data processing algorithms for public domain software products

The round robin for the glacier area product (Paul et al., 2013) confirmed earlier studies that the results of the various algorithms (band ratio, NDSI) can only be distinguished at the pixel level (e.g. Paul and Kääb, 2005) and that the uncertainties introduced in the post-processing stage are much larger, in particular for debris-covered glaciers. Hence, the algorithm used by the analyst to map glaciers can be freely chosen, but the editing of the outlines has to be performed with great care and improvements at this end have to be in the focus of further efforts. The illustrated guidelines mentioned under (a) will help to increase the consistency in the interpretation. The guidelines will also benefit from the application of coherence images (b) that have a high potential for improving the interpretation of outlines from debris-covered glaciers (e.g. Frey et al., 2012).

The improvement of the geo-location (c) will be a continuous effort at the institutions performing the operational processing of the raw satellite data. Any achievements here will be related to the availability of improved DEMs (e.g. from TanDEM-X) compared to what is currently used (mostly the SRTM DEM in the void filled version from CGIAR). A recent study by Frey et al. (2012) has shown that location shifts of about 3 to 5 pixels can occur in regions where the data voids in the SRTM DEM have been poorly interpolated. This shift results in a considerable mismatch between drainage divides and glacier outlines and a related high workload for manual editing. This workload can be reduced (d) with a better geolocation. Once the related drainage divides are defined (at the correct location), they can be applied repeatedly thus further reducing the post-processing workload (e). It is also faster to remove wrong classifications (e.g. water and seasonal snow) once glacier boundaries are identified (d), for example by applying a one or two pixel sized buffer around all outlines.

A current bottleneck for uploading the generated outlines to GLIMS is the required conversion to the specific GLIMS format (see PSD). When the related workload for the user can be reduced by applying scripts that perform the conversion automatically, data input will certainly increase (e). Such scripts are currently under development for integration of the RGI outlines in the GLIMS database. Finally, the algorithms applied for generating the glacier area product are computationally simple and it should be possible to integrate them also in public domain software products. Though this might not increase their application at the user site, it opens the possibility to provide data processing as a web-based service. This could be a goal in the long-term.

4. Elevation changes from repeat altimetry

4.1 Introduction

Satellite altimetry is a powerful tool for mapping the surface elevation of glaciers and ice caps and the instruments used to reach this purpose can be divided in two groups based on the part of the electromagnetic spectrum they utilise. **Figure 4.1** summarises the useful regions of the electromagnetic spectrum for remote sensing and the transparency of the atmosphere.

Laser altimeters operate at visible (typically at the green wavelength, i.e. 532 nm), but more usually at near infrared wavelengths (typically around 1024 nm). The main advantages of these instruments are related to the high absolute accuracy (accuracies better than 0.05 m have been demonstrated under optimal slope conditions by Fricker *et al.*, 2005) and to the smaller footprint size, which allows to consider more data points. The most significant difference of laser over radar altimeters is the much smaller ground footprint of less than a hundred metres in diameter (Zwally *et al.*, 2002), in contrast to that of several kilometres of radar altimeters. The main drawbacks are the short time series (for ICESat from 2002 to 2009), the infrequent repeat passes, detector saturation (Fricker *et al.*, 2005) and cloud interference with the beam.

Although laser altimeters are widely used airborne remote sensing instruments, there have been one of them (ICESat GLAS) orbiting in space. This is due to laser altimeters being electrically and mechanically more complicated than radar altimeters, making the space environment particularly harsh for them.

This chapter provides the theoretical basis of the algorithm which has been selected as the best performing algorithm for the production of elevation changes maps from laser altimeter data, to assess the accuracy, to evaluate the range of applicability and the limitations of the derived data.

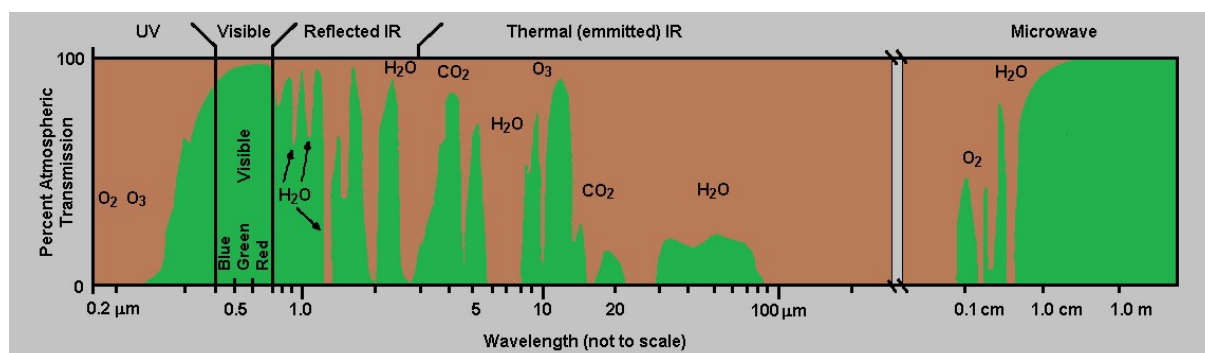


Fig 4.1: Typical atmospheric transparency and principal regions of the electromagnetic spectrum.

4.2 Scientific background

For the wavelengths used by spaceborne laser altimetry, the interaction of an electromagnetic wave with clouds and aerosol will be described to understand the main effects which cause attenuation and broadening of the laser beam as it propagates through the atmosphere. Heavy clouds (optical depth > 2 or so) will completely block ground returns, whereas thinner clouds

and aerosols cause forward scattering, which is indeed a specific problem for laser altimeters. In the presence of clouds or aerosols in the atmosphere, a part of the signal can be scattered. These scattered photons travel a longer path than photons that pass directly to and from the target. Therefore the mean travel time of the return pulse is lengthened, and the centroid of the pulse is shifted toward a later time (Duda *et al.*, 2001). Forward scattering causes a long tail in the waveform (Fricker *et al.*, 2005), and measurements with such a tail can later be discarded.

4.2.1 Review of laser principles

The basic idea of a laser profiler is rather simple. The instrument emits a short pulse of “light” (usually near-infrared radiation) from a downward-pointing laser. At the same instant, an electronic clock is started. The pulse propagates down through the atmosphere, bounces off the Earth’s surface, propagates back up through the atmosphere, and is detected by a photodiode. Detection of the pulse stops the clock, so that the two-way travel time to the surface can be deduced. If the propagation speed is known, the range to the surface can be determined. If the absolute position of the instrument is known, the absolute position of the reflecting point on the Earth’s surface can therefore also be determined.

The spatial resolution of a laser profiler has two aspects: horizontal resolution and vertical (height) resolution. The horizontal resolution is determined fundamentally by the beam width of the laser. For a laser with a beam width of $\Delta\theta$ (radians) operating from a height H above the surface, the horizontal resolution is clearly:

$$\Delta x = H\Delta\theta \quad (4.1)$$

This is often referred to as the laser’s footprint.

The vertical resolution is determined by the accuracy with which the two-way travel time can be measured. Assuming that the electronic clock is sufficiently accurate, the accuracy with which the travel time can be measured is governed by the rise time t_r of the detected pulse (the time it takes to increase from zero to maximum power) and its signal-to-noise ratio S . For a single pulse, the vertical resolution is given by:

$$\Delta z = \frac{ct_r}{2S} \quad (4.2)$$

where it is assumed that the pulses travel at the speed of light c . However, laser profilers are pulsed systems and if the pulse repetition frequency (PRF) f is high enough and the platform speed v is low enough, a given footprint-sized area on the Earth’s surface will be sampled several times. Since each of these samples is independent, and there are $(fH\Delta\theta/v)$ of them, the vertical resolution when these samples are averaged becomes:

$$\Delta z = \frac{ct_r}{2S} \sqrt{\frac{v}{fH\Delta\theta}} \quad (4.3)$$

Eq. (4.3) indicates the features of a laser profiler’s design that will give a high vertical resolution. The rise time of the returned pulse should be as short as possible. This obviously indicates that the transmitted pulse should be as short as possible, but reflection from a rough surface will spread the reflected pulse over time. The signal-to-noise ratio should be as high as possible, which indicates that a large transmitted power is needed, and also that the height

H should be small to reduce losses through absorption and geometrical spreading. The platform speed should be small and the horizontal resolution $H\Delta\theta$ large, though these considerations are clearly not optimal for other reasons. The PRF should be as high as possible, but there is an upper limit on the PRF. If it is too large, the measurement of the range H becomes ambiguous because it is no longer possible to identify which return pulse corresponds to which transmitted pulse. The simplest situation is that in which the second pulse is not transmitted until the first pulse has been received, and this implies that:

$$f < \frac{c}{2H} \quad (4.4)$$

Figure 4.2 sketches the returned laser pulse, which is broadened by the distribution of surface heights within the footprint. The surface height distribution is characterised by a mean surface slope and a surface roughness within the footprint.

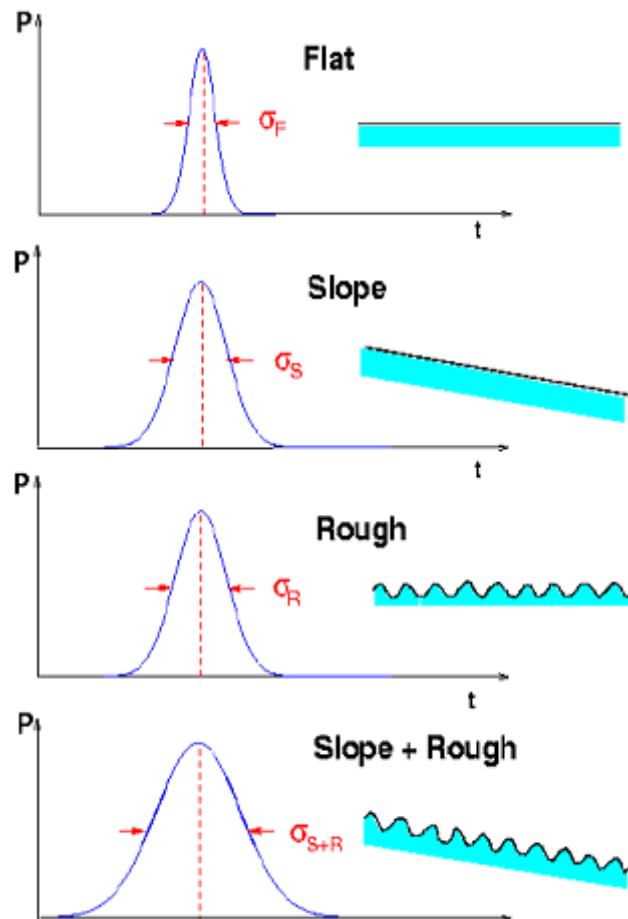


Fig. 4.2: Characteristics of the returned laser pulse as function of surface type. Both, surface slope and roughness broaden the pulse. Sigma (σ) indicates one standard deviation.

4.2.2 Laser beam atmospheric propagation

Many studies have been undertaken for characterising and modelling linear and non-linear atmospheric propagation effects on laser beams. In the following paragraphs, only a brief

introduction to the fundamentals of laser beam propagation is presented, with emphasis on those phenomena affecting the peak irradiance at the target.

4.2.2.1 Atmospheric transmittance

Attenuation of laser radiation in the atmosphere is described by the Beer Lambert law:

$$\tau(\lambda, z) = \frac{P(\lambda, z)}{P(\lambda, 0)} = e^{-\gamma(\lambda)z} \quad (4.5)$$

where

- $\tau(\lambda)$ is the total transmittance of the atmosphere at the wavelength λ
- $P(\lambda, z)$ is the power at the distance z from the transmitter
- $P(\lambda, 0)$ is the emitted power
- $\gamma(\lambda)$ is the attenuation or the total extinction coefficient per unit of length

If the attenuation coefficient is a function of the path, the Eq. (4.5) becomes:

$$\tau(\lambda, z) = \int_0^z e^{-\gamma(\lambda, z')z'} dz' \quad (4.6)$$

The attenuation coefficient is determined by four individual processes: molecular absorption, molecular scattering, aerosol absorption, and aerosol scattering. The atmospheric attenuation coefficient is:

$$\gamma(\lambda) = \alpha_m(\lambda) + \alpha_a(\lambda) + \beta_m(\lambda) + \beta_a(\lambda) \quad (4.7)$$

where α is the absorption coefficient, β is the scattering coefficient, and the subscripts m and a designate the molecular and aerosol processes, respectively. Each coefficient as shown in the equation depends on the wavelength of the laser radiation. It is convenient to discuss absorption and scattering in terms of the absorption and scattering cross sections, σ_a and σ_s , respectively, of the individual particles that are involved. They are defined as the ratio of the absorbed power to the incident power density and as the scattered power to the incident power density, respectively, and have the dimension of an area (m^2). Thus, it is possible to write:

$$\alpha = \sigma_a N_a \quad (4.8)$$

and also

$$\beta = \sigma_s N_s \quad (4.9)$$

where N_a and N_s are the concentrations of the absorber and scatterers, respectively. In the absence of precipitation, the atmosphere contains finely dispersed solid and liquid particles (of ice, dust, aromatic and organic material) that vary in size from a cluster of a few molecules to particles of about 20 μm in radius. Particles larger than this remain airborne for a short time and are only found close to their sources. Such a system, in which a gas (in this case, air) is the continuous medium and particles of solid or liquid are dispersed, is known as an aerosol. Aerosol attenuation coefficients depend considerably on the dimensions, chemical composition, and concentration of aerosol particles. These particles are generally assumed to

be homogeneous spheres that are characterized by two parameters: the radius and the index of refraction. In general, the index of refraction is complex and defined as:

$$n = n' - jn'' \quad (4.10)$$

In general, both n' and n'' are functions of the frequency of the incident radiation. The imaginary part (which arises from a finite conductivity of the particle) is a measure of the absorption coefficient. In fact n'' is related to the absorption by (Ulaby et al., 1982):

$$\alpha = \frac{2\pi}{\lambda} n'' \quad (4.11)$$

For the wavelength in the visible region to about 15 μm the principal atmospheric absorbers are the molecules of water, carbon dioxide, and ozone. Attenuation occurs because these molecules selectively absorb radiation by changing vibrational and rotational energy states. The two gases present in greatest abundance in the Earth's atmosphere, nitrogen (N_2) and oxygen (O_2), do not possess electric dipole moment and therefore do not exhibit molecular absorption bands. The H_2O and CO_2 are by far the most important absorbing molecules. Other absorbing molecules found in the atmosphere are methane (CH_4), nitrous oxide (N_2O), carbon monoxide (CO) and ozone (O_3).

The scattering coefficient β in Eqs. (4.7) and (4.9) also depends on the frequency of the incident radiation as well as the index of refraction and radius of the scattering particle (supposed spherical). The incident electromagnetic wave, which is assumed to be a plane wave in a given polarisation state, produces forced oscillations of the bound and free charges within the sphere. These oscillating charges in turn produce secondary fields internal and external to the sphere. The resulting field at any point is the vector sum of the primary (plane wave) and secondary fields. Once the resultant field has been determined, the scattering cross section can be obtained. As is indicated in **Table 4.1**, the physical size of the scatterer determines the type of scattering. Thus, air molecules that are typically several angstrom units in diameter lead to Rayleigh scattering, whereas the aerosols scatter light in accordance with the Mie theory. Furthermore, when the scatterers are relatively large, such as the water droplets found in fog, clouds, rain, or snow, the scattering process is more properly described by diffraction theory (Ulaby et al., 1982).

Type of Scattering	Size of Scatterer
Rayleigh Scattering	Larger than electron but smaller than λ
Mie Scattering	Comparable in size to λ
Non-selective Scattering	Much larger than λ

Table 4.1: Types of atmospheric scattering.

In the scattering process there is no loss of energy but only a directional redistribution which may lead to a significant reduction in beam intensity for large path lengths. In addition to this reduction, the presence of thin clouds and aerosols produces the multiple scattering phenomenon and consequently a stretching of the laser pulse and the presence of a long tail (Fricker et al., 2005). Scattered photons that pass through thin clouds and aerosols travel a

longer path than photons that pass directly to and from the surface, so the mean travel time of the return pulse is lengthened and the centroid of the pulse is shifted toward a later time (Fig. 4.3). The use of the pulse centroid as the receiver time then produces a biased measurement or an apparent delay in the receive time (Duda et al., 2001).

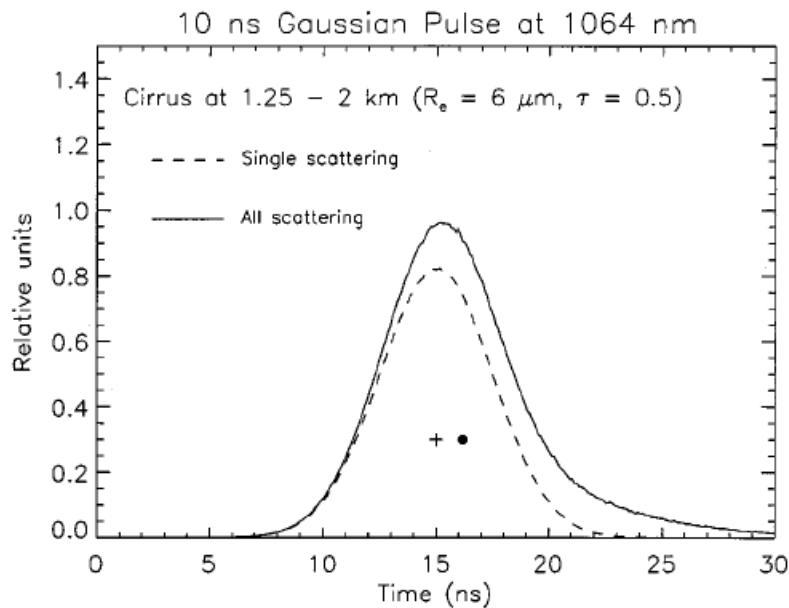


Fig. 4.3: Plot of a typical simulated GLAS return pulse as a function of time in the presence of cirrus clouds at heights ranging from 1.25 – 2 km, with particle radius $R_e = 6 \mu\text{m}$ and optical depth $\tau = 0.5$. The initial lidar pulse was assumed to be not divergent and to have a normal distribution of intensity with a pulse width of 10 ns. The centroid of the singly scattered part of the pulse is shown as a plus sign, and the filled circle indicates the centroid of the entire pulse (Duda et al., 2001).

To calculate the mean path delay accrued by photons, the angular distribution of the scattered energy must be known. This is represented by the scattering phase function. For particles that are large compared to the wavelength of light, diffraction theory shows that one half of the energy is scattered into a narrow forward diffraction peak. A reasonable approximation to this forward scattering peak can be achieved with a Gaussian (Eloranta, 1998). In (Duda et al., 2001), the authors derive the expression of the additional mean path delay based on a phase function given by the sum of a Gaussian forward peak containing one half of the scattered energy with the other half in an isotropic component. Figure 4.4 shows the average path delay of the received photons as function of mean cloud altitude and particle radius for the ICESat field of view of $475 \mu\text{rad}$. Large delays are predicted for clouds composed of particles less than $50 \mu\text{m}$ in radius, and for low altitude clouds.

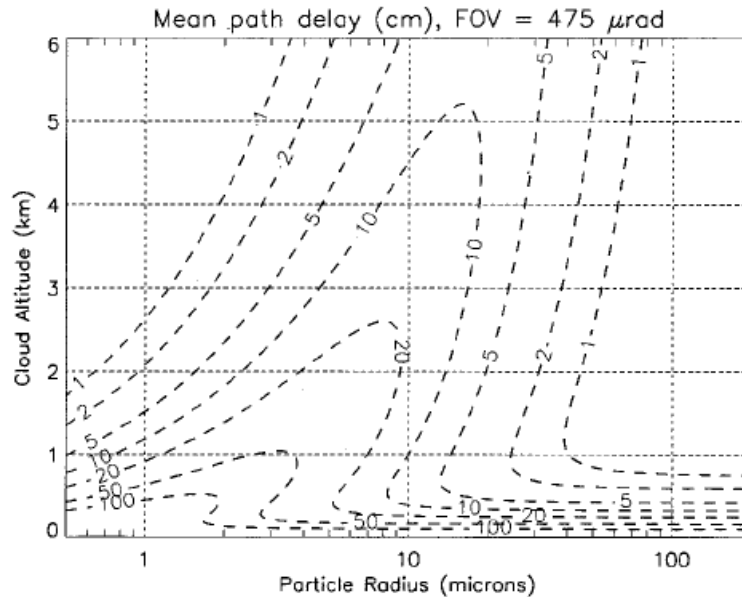


Fig. 4.9: Mean GLAS path delay (in cm) of doubly scattered photons derived from the analytic model as a function of mean cloud height and cloud particle size. These results assume an optical depth of 0.2 (Duda et al., 2001).

4.2.2.2 Propagation through haze and precipitation

Haze refers to the small particles suspended in the air. These particles consist of microscopic salt crystals, very fine dust, and combustion products. Their radii are less than $0.5 \mu\text{m}$. During periods of high humidity, water molecules condense onto these particles, which then increase in size. It is essential that these condensation nuclei are available before condensation takes place. Fog occurs when the condensation nuclei grow into water droplets or ice crystals with radii exceeding $0.5 \mu\text{m}$. Clouds are formed in the same way; the only distinction between fog and clouds is that one touches the ground while the other does not.

In the early stages of droplet growth the scattering cross section, and consequently the scattering coefficient, depends strongly on the wavelength. When the drop has reached a radius $a \approx 10\lambda$ the scattering process is now independent of wavelength, i.e., it is non-selective. Since most of the fog droplets have radii ranging from 5 to $15 \mu\text{m}$ they are comparable in size to the wavelength of infrared radiation. Consequently the value of the scattering cross section is near its maximum. It follows that the transmission of fog in either the visible or infrared spectral region is hampered for any reasonable path length. This, of course, also applies to clouds.

Since haze particles are usually less than $0.5 \mu\text{m}$, a laser in the infrared region has $a/\lambda \ll 1$ and thus the scattering is not an important attenuation mechanism. Rain drops are of course many times larger than the wavelengths of laser beams. As a result there is no wavelength-dependent scattering. The scattering coefficient does, however, depend strongly on the size of the drop. In order to obtain accurate estimates of this parameter, the concentrations of different types of rain drops (radius) and the associated rainfall rates should be known. In this case, the scattering coefficient can be calculated as the sum of the partial coefficients associated to the various rain drops.

4.2.2.3 Refractive index variation

When a laser beam passes through air, the randomly fluctuating air temperature produces small density and refractive index inhomogeneities that affect the beam in at least three different ways. Considering for example an initially well-defined phase front propagating through a region of atmospheric turbulence. Because of random fluctuations in phase velocity the initially well defined phase front will become distorted. This alters and redirects the flow of energy in the beam. As the distorted phase front progresses, random changes in beam direction (“Beam Wander”) and intensity fluctuations (“Scintillation”) occur. The beam is also found to spread in size beyond the dimensions predicted by diffraction theory.

The cause of all this, as we have stated, is the atmospheric turbulence that arises when air parcels of different temperatures are mixed by wind and convection. The individual air parcels, or turbulence cells, break up into smaller cells and eventually lose their identity. In the meantime, however, the mixing produces fluctuations in the density and therefore in the refractive index of air. To describe these random processes, one must have a way of defining the fluctuations that are characteristic of turbulence. The most common approaches adopted may be found in Strohbehn et al, 1978 and Weichel, 1990.

4.2.3 Electromagnetic properties of snow in the optical and near-infrared regions

Fresh dry snow appears highly reflective, with little variation over the range of wavelengths approximately from 0.4 to 0.65 μm . The reason for this lies in the dielectric properties of ice, and the fact that the ice constituting snow is in a very highly divided form with of the order of 10^9 particles per cubic metre.

Figure 4.5 is based on data given by Warren (1984) and collated by Rees (1999), illustrates this in more detail. In ice, the absorption length of visible-wavelength radiation, defined as the distance through which the radiation must travel in order for its intensity to be reduced by a factor e as a result of absorption alone, is of the order of 10 m, which means that in traversing a snow pack with a thickness of (say) 2 m, containing a total thickness of perhaps 1 m of ice, a photon has a negligible chance of being absorbed. On the other hand, the photon will encounter of a few thousand air–ice and ice–air interfaces as it traverses the pack, with a probability of about 0.02 of being reflected at each of these interfaces. Thus, it is almost certain that the photon will be scattered back out of the snow pack, and since neither the absorption nor reflection properties of ice vary significantly over the visible waveband, this will be equally true for all wavelengths.

This simple argument, which is developed more fully by Rees (2001), also implies that the reflection coefficient of a snow pack should be smaller if the grain size is larger, since the number of air–ice interfaces and hence scattering opportunities will be reduced. Furthermore, the generally increasing absorption (smaller absorption lengths) at longer wavelengths, illustrated in Fig. 4.5, implies a corresponding reduction in reflectance at these wavelengths. These phenomena are illustrated in Fig. 4.6, which shows the comparative insensitivity of reflectance to grain size in the visible region and the high degree of sensitivity in the range from about 1.0 to 1.3 μm .

The reflectance of snow does not depend directly on density, although the processes of compaction by wind and gravity that cause the increase in density over time also lead to an increase in grain size and hence a consequent decrease in reflectance. As a snow pack ages, it

may also acquire a covering of dust or soot that may also decrease the reflectance. While the albedo of a fresh snow cover can exceed 90%, this figure can fall to 40% or even as low as 20% for dirty snow (Hall and Martinec, 1985).

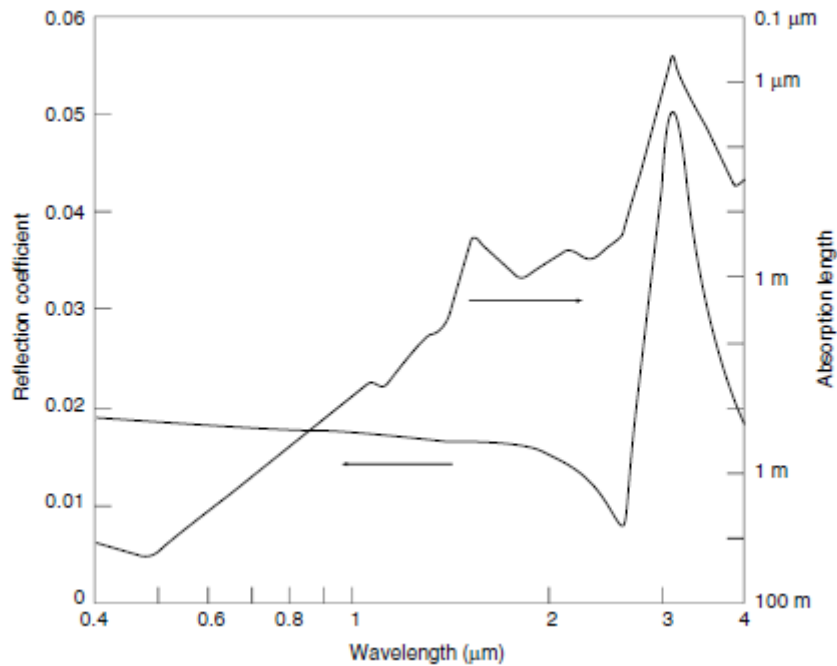


Fig. 4.5: Reflection coefficient from an ice-air interface (curve identified by the arrow pointing to the left) and absorption length in ice (curve identified by the arrow pointing to the right) for electromagnetic radiation with wavelengths between 0.4 and 4 μm (simplified)

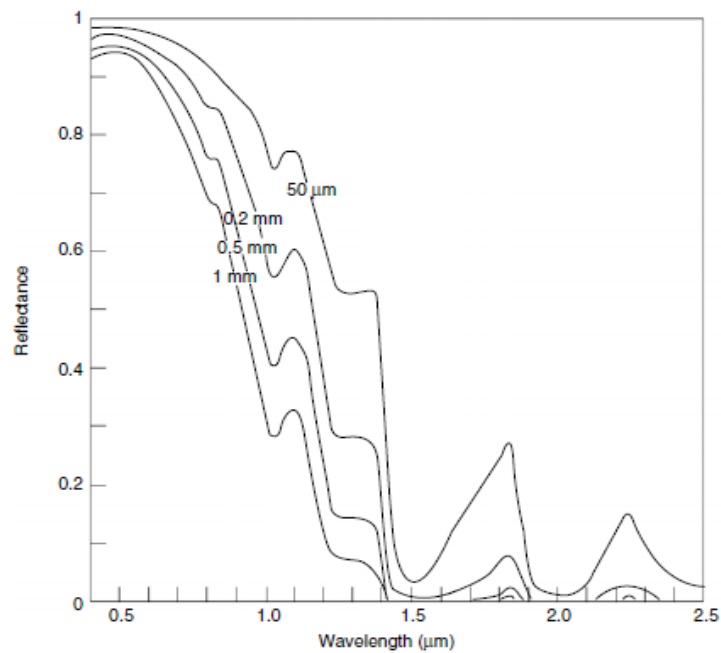


Fig. 4.6: Spectral reflectance of a deep snow pack as a function of grain size (based on Choudhury and Chang, 1979).

It is clear that these arguments apply only if the snow pack is sufficiently thick, since most of the photons encountering a thin pack will travel right through it without being scattered. This phenomenon can be quantified by specifying a scattering length for the snow pack. This is analogous to the absorption length, specifying the distance that radiation must travel through the medium before its intensity in the direction of propagation is reduced by a factor of e as a result of scattering. The optical thickness of a uniform snow pack is just the ratio of its actual thickness to its scattering length, and is a measure of its opacity. It is proportional to the grain size (radius) and inversely proportional to the snow density. Thus the optical thickness for a given grain size will depend principally on the snow water equivalent.

The presence of liquid water in a snow pack has little direct effect on its reflectance. The amount of water rarely exceeds 10% by volume and there is in any case sufficient dielectric contrast between water and ice to ensure that the multiple-scattering phenomenon continues to occur. The absorption of electromagnetic radiation in water is similar to that in ice in the visible and near-infrared regions. On the other hand, the presence of liquid water does have an indirect effect on the optical properties, since it promotes clustering of the ice crystals leading to a larger effective grain size and hence lower reflectance. Green et al. (2002) present model simulations that take into account both grain size and liquid water content as influences on the reflectance of snow. The most significant effect of increasing water content appears to be a small shift of the absorption feature at 1030nm to shorter wavelengths.

Reflection from a snow pack is anisotropic (not strictly Lambertian), with enhanced specular scattering due to reflection from ice crystals (Middleton and Mungall, 1952; Hall et al. 1993; Knap and Reijmer, 1998; Jin and Simpson, 1999). However, most studies to date have neglected this effect (Koenig et al, 2001) even though it is rather important in calculating the albedo of a snow-covered surface.

4.2.4 Electromagnetic properties of glaciers in the optical and near-infrared regions

In the winter, a glacier surface is usually covered by snow. The optical properties of snow cover have already been discussed in the previous section. In the summer, however, other surfaces can be exposed. Figure 4.7 summarises some experimental data on the spectral reflectance properties of glacier surfaces. The spectra *a*, *c*, *e*, and *f*, for fresh snow, firn, clean glacier ice, and dirty glacier ice, respectively, are adapted from Qunzhu et al. (1984), while the spectra *b* and *d*, for the accumulation and ablation areas of Forbindels Glacier in Greenland, are adapted from Hall et al., 1990. Comparison of curve 'a' with Fig. 4.6 shows that the snow grain size in this case is about 0.2 mm.

It is possible to note from Fig. 4.7 a general tendency for the visible-wavelength reflectance of a glacier surface in summer to increase with altitude, moving upwards from the ablation area. This is illustrated in Fig. 4.8, which shows the broad-band albedo of the glacier Midre Lovenbreen in Svalbard, measured in situ in summer. At wavelengths longer than about 600 nm the same general trend is observed, although there is greater observed scatter in the results, presumably as a consequence of the greater sensitivity to structural details such as grain size (Winther, 1993) and the quantity and size of air bubbles in ice.

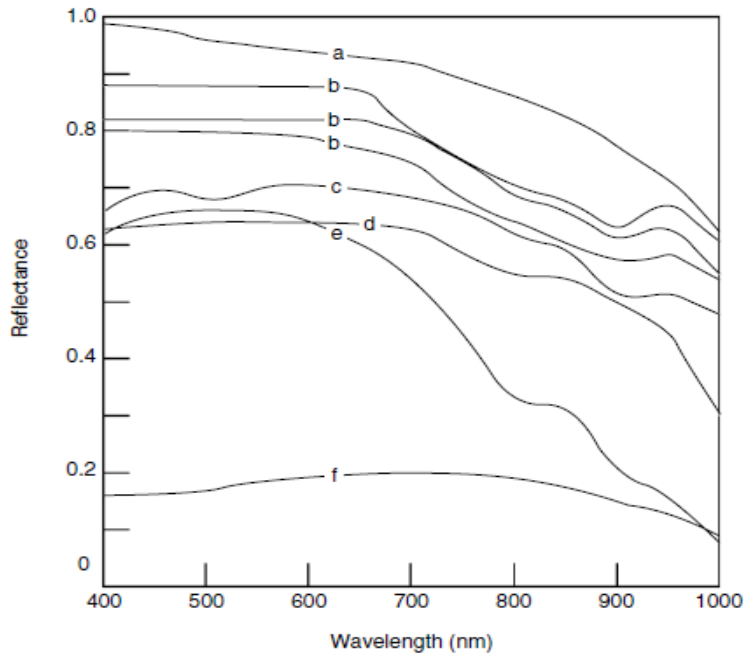


Fig. 4.7: Spectral reflectance of different glacier surfaces (simplified). a: fresh snow; b: accumulation area; c: firn; d, e: glacier ice; f: dirty glacier ice.

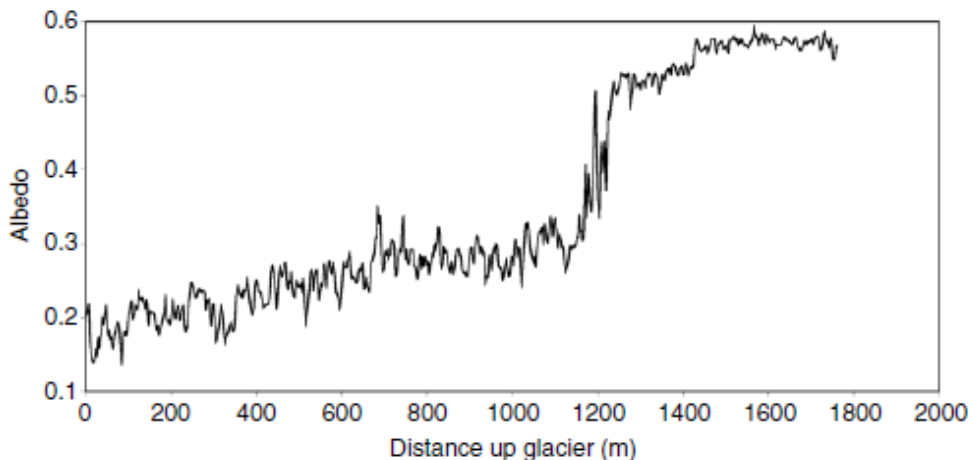


Fig. 4.8: Longitudinal profile of Midre Lovénbreen, Svalbard, showing the variation of summer albedo (data supplied by N. S. Arnold, Scott Polar Research Institute).

4.3 Justification on the algorithm chosen

Elevation changes using satellite altimeter data are typically studied with either crossover or repeat track analysis. Both techniques have been described in the ATBDv0 (Glaciers_cci, 2012a) and were applied during the round robin, using radar altimeter data as input of the cross-over method and laser altimeter data as input to the different implementations of the repeat-track methods (cf. Glaciers_cci, 2012a). The results of the comparison and validation activities are reported in the PVASR (Glaciers_cci, 2012b). In particular, the limitation of the cross-over method in terms of spatial coverage was quite evident when compared with the

repeat-track algorithm. The comparison between the different repeat-track implementations showed a good agreement between them indicating their almost equivalence. From the validation against airborne data, it evidently appeared that due to the large footprint the radar altimeter data were not measuring properly the elevation in correspondence of the ice sheet margin where the slope is too high. In addition, the repeat track method applied to laser altimeter data provided estimates of ice cap surface elevation change with significantly better accuracy than the cross-over method applied to radar altimeter. As a conclusion, the repeat track method applied to laser altimeter data has been selected as the most reliable technique for developing satellite based observations of ice cap surface elevation change.

It is worth noting that the selected repeat track algorithm, further described in the next section, is also applicable to new Cryosat-2 radar altimeter data, which is characterised by a footprint size comparable to the laser altimeter measurements available. Cryosat-2 is the first satellite equipped with a SAR Interferometric Altimeter (SIRAL) to enhance the radar's horizontal resolution to 250 m while allowing for precise measurements of changes as small as a few centimetres. Whereas conventional radar altimeters send pulses at intervals long enough that the echoes are "uncorrelated" (about 500 μ s), the CryoSat-2 altimeter sends a burst of pulses at an interval of only about 50 μ s. The returning echoes are correlated and, by treating the whole burst together, the data processor can separate the echo into strips arranged across the track by exploiting the slight frequency shifts, caused by the Doppler effect, in the forward- and aft-looking parts of the beam. Each strip is about 250 m wide and the interval between bursts is arranged so that the satellite moves forward by 250 m each time. The strips laid down by successive bursts can therefore be superimposed on each other and averaged to reduce noise which is known as the SAR mode. In addition, the presence of a second antenna, which receives the radar echo simultaneously, provides a SAR Interferometry capability. Thus, Cryosat-2 is able to identify the location of the echo on sloping surfaces, such as those found around the edges of ice sheets.

4.4 Mathematical algorithm development description

Repeat-track analysis is a technique used to detect elevation change rate by comparing elevations from different times along the same repeat portion of a ground-track or spot track from one orbital revolution of the altimeter, also referred to as track segment (Zlotnicki et al., 1989). The track segments will not repeat exactly, so repeat-track analysis is an attempt to reduce the associated errors by estimating parameters that influence the elevation. In an ideal case, ground-tracks or spot tracks for altimeter satellites in repeat-track orbits would repeat exactly so that elevations along the track at one time could be directly compared to elevations along the same track obtained at a different time. However, differences in the altimeter pointing angle and orbital perturbations will cause cross-track differences which should therefore be compensated for within the repeat track analysis.

The unmeasured topography between near repeat-tracks needs to be considered when comparing elevations from different tracks. The algorithm selected, the DEM Subtracting Repeat Track Repeat Altimetry (DS-RT-RepAlt) is based on the use of an external DEM (the best available for the respective region) for correcting the slope effects. It slightly differs from the DP-RT-RepAlt algorithm described in the ATBDv0 (Glaciers_cci, 2012a). In fact, the algorithm computes the difference between the GLAS measured elevations and the DEM elevations at each altimetry footprint location to assess the elevation change. The DEM elevations at these locations are obtained by interpolating the DEM grid.

For a detailed mathematical description it is necessary to introduce an appropriate symbology for representing GLAS measurements, the epoch of acquisitions and the DEM elevation data.

Thus, for the i -th laser measurement at the acquisition time $t = t_i^m$, with $t_i^m \in [t_{ini}, t_{fin}]$, where t_{ini} and t_{fin} represent the epoch time interval under consideration, the measurement is indicated as a point in a 3D space, where the first two coordinates, x_i^m, y_i^m , represent the location on the Earth (i.e. latitude and longitude) and the third coordinate, h_i^m , represents the elevation above the reference ellipsoid (WGS84):

$$P_i^m = (x_i^m, y_i^m, h_i^m)$$

The upper index m stands for measurements. The same notation is used to indicate the j -th elevation available from the DEM obtained at the reference time $t = t_{REF}$:

$$P_j^{DEM} = (x_j^{DEM}, y_j^{DEM}, h_j^{DEM})$$

As mentioned above, the DEM elevation around the location of the laser acquisition were interpolated to achieve the elevation from the DEM data exactly in such location. Assuming a number of k DEM elevations available around the location (x_i^m, y_i^m) and indicating with f_{int} the interpolation function, the interpolated elevation can be written as follows:

$$h'_i = f_{int}(x_i^m, y_i^m; x_1^{DEM}, y_1^{DEM}, \dots; x_j^{DEM}, y_j^{DEM}, \dots; x_k^{DEM}, y_k^{DEM}) \quad (4.12)$$

The difference between GLAS measured elevation and the DEM elevation can be expressed as:

$$\Delta h_{t_i^m - t_{REF}}(x_i^m, y_i^m) = h_i^m - h'_i \quad (4.13)$$

The differences achieved for each laser footprint are then averaged in order to represent the spatial variation on grid cells of 1 km x 1 km:

$$\overline{\Delta h_{\bar{t}}}(x_c, y_c) = \frac{\sum_{k=1}^N \Delta h_{t_k^m - t_{REF}}(x_k^m, y_k^m)}{N} = \frac{\sum_{k=1}^N h_k^m - h'_k}{N} \quad (4.14)$$

where N is the number of laser acquisitions within a fixed range distance from the centre of each grid cell, (x_c, y_c) , and t_k^m is the time of the each acquisition within the epoch considered, that is $t_k^m \in [t_{ini}, t_{fin}]$. The sub-index \bar{t} is the mean time value associated with the averaged difference $\overline{\Delta h}$:

$$\bar{t} = \frac{\sum_{k=1}^N t_k^m}{N} \quad (4.15)$$

This procedure is repeated for each ICESat operational period and the elevation trend for each grid cell is determined by fitting a first order polynomial, $\Delta h(t) = b_0 + b_1 t$, so that the slope of the polynomial, the coefficient b_1 , represents the elevation trend in the data bin considered (Rinne et al., 2011). Analytically, if \bar{t}_i represents the averaged time of the i -th operational period, or epoch, and $\overline{\Delta h}_i(x_c, y_c)$ is the average difference relative to such time in the grid cell centred around (x_c, y_c) , the first order polynomial is identified applying the least square method. The best estimation of the coefficients b_0 and b_1 is obtained minimising the sum square error:

$$\min_{b_0, b_1} \sum_{i=1}^M [\Delta h(\bar{t}_i) - \overline{\Delta h}_i]^2 = \min_{b_0, b_1} \sum_{i=1}^M [b_0 + b_1 \bar{t}_i - \overline{\Delta h}_i]^2 \quad (4.16)$$

where M is the total number of operational period, or epoch.
 If we define the cost function $f(b_0, b_1)$ as follow:

$$f(b_0, b_1) = \sum_{i=1}^M [b_0 + b_1 \bar{t}_i - \overline{\Delta h}_i]^2 \quad (4.17)$$

minimising the eq. (4.16) corresponds to solve the following system of equations:

$$\begin{cases} \frac{\partial f}{\partial b_0} = 0 \\ \frac{\partial f}{\partial b_1} = 0 \end{cases} \quad (4.18)$$

whose solutions are:

$$\hat{b}_0 = \frac{\sum_{i=1}^M \overline{\Delta h}_i}{M} - \hat{b}_1 \frac{\sum_{i=1}^M \bar{t}_i}{M} \quad (4.19)$$

$$\hat{b}_1 = \frac{\frac{\sum_{i=1}^M \bar{t}_i \overline{\Delta h}_i}{M} - \frac{\sum_{i=1}^M \bar{t}_i}{M} \frac{\sum_{i=1}^M \overline{\Delta h}_i}{M}}{\frac{\sum_{i=1}^M \bar{t}_i^2}{M} - \left(\frac{\sum_{i=1}^M \bar{t}_i}{M} \right)^2} \quad (4.20)$$

Figure 4.9 is a flow chart for the computational procedure described above.

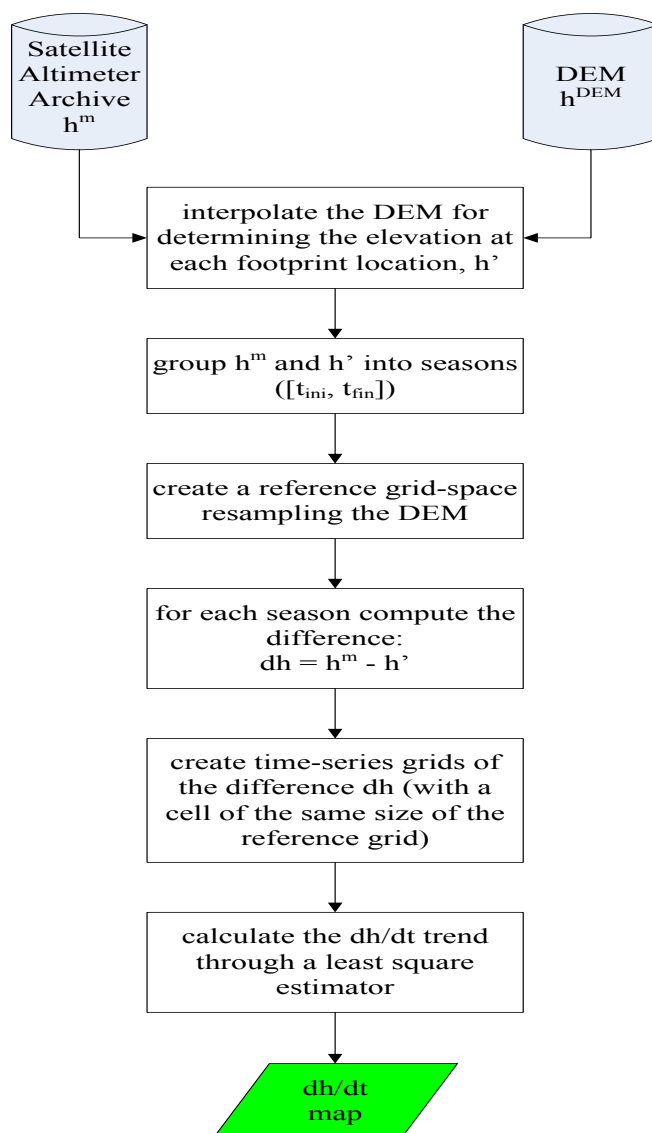


Fig. 4.9: Flow chart of the selected algorithm: DS-RT-RepAlt.

4.5 Description of the processing line

Figure 4.10 shows the processing line to apply together with the DS-RT-RepAlt Algorithm. Before starting the processing, the ICESat data archive needs to be filtered to discard data points where no saturation correction was applied and data points with large receiver gain values (greater than 150). A further check before applying the selected algorithm regards the system reference projection used. In the case the two input datasets, the laser and DEM data, are expressed in two different reference systems then it is necessary to convert them into a common one.

After the subtraction of the DEM from the elevation measurements, the time series is created taking into consideration measurement density thresholds and statistical filtering, like a 3-sigma clipping, where all the differences $\overline{\Delta h}_i$ that deviate more than three times the standard deviation from their mean value are discarded. Eventually a glacier mask is applied to discard all the points falling outside a given ice outline.

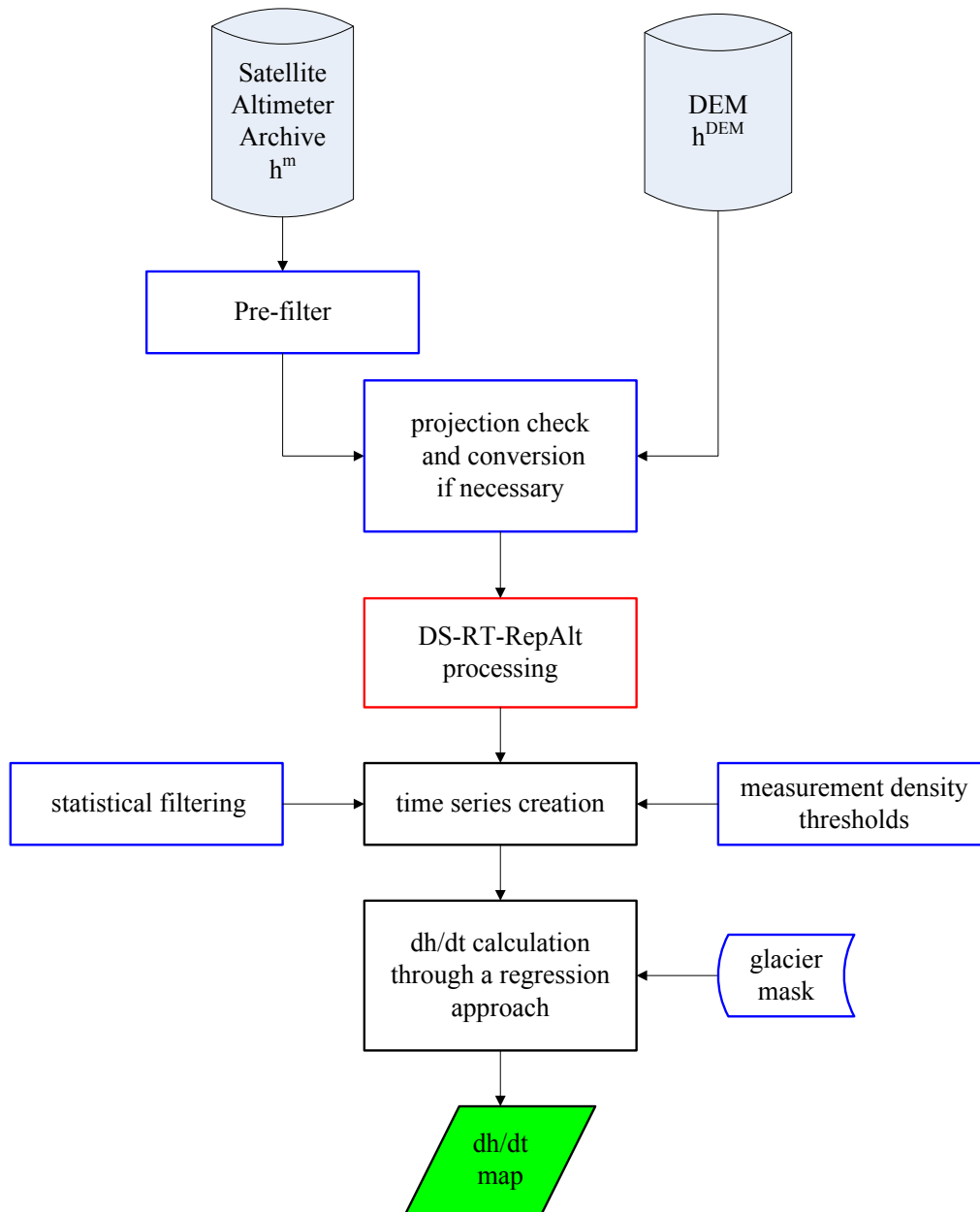


Fig. 4.10: Generalized processing line for the dh/dt map from altimeter data.

4.6 Input data and algorithm output

The input necessary for the DS-RT-RepAlt algorithm are the ICESat/GLAS measurement and the DEM. The left panel of Fig. 4.11 shows an example of the elevations measured with the laser altimetry over Devon Ice Cap, which extends approximately over 13700 km². On the right panel the DEM is shown in form of iso-level curves corresponding to increments of 100 m over the same area.

The elevation change is provided on a grid space with resolution of 1 km x 1 km. The elevation trend is associate with the location corresponding to the centre of each grid cell. This information are saved in a ASCII file. Figure 4.12 shows an example of the elevation change over Devon Ice Cap obtained with the DS-Rt-RepAlt algorithm selected.

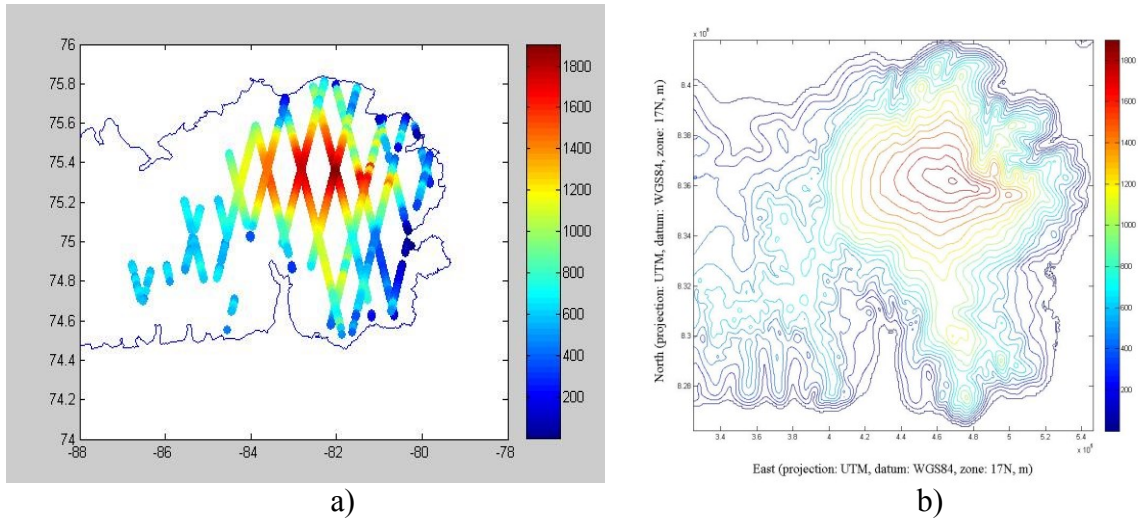


Fig. 4.11: a) Elevation in m obtained using the ICESat/GLAS archive over Devon Ice Cap; b) DEM, the iso-level curves correspond to increments of 100 m.

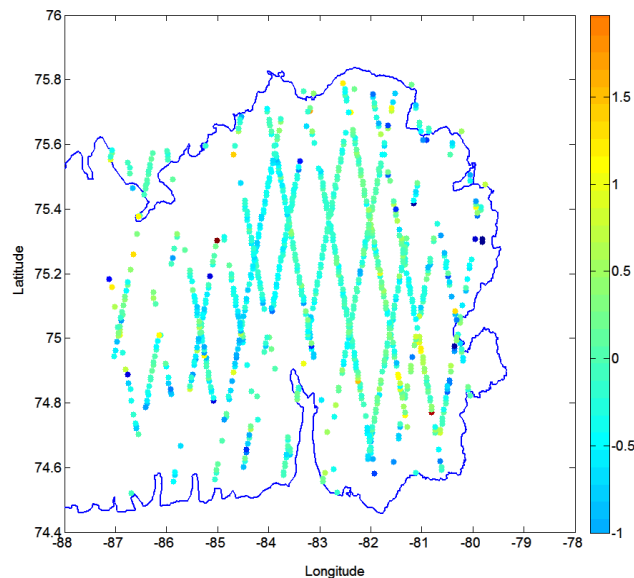


Fig.4.12: Example of dh/dt output of the DS-RT-RepAlt algorithm applied over Devon Ice Cap.

4.8 Error budget estimates

There are several potential error sources originating from the EO data themselves that have an effect on the surface elevation measured. To achieve the best possible accuracy, the effect of these variables must be compensated for. However, their impact on the results is very small and the required computational effort to determine them is beyond the possibilities of the processor presented here. They are thus mentioned here for completeness only:

- uncertainty in satellite orbit (also known as radial uncertainty) due to gravity anomalies of the Earth as well as the gravity of the Sun and the Moon;
- uncertainty in satellite attitude (roll, pitch and yaw rotations) due to fuel consumption, solar panel orientation and other factors;
- waveform saturation;
- atmospheric propagation effects, i.e. the attenuation introduced by the scattering of water droplets and aerosols, and the multiple scattering phenomenon which causes a stretching of the return pulse and the formation of a long tail;
- Propagation effects due to haze and precipitation;
- Refractive index variation effects (random fluctuations in phase velocity and consequent phase front distortion; redirection of the flow of energy in the beam; intensity fluctuations; beam spreading);
- solid Earth tides due to gravity pull of the Moon and the Sun and to the variations of the Earth's rotation axis;
- ocean loading tides.

4.9 Practical considerations for implementation

The NGAT software provided by NSIDC is used to open the ICESat/GLAS file and extract the information needed, i.e. the location of the measurements, the elevation, the time of acquisition, the saturation correction, and the gain. Additional scripts (described in the DPM) have to be used for converting the location of the measurements expressed in the geodetic reference system to the DEM reference system.

5. Elevation changes from DEM differencing

5.1 Introduction

This product is a spatially complete grid of elevation change values that can be converted to volume changes and to mass changes if appropriate assumptions of the density of the changed material can be made. DEM differences may be created over time spans of more than about five years to reduce the impact of seasonal fluctuations of glacier surface elevation due to meteorological causes (mass balance processes).

For DEM differencing, the major algorithms presented in this chapter are a part of the **pre-processing** stage. In order to assure that multi-temporal elevation data actually stem from corresponding ground points, i.e. have exactly the same horizontal coordinates in a reference system, elevation data sets require co-registration. This minimizes potential systematic errors (biases). After co-registration, biases may remain related to the acquisition strategy and DEM creation. For example, ASTER and SPOT DEMs have shown to have errors related to pointing inaccuracies of the sensors (Berthier et al., 2007; Nuth and Kääb, 2011). These should be analysed, typically by looking at along track and cross track geometries. However, as these types of biases are sensor or even scene-dependent, they are not considered as uniformly applied in all situations and therefore will remain as a suggested work-flow rather than a defined algorithm in the Glaciers_cci project.

After co-registration between the DEMs, the main **elevation difference** algorithm is applied by simply differencing the two DEMs. The DEM differences (sometimes called dDEM, differential DEM) have three important error characteristics: voids, noise and bias. At all locations where at least one DEM has a void the dDEM will have a void (no-data value) too. There are many reasons for these voids but all depend primarily on the methods used for DEM generation (e.g. failed correlation for optical stereo, lack of phase coherence for InSAR, perspective obstruction by adjacent terrain, etc.). Secondly, dDEMs are affected by noise or random errors. These are typically evaluated statistically using the root sum of squares (RSS) or standard deviations of the vertical differences between DEMs on stable terrain. Last, potential un-removed systematic bias may remain. They can be evaluated if a third dataset is available (e.g. laser altimetry). By performing co-registration between all three datasets, the residual remaining by triangulation of the three co-registration vectors is an estimate of the un-removed systematic bias. Hence, altimetry helps correctly calculating a dDEM while the DEM itself helps to correctly determine elevation changes from altimetry (slope correction). Last, as a **post-processing** step, dDEMs may be filtered or smoothed. This will also be a site/data specific task and thus Glaciers_cci will not particularly focus on these algorithms. However, resampling to larger grids may be applied by Glaciers_cci when providing data, to abide by potential copyright laws (e.g. in the case of national DEMs).

5.2 Scientific background on DEM generation

Digital Elevation Models are spatially continuous representations of the Earth surface and may be generated using stereo optical images, laser pulse scanning or radar interferometry on either terrestrial, aerial or satellite platforms. This variation of acquisition methods results in a plethora of data that has different attributes. Since Glaciers_cci will focus on the differencing of this type of data, and not specifically on the generation of DEMs, this section will only provide a short overview of the acquisition methods and DEM generation.

5.2.1. Stereoscopic DEMs

Stereoscopic DEMs are generated using photogrammetric principles. In along-track stereo, a parallax measurement gives the difference between the projected stereo rays of the same object onto the Earth's ellipsoid and can be converted to height provided the observer positions, the sensor pointing angles and camera parameters are known (Lillesand et al., 2004). Examples of satellite stereoscopic geometries are nadir and backward looking sensors (e.g. ASTER), forward and backward looking sensors (e.g. SPOT-5 HRS), forward, nadir and backward looking sensors (ALOS PRISM), or sensors that can be freely rotated to any stereo geometry (e.g. Ikonos, WorldView, Pleiades), all of which are pushbroom or line scanners.

Satellite stereoscopy is slightly more complicated than traditional photogrammetry from aerial frame imagery due to the typical pushbroom acquisition strategies and to the greater effect of Earth's rotation and curvature from the higher flying height of satellites (Toutin, 2004; Käab, 2005). Image orientation may be solved from Ground Control Points (GCP) and a satellite orbital model (Toutin, 2004) that is implemented in commonly available software e.g. PCI Geomatica®. Automated approaches are becoming more common for deriving the relative and/or absolute orientation of stereo images using direct measurements of the satellite's attitude and position (i.e. pointing information, auxiliary and ancillary data) (for more details, see Schenk, 1999). Common examples of automatically generated satellite stereo DEMs that are available today include: the ASTER DEMs produced by LPDAAC using the SilcAst software (product AST14) (Fujisada et al., 2005) and the SPOT5-HRS DEMs (Bouillon et al., 2006; Korona et al., 2009), as for instance available through the IPY SPIRIT (SPOT 5 stereoscopic survey of Polar Ice: reference Images and Topography) project.

Errors associated with stereoscopic DEMs are related to the errors in the orientations of the stereo-scenes, either from GCP-based solutions or direct on-board determination, and to the ability of the matching algorithms to locate the corresponding points on two or more images. Errors in the parallax determination are both due to imperfect matching procedures and to imperfect image quality such as from lack of visible contrast, cloud cover, shadows and topographic distortions. Errors related to the parallax matching often result in blunders and voids rather than bias, whereas errors related to the image orientation will typically induce bias. ASTER DEM uncertainty is reported to be typically within 15 to 60 m RMSE in the vertical depending upon terrain type (Toutin, 2002, 2008; Käab et al., 2002; Hirano et al., 2003; Käab, 2005; Fujisada et al., 2005) and between 15 and 50 m horizontally (Fujisada et al., 2005; Iwasaki and Fujisada, 2005). SPOT5 uncertainty is reported to be between 10 and 25 m vertically (Berthier and Toutin, 2008; Korona et al., 2009) and greater than 15 m in the horizontal (Bouillon et al., 2006; Berthier and Toutin, 2008). In relation to pushbroom sensors (e.g. ASTER and SPOT5 HRS), it has been shown that variation in the satellite's attitude induces biases within the raw images acquired as well as final DEMs produced (Leprince et al., 2007; Berthier et al., 2007; Nuth and Käab, 2011).

5.2.2. Interferometric DEMs

Interferometric DEMs are generated through synthetic aperture radar (SAR) interferometry which uses the phase differences between two radar images acquired with a small base-to-height ratio. These phase differences are the photogrammetric equivalent to a "parallax" measurement allowing retrieval of topography (Rosen et al., 2000). Examples include the SRTM DEM, acquired in February 2000, which mapped the Earth from 60° N to 56° S using single-pass SAR interferometry (Farr et al., 2007), and the ongoing TanDEM-X Mission.

Many glacier elevation change studies have used the SRTM as a base dataset to compare to both newer and older data products (Rignot et al., 2003; Larsen et al., 2007; Schiefer et al., 2007; Paul and Haeberli, 2008). Typically reported vertical uncertainties of the dataset are $\pm 10\text{m}$ which is lower than the mission standards of $\pm 16\text{m}$ (Rodriguez et al., 2006). However, vertical biases are present due to instability of the sensor and/or platform (Rabus et al., 2003), and elevation-dependent biases have also been shown due to penetration of the C-band radar waves (centre frequency at 5.3 GHz) into snow and ice (Rignot et al., 2001; Berthier et al., 2006). Rignot et al. (2001) determined that the phase centre of the C-band signal return was 1 to 10 m into the surface depending upon the snow conditions (i.e. wet vs. dry) in Greenland and Alaska. In Svalbard, the volumetric phase centre of the C-band varied from 1 to 5 m along a profile from ablation to firn zones, respectively (Müller, 2011). Corrections for depth penetration are hardly used for the SRTM data, and it is extremely difficult to correct for as knowledge of the snow conditions at the time of acquisition is required but generally not available. Nonetheless, this bias is crucial to understand when interferometric DEMs are used in differencing. Future potential in determining this bias may entail the comparisons between the C-Band and X-Band SRTM datasets (e.g. Gardelle et al., 2012).

5.2.3. Laser scanning DEMs

DEMs generated from laser altimeters are at the present time typically restricted to airborne platforms and are therefore less widespread than satellite based DEMs. However, their accuracy is unprecedented and therefore provide great potential for glacier elevation changes (Geist et al., 2003; Geist et al., 2005; Aberman et al., 2010). Elevation acquisition from laser pulses is described in section 4.3.2. Laser scanning uses the same principles but collects data not only along a profile (as ICESat), but also across track (swath). Depending upon the flying height and sampling frequency, airborne laser scanners can typically acquire a horizontal point density on the order of 1-2 metres. The accuracy of the returned elevations are typically a function of the accuracy of the laser range determination and of the GPS position of scanner through time. Laser scanning DEMs are not globally available, and are only used as a secondary DEM source for those particular glaciers from which they are available.

5.3 Elevation changes from multi-temporal DEMs

Glacier elevation changes can be derived from multi-temporal DEMs through differencing. DEM differencing provides a more-or-less complete spatial representation of the glacier changes in height (provided no data voids), but has a coarse temporal resolution. This is because a greater time between data acquisitions is required to estimate significant changes due to the accuracy of the DEMs and due to seasonal elevation variations of the glacier surface as a result from accumulation and ablation. To compensate for both DEM accuracy and natural seasonal height variability, glacier elevation changes from DEM differencing are typically derived as long term averages (i.e. >5 years). The shortest period between successive DEMs is dependent upon the accuracy of the DEMs and the magnitude of the changes.

Glacier elevation changes are used for analyzing changes in the geometry of glaciers (Hagen et al., 2005) and for estimating volume and mass changes (Kääb, 2008; Berthier et al. 2010; Nuth et al., 2010), and possibly their relation to climate. However, the estimation of volume and mass changes requires some standard assumptions about the density of the changes which is difficult and rarely measured. Furthermore, an elevation change at a point on a glacier is the result of both climatic (surface mass balance) and dynamic (glacier flow) processes, and therefore a direct translation into responses induced by climate change is difficult. This is sometimes made easier when integrating all changes over individual glaciers (i.e. mean

elevation change thickness) as the dynamic component of ice submergence and ice emergence cancels due to mass conservation within a land terminating glacier system. For these land terminating glaciers, this has led to a large effort to control field derived surface mass balances of glaciers (Andreassen, 1999; Elsberg et al., 2001; Cox and March, 2004; Thibert et al., 2008), but also to provide control and calibration for surface mass balance models (Huss et al., 2009). However, if the glacier is marine terminating and contains ice loss to calving processes, the mean elevation change will include both the surface mass balance component as well as the component related to the calving loss of ice. In some instances, glacier elevation changes from DEM differencing have been combined with surface mass balance modelling to estimate the calving component to volume change (Nuth et al., 2011; Gardner et al., 2011). In summary, the algorithms presented for DEM differencing will focus on the **pre-processing** and generation of elevation changes, rather than the translation of elevation changes into volume and mass changes which require several assumptions.

While the approach of DEM differencing is straight-forward (i.e. subtraction of the older DEM from the newer DEM), the results of this differencing can be misleading due to bias in one or both of the DEMs and to the geometric co-registration of the DEMs to each other. DEMs can be generated from optical, radar or lidar data, and therefore variation in the errors and biases in any of these products may propagate into the elevation changes. Thus, the goals in terms of algorithms will be to outline the best procedures for (1) combining the various datasets and (2) for detecting and correcting (if possible) potential biases between the datasets. Further, we aim for universal procedures that can be highly automated and are flexible for the various input data sources used to generate differential DEMs.

5.4 Description of the algorithm chosen

5.4.1 Justification on the algorithm chosen

For DEM differencing, the elevation change algorithm is simply subtraction of the two grids and therefore requires little attention. The main algorithm for DEM differencing is for horizontal and vertical co-registering of the DEMs. This algorithm (DEM CR) was discussed in the ATBDv0 (Glaciers_cci, 2012a) and investigated together with other approaches during the round robin. In conclusion of the round robin and as documented in the PVASR (Glaciers_cci, 2012b), the co-registration algorithm presented in the ATBDv0 is found to be the most robust and efficient algorithm with similar reliability to other published approaches and thus is the most appropriate for Glaciers_cci. In addition, the analytical basis of the algorithm allows consistent application for multiple data types and sources in which the other algorithms experienced slightly worse reliabilities.

5.4.2 Algorithm overview

One of the DEMs will have to be re-sampled to the cell size of the other DEM. Any resampling technique more advanced than nearest neighbour should be used (i.e. bilinear interpolation), because nearest neighbour resampling, though retaining the original measurements, will inherently compare ground elevations representing different locations and areas (pixel sizes). Therefore, despite the smoothing of higher order interpolations (e.g. bilinear), these methods are necessary to ensure comparison of similar ground locations and areas in order to limit the effect of mis-registrations on DEM differences. We here focus on the pre-processing steps to improve the accuracy (remove bias) and precision of DEM differencing measurements.

The accuracy of glacier elevation differences from multi-temporal DEMs is dependent upon the individual accuracies of each of the DEMs and the geometric alignment between the DEMs. For DEMs that contain sufficient non-glacier terrain (e.g. > 10% of the scene), DEM difference statistics in this terrain, assumed stable within the time period, can be used for co-registration and bias-assessments. The initial (and universal) pre-processing step for deriving glacier elevation changes from DEM differencing is thus co-registration of the DEMs to each other. After co-registration, higher order biases can be investigated and removed if possible.

5.4.3 Mathematical description

Two DEMs of the same terrain surface that are not perfectly aligned experience a characteristic relationship between elevation differences and the direction of the terrain (aspect) that is precisely related to the x-y-shift (co-registration) vector between them. [Figure 5.1](#) shows a schematic drawing and a real example where one DEM is shifted to the second. Resulting elevation differences (dh) are larger on steeper slopes due to the relationship of the magnitude (a) of the shift vector and the elevation errors to the tangent of the slope of the terrain (α):

$$\tan(\alpha) = \frac{dh}{a} \quad (5.1)$$

For the assumed shift in x-direction, dh is positive on eastern and negative on western slopes, exemplifying the relationship between the shift direction and terrain aspect (Ψ). Because Ψ is usually defined circular from the north (azimuth), the direction of the shift can be modeled using a cosine of the difference between Ψ and the horizontal directional component of the co-registration vector. Combining this with the relation described by Eq. 5.1 derives the full analytical solution by relating the elevation differences to the elevation derivatives slope and aspect (Kääb, 2005):

$$dh = a \cdot \cos(\Psi - \psi) \cdot \tan(\alpha) + \overline{dh} \quad (5.2)$$

where dh is the individual elevation difference, a is the magnitude of the horizontal shift, ψ is the direction of the shift vector, α is the terrain slope, Ψ is the terrain aspect and \overline{dh} is the overall elevation bias between the two DEMs. Slope and aspect can be calculated by any standard GIS or mathematical software, and different approaches exist depending upon application. In this case (photogrammetric DEMs), the finite difference method is more appropriate than the D8 method, but for other DEMs (e.g. derived from contourlines) it might be vice versa (cf. Wilson and Gallant, 2000). To remove the error dependency on slope due to a geometric mis-registration, we normalize the vertical deviations by dividing by the tangent of slope at that pixel. This produces a clean sinusoidal relationship between elevation difference and aspect ([Fig. 5.2](#)). The transformation of Eq. 5.2 after slope normalization is:

$$\frac{dh}{\tan(\alpha)} = a \cdot \cos(\Psi - \psi) + c \quad (5.3)$$

where:

$$c = \frac{\overline{dh}}{\tan(\overline{\alpha})} \quad (5.4)$$

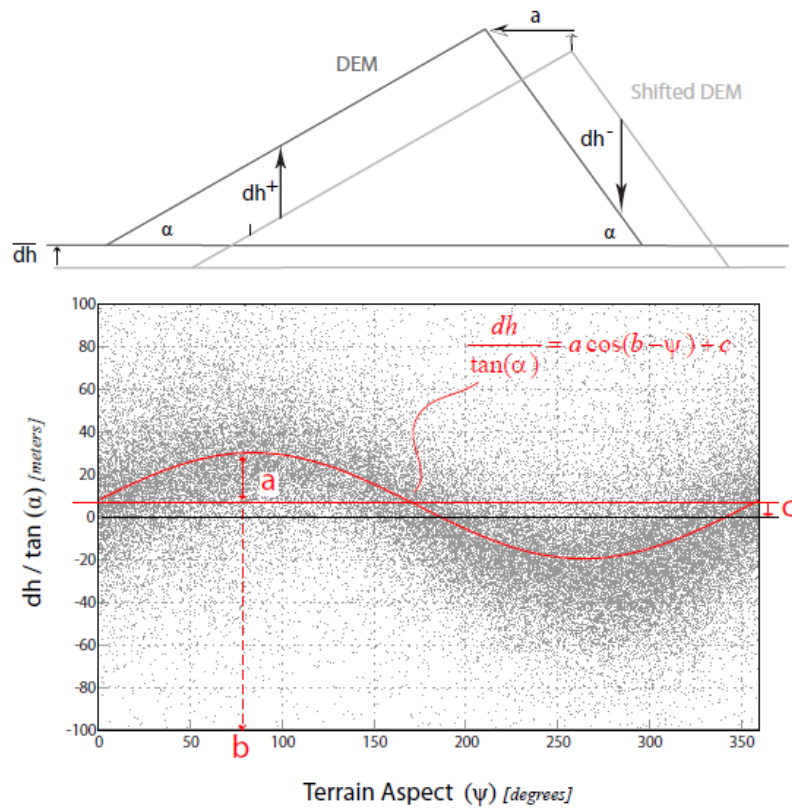


Fig. 5.1: Top: 2-D scheme of elevation differences induced by a DEM shift. Bottom: The scatter of elevation differences between two DEMs showing the relationship between the vertical deviations normalized by the slope tangent (y-axis) and terrain aspect (x-axis). The equation for the solved sinusoidal curve fit is shown along with the three unknown solution parameters a , b and c . Reproduced from Nuth and Kääb (2011).

Three cosine parameters (a , b and c) are solved using least squares minimization where the amplitude of the cosine (a) is directly the magnitude of the shift vector, b is the direction of the shift vector and c is the mean bias between the DEMs divided by the mean slope tangent of the terrain. Because the solution to this analytical relationship is solved using the terrain which is not an analytical surface, the first solution may not be the final solution and iteration of the process is required to arrive at an ultimate solution. For automation, the iteration is halted when the improvement of the standard deviation is less than 2% or if the magnitude of the solved shift vector is less than 0.5 m (other values are possible, but might require more iterations). The final correction is applied to the corner coordinates of the un-registered DEM by solving the x- and y-components of the shift vector from the magnitude (a) and direction (b). The mean bias determined by inverting Eq. (5.4) is added to the DEM using an estimate of the mean slope of the terrain (α) used to solve Eq. (5.3):

$$\begin{aligned}
 x_adjustment &= a \cdot \sin(b) \\
 y_adjustment &= a \cdot \cos(b) \\
 z_adjustment &= c \cdot \tan(\bar{\alpha})
 \end{aligned}
 \tag{5.5}$$

The co-registration procedure outlined here is not restricted to DEMs, but to datasets that contain a sufficient amount of stable non-glacier terrain to solve with Eq. (5.3). In particular, ICESat can be used for this despite the smaller amount of points available (Nuth and Kääb, 2011). This provides a framework for global co-registration using ICESat as a reference. Last, alternate methods for co-registration involve the basic principles in image matching techniques, but use entire DEMs rather than sub-image search windows (e.g. Berthier et al., 2007). The algorithm may be useful in situations where the terrain slope is low over the entire scene (i.e. < 5 degrees) and the aspect distribution is not close to uniform rendering the analytical solution (equation 5.3) un-solvable.

5.4.4 Description of the processing line

Figure 5.2 outlines the processing scheme for DEM co-registration. The general procedures for DEM co-registration are:

- *Pre-Processing*: Selection of suitable terrain for input into the DEM co-registration routine. Suitable terrain is defined as stable and unchanging, i.e. outside glaciers, no water bodies, no clouds or data voids and assuming limited vegetation effects. This terrain is further used for both determining the co-registration parameters and later for validation of products and accuracy quantification. This choice of stable terrain is an implementation procedure that leads to variations in the accuracy.
- *Co-Registration*: DEM co-registration with the algorithms described in section 5.5. Adjustment of the slave DEM to the master DEM using the co-registration parameters.
- *Resampling*: Resample one DEM to another, and matrix difference the two aligned DEMs. Use the selected stable terrain for product validation and accuracy assessment. Estimation of random and systematic uncertainties in the final DEM difference grids.

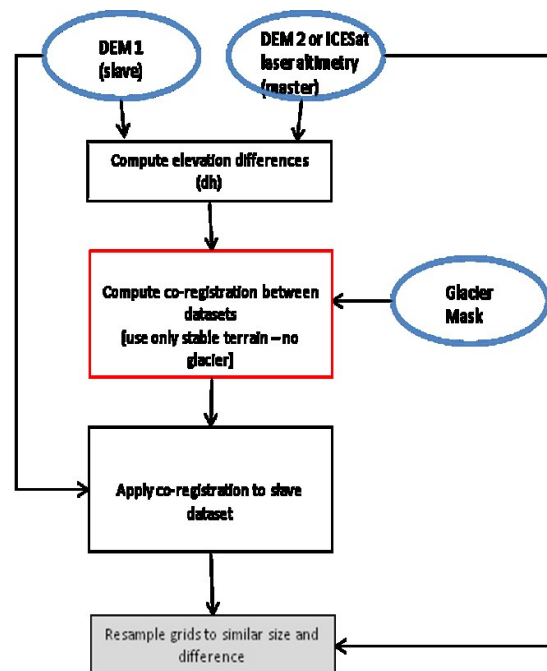


Fig. 5.2: Flow chart for the elevation change – DEM differencing algorithm to be used. Input data is denoted by blue circles and may either be DEMs or ICESat laser altimetry. Also required is a glacier mask to determine stable terrain from which to apply the DEM co-registration algorithm. The output denoted as a grey shaded box may either be the raw co-registration parameters, the co-registered slave DEM, or a resampled difference DEM.

5.5. Input data and algorithm output

The input data required for DEM co-registration is a slave DEM (to be co-registered) and a master DEM or laser altimetry (i.e. ICESat). Auxiliary input data required is a glacier mask to separate stable terrain pixels from un-stable terrain (i.e. glacier) pixels. The geolocation accuracy of this dataset is uncritical, as outlines are buffered to be on the safe side. Once separated, the co-registration algorithm is then operated on the appropriate (non-glacier stable terrain) pixels. The output to the DEM co-registration tool are the co-registration parameters in the x, y, and z directions, that can be applied by the user directly. Alternatively, a DEM co-registration tool may also be able to apply the co-registration and export a new DEM, directly. Outputs may also include an additional processing step to resample the DEMs to co-incident grids (requires interpolation) and further export an elevation difference grid (including glaciers and stable terrain) from which the user can assess glacier specific changes. We note that elevation difference grids of the glaciers alone (without the surrounding stable terrain) will not allow for error analysis by the individual users.

5.6 Error budget estimates

The error budget of glacier elevation changes is in practice defined by the combination of the individual accuracies of the DEMs and may be estimated through either physical or statistical error modelling. Statistical error modelling is more robust, complete, and easier to implement. This error budget typically is composed of random errors estimated by the standard error of the non-glacier terrain elevation differences after accounting for the degree of spatial autocorrelation. On top of this, the unknown systematic errors must be added. Parts of this uncertainty can be extracted through the co-registration of 3 or more DEMs, and subsequent sum of co-registration vectors (details in the PVASR Glaciers_cci, 2012b). Ultimately, internal DEM bias may significantly affect the error of glacier elevation changes, but may be difficult to detect and quantify. A prime example is that of satellite jitter in, for example, ASTER DEMs.

5.7 Expected accuracy

We estimate the reliability of the co-registration algorithm to return parameters as accurate as 1/10th a DEM pixel but certainly not worse than 1/3rd a pixel. Further investigation is required into the choice of stable terrain implemented and used for DEM co-registration as this affects the individual accuracies of the co-registration, the estimated errors for elevation difference grid products and the mean elevation changes that may be derived from them. It is highly important that the entire processing chain remain within one software. Within the round robin experiments, some contributions provided very accurate co-registrations, though the triangulation of co-registration vectors between 3 datasets revealed problems with the internal pixel definition (pixel centre vs. pixel corner) within the contributors processing chains as documented in the PVASR (Glaciers_cci, 2012b). This failure to maintain proper pixel definition counter-acts the accuracy of the co-registration correction and the bias remains within glacier elevation changes even if considered removed. In addition, the choice of resampling is highly important, and should always be more sophisticated than nearest neighbour as this will also re-induce mis-alignments in the DEMs, and thus bias. The resampling procedures used for glacier elevation change products from DEMs of varying resolutions requires more investigation, though first results from the round robin imply that up-sampling to higher resolutions will lead to artefacts related to terrain curvature while down sampling to lower resolutions minimizes these effects.

5.8 Practical considerations for implementation

The co-registration algorithm presented here is the analytical solution to correct for a linear mis-registration between two DEMs, or elevation data sources. It is operational on continuous DEM products and also in combination with sparse laser altimetry (e.g. ICESat). The algorithm fails on low sloping surfaces (e.g. less than 3-5 degrees) and in situations where the aspect distribution is not uniform over at least 180 degrees of aspects. In these situations, some previous image matching based co-registration algorithms may be used (Berthier et. al. 2007). The number of iterations required to find a global minimum solution is on average between one and four. Computational effort will increase exponentially with the size of the DEM, so a subset might be selected to find the co-registration parameters.

6. Algorithms for Glacier Velocity

6.1 Introduction

A large number of archived and upcoming optical and SAR satellite missions make it now possible to operationally map and monitor glacier flow on a nearly global scale. Deriving glacier displacements globally will provide unique glaciological information (Heid and Kääb, 2012a and b). It will make it possible to compare spatio-temporal variations of glacier velocities both within regions (e.g. Fig. 6.1) and between regions. Such knowledge will enable better understanding of a wide range of processes related to glacier mass fluxes, such as glacier response to climate and climatic changes, glacier physics and flow modes, glacier flow instabilities (e.g. surges), subglacial processes (e.g. erosion), supra- and intra-glacial mass transport, etc. Knowledge about glacier ice supply helps to understand the development of glacier lakes and associated hazards (Kääb et al., 2005). Mapping and monitoring glacier flow globally perfectly complements current attempts for mapping and monitoring glacier areas and glacier volume changes on a global scale within Glaciers_cci and other projects (GLIMS, GlobGlacier).

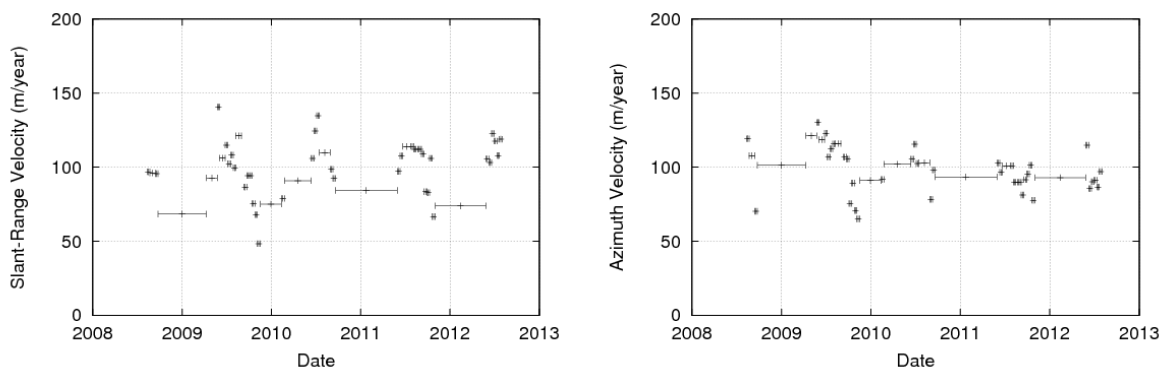


Fig. 6.1: Variations of surface speeds from repeat TerraSAR-X data over Aletschglacier, Swiss Alps, along (left) slant-range and (right) azimuth direction.

Within the Glaciers_cci project, the generation of ice motion fields of glaciers is performed using high and very-high resolution repeat-pass SAR images and medium to high-resolution optical satellite data. In the case of images from a single look direction none of these methods is capable of directly measuring the full 3-D ice velocity vector which is of interest for ice dynamic studies. Additional assumptions on the ice flow can be introduced to provide ice velocity information directly applicable for glaciological tasks. In general, a surface-parallel ice flow is assumed where the slope is derived from a low-pass filtered DEM. As an effect, displacements from SAR and optical methods cannot be compared directly, unless they are projected to a common geometry. This step involves assumptions and auxiliary data (in particular DEMs).

The suitable temporal baselines of the repeat data are defined by two fundamental constraints:

- The displacements have to exceed the accuracy of the method, i.e. have to be statistically significant;

- The surface changes such as melt, deformation, phase coherence loss, etc. over the measurement period have to be small enough so that corresponding intensity or phase features can be matched in both data sets.

Typical temporal baselines suitable for optical data are up to 1-2 years, for SAR offset-tracking up to a few weeks (depending on magnitude of ice flow and stability of available features), for SAR interferometry a few days (Glaciers_cci, 2011b). In the optical domain, tracking methods are usually called '**image matching**', in the microwave domain '**offset tracking**'. Here we use the term offset-tracking for both optical or SAR data.

This chapter provides an overview on the methods for retrieving ice motion fields from SAR and optical satellite data considering the results of the round robin and including the boundary conditions applied to transform satellite-derived displacement to surface ice velocity products. In response to the User Requirement Document (URD, Glaciers_cci, 2011a) and the surveys conducted in the requirement definition process, the main focus is on raw displacements derived from multi-temporal image pairs in UTM or geographic projection, i.e. without projection to a certain flow direction.

6.1.1 SAR data

The generation of ice motion fields of glaciers is performed using repeat-pass images acquired by high and very-high resolution SAR satellite data. SAR data have the advantage of an active sensor that is not affected by solar illumination (day/night) or cloud coverage. Moreover, the acquisition geometry, satellite orbit and the technical sensor properties are well defined and stable, enabling precise analysis of repeat-pass images which are required for retrieval of glacier motion. The penetration depth of microwaves in dry snow and ice is on the order of a few metres to more than 100 m, depending on the radar frequency and snow and ice purity and structure (Ulaby et al., 1982; Maetzler, 1996; Rignot et al., 2001). While radar methods detect a mixture of surface and sub-surface features, they are generally referred to as measurement of glacier surface flow.

Depending on the available SAR data in terms of spatial resolution and temporal sequence of repeat passes, two primary methods evolved during recent years to retrieve the surface ice motion field. The methods discussed here are:

- (1) Across-track Interferometric repeat-pass SAR (InSAR) analysis, delivering the velocity component in radar line-of sight (LOS), and
- (2) SAR Image offset tracking: this encompasses various methods, including the cross-correlation of chips in amplitude or complex SAR images and coherence optimization. Both methods provide velocity components in LOS and along-track and do not require phase-unwrapping, but are less sensitive to displacement than InSAR. Depending on the employed algorithm they require distinct features, like crevasses, or coherence.

In their raw form, SAR offset-tracking provides 2-dimensional displacements in SAR geometry, i.e. in the azimuth and slant-range system, and SAR interferometry provides 1-dimensional displacements in the line-of-sight (LOS) direction between the ground points and the satellite positions.

6.1.2 Optical data

Surface displacements from repeat optical data are usually performed on orthorectified and projected images so that the displacements are directly in the coordinate system aimed at. The method applied in most cases is block-matching (in contrast to feature matching) where a maximum similarity of an image template is searched for in the second image using image chips (also called templates). The techniques used for that purpose are similar, in parts identical, to the amplitude offset tracking described before (section 6.1.1). A main difference between optical and SAR matching algorithms lies in their ability to cope with the large noise level in SAR images (radar speckle) (Debella-Gilo and Käab, 2012).

A second major difference which is relevant for offset tracking, is the different sensor and thus image geometry. Most optical data used for this purpose are nadir looking, with, for instance, similar pixel resolutions over the image and little effect of elevation changes and errors, whereas both effects play a significant role in the side-looking geometry of SAR data. In their raw form, optical orthoimages provide the 2-dimensional horizontal displacement component in a given map coordinate system. They are sensitive to surface features only.

6.2 Scientific background

6.2.1 Ice motion fields from SAR

The general steps of a processing line for ice motion retrieval from repeat-pass SAR data, including InSAR and offset tracking, are outlined in [Fig. 6.2](#). As input a data stack of multi-temporal repeat pass SAR images and a DEM is needed. Accurate co-registration of the repeat pass SAR images is an important step for further analysis and has to be performed with high accuracy. Depending on the software implementation of the co-registration module different steps are applied including geometrical co-registration based on orbit and imaging parameters only, coarse-co-registration with pixel-accuracy using a DEM or not and sub-pixel co-registration using stationary regions or points available in both images. In the latter methods it is important to mask out potentially non-stationary areas like glaciers or water surfaces in the co-registration process. The precisely co-registered SAR image stacks are fed into the InSAR and offset-tracking modules for retrieving ice displacements. After performing InSAR or offset-tracking the derived displacement component in radar geometry has to be resampled to the preferred map projection and can be converted to ice velocity maps.

The criteria used for algorithm selection within the Glacier_cci project were robustness, reliability and accuracy. This led to the selection of the intensity-cross correlation algorithm. The phase-based SAR methods (fringe-visibility, InSAR and MAI) show some inherent drawbacks which lead to a rejection of these algorithms for ECV production:

- Coherence

The availability of coherent SAR data represents the main limitation. Glacier surface processes like summer melt cause total decorrelation between consecutive images. Further, short satellite repeat-cycles are a prerequisite for coherent images even in winter, and the current satellite missions do not fulfil this criterion.

- Phase unwrapping

The process of phase unwrapping, translating phase shifts into actual motion values, is very costly and prone to errors. For example, it requires intensive interaction of a skilled operator, and fails with strong velocity gradients.

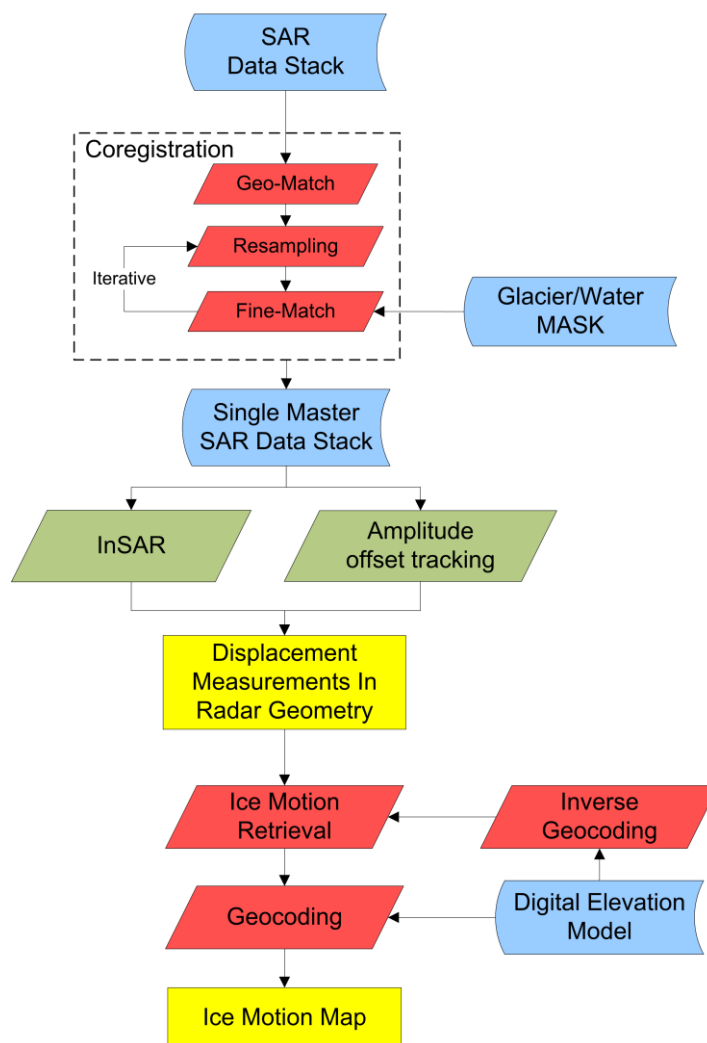


Fig. 6.2: Overview of general steps for ice motion retrieval from SAR data. SAR Interferometry and amplitude offset-tracking using SAR data.

6.2.1.1 Ice motion fields from offset-tracking

Offset-tracking is employed in order to provide ice surface motion when the signal in the repeat-pass SAR image pair is not coherent. After the common co-registration, outlined in Fig. 6.2, the displacement is measured by applying various algorithms. One of the most commonly used is the normalized cross-correlation coefficient (NCC) of amplitude image chips according. Depending on the implementation there might be some overlap between the search and reference windows implicitly resulting in some low-pass filtering as the image windows are not completely independent. The NCC kernel provides image offsets in slant-range (LOS) and azimuth (along-track) direction. Optionally the Correlation Relaxation Labelling (CRL) technique can be applied to check for outliers in the displacement field. CRL provides the opportunity to check the consistency of a NCC image offset retrieval by comparing the results to neighbouring NCC results (Wu, 1995). If the result is not consistent with the neighbourhood it will be rejected. In general, the best performance of the NCC kernel can be expected in regions with pronounced surface features such as crevasses, drainage channels and surface moraines, but it also works where speckle (and thus coherence) is retained.

In comparison to SAR interferometry, offset-tracking techniques have various drawbacks. Comparatively large image patches ($> 64 \times 64$ pixels) are needed to retrieve a single motion vector, which excludes the application ERS SAR or ASAR on small glaciers. Distinct features (including speckle) need to be present on the glacier surface that move with the glacier and are preserved over months or years and in accumulation areas such features are usually missing. The offset-tracking techniques are significantly less sensitive to displacement than InSAR which results in larger error bars. However, this improves with the new high resolution spaceborne SAR systems such as TerraSAR-X and Cosmo-Skymed.

Alternatively to the NCC parameter for determination of the displacement other statistical parameters can be applied, including a complex-correlation of SAR images and coherence optimization. The computational burden and performance of these algorithms are different to those of the NCC, but the above mentioned characteristics remain valid.

6.2.1.2 Retrieval of glacier surface velocity by SAR

The displacement of a particle on the glacier surface during a time interval, T , is described by the three-dimensional displacement vector \mathbf{d} :

$$\mathbf{d} = d_x \hat{\mathbf{x}} + d_y \hat{\mathbf{y}} + d_z \hat{\mathbf{z}} = \mathbf{d}_h + d_z \hat{\mathbf{z}} \quad (6.1)$$

Normalizing the displacement by the time interval, T , between the two image acquisitions the velocity vector \mathbf{v} , is given by:

$$\mathbf{v} = v_x \hat{\mathbf{x}} + v_y \hat{\mathbf{y}} + v_z \hat{\mathbf{z}} = \mathbf{v}_h + v_z \hat{\mathbf{z}} \quad (6.2)$$

$\hat{\mathbf{x}}$, $\hat{\mathbf{y}}$, and $\hat{\mathbf{z}}$ are the unit vectors in the Cartesian coordinate system. The orientation of the coordinate system can, for example, be selected according to a specified map projection. In the following the x-coordinate is assumed to correspond to easting (E), the y-coordinate to northing (N), and the z-coordinate upward perpendicular to the local geoid surface. The three components of the vector can be re-arranged to separate the vertical displacement component d_z and the horizontal displacement vector \mathbf{d}_h . The vertical displacement (elevation change) at the glacier surface represents the net effect between the ablation/accumulation and emergence/submergence velocity of the ice at a given location. On land terminating glaciers in retreat, the emergence velocity in the ablation area is usually rather small. During summer the ablation dominates over emergence as well as on glaciers that are in balance over the year, causing the surface to subside. Mass balance assessments of glaciers and ice sheets by flux divergence calculations require at least the two-dimensional horizontal surface velocity pattern (Mohr and Madsen, 1996). The knowledge of the full 3D flow pattern is required for some ice dynamical studies and the validation of ice flow models, but not provided by Glaciers_cci. Other approaches are able to account for individual velocity components.

Figure 6.3 shows the imaging geometry of SAR and the velocity / displacement components. Repeat pass SAR enables two main methods for mapping ice displacement, Differential SAR Interferometry (DINSAR) and incoherent amplitude offset tracking. DInSAR measures only the displacement in radar look direction (LOS) during the time interval between the acquisitions of two SAR images. However, surface deformations may occur in vertical or horizontal direction, along the surface gradient, in the local surface plane, but also in any other directions. Strictly speaking, a single SAR interferometric observation does not allow for full determination of the magnitude and direction of a surface deformation, but only allows an observation of the deformation component along the radar look direction.

As the vertical component affects the slant range displacement, two cases can be distinguished depending on the imaging geometry relative to the flow direction of the glacier.

- *horizontal displacement towards near range and downward vertical displacement:* without taking the vertical component into account, the observed pixel shift in slant range direction derived from offset-tracking is reduced relative to the “true” horizontal displacement
- *horizontal displacement towards far range and downwards vertical displacement:* without taking the vertical component into account, the observed pixel shift in slant range direction derived from offset-tracking leads to an overestimation of the horizontal displacement relative to the “true” horizontal displacement

In the interpretation of ice displacement fields of glaciers with changing ice flow direction the discrimination of the two cases is particularly important.

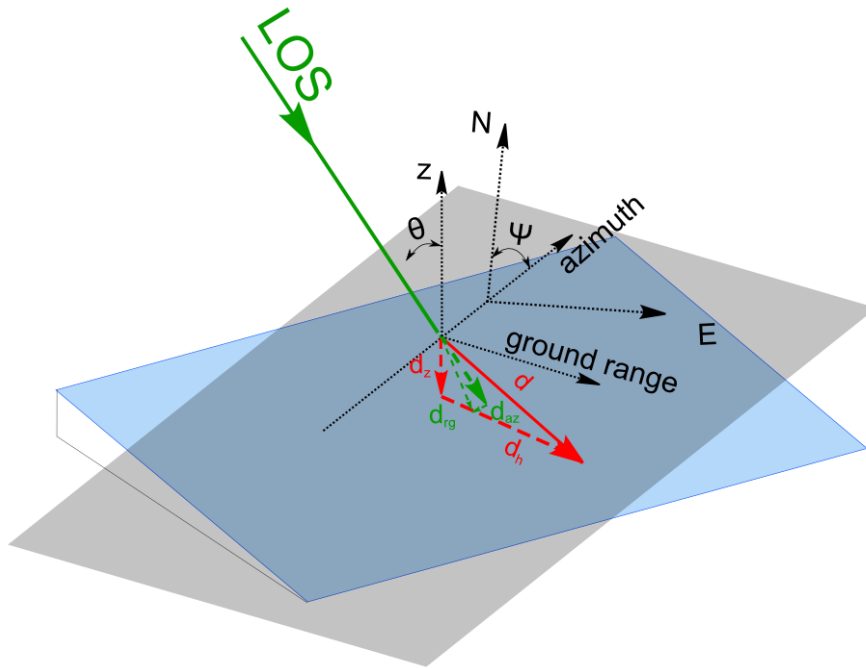


Fig. 6.3: Sketch of the geometry of spaceborne SAR observations with 3D displacement vector (d). With d_h : the horizontal displacement component, d_z : the vertical displacement (elevation change), d_{az} and d_{rg} : are the displacement components in azimuth and range direction in SAR slant range coordinates, respectively, θ : the off-nadir angle, and ψ the azimuth angle (defined as the angle between North and along-track direction).

For the description of a displacement in look direction (line-of-sight) we select the polar coordinates in the geocoded (map) geometry. We characterize the displacement vector in look direction $\mathbf{v} = (v_x, v_y, v_z)$ by its magnitude d , elevation angle ν and orientation angle φ :

$$\begin{aligned}
 v_x &= d \cdot \cos \nu \cdot \sin \varphi \\
 v_y &= d \cdot \cos \nu \cdot \cos \varphi \\
 v_z &= d \cdot \sin \nu
 \end{aligned}
 \tag{6.3}$$

For a displacement component v in look direction, the possible displacement vectors are in a plane perpendicular to the look vector direction intercepting the look vector at a distance r . The equation of a plane perpendicular to a vector $\mathbf{v} = (v_x, v_y, v_z)$ is given by:

$$v_x x + v_y y + v_z z = r^2 \quad (6.4)$$

where x , y and z are the Cartesian coordinates of the 3-dimensional displacement vector, with the x coordinate corresponding to the east direction, the y coordinate to the north direction and the z coordinate pointing upward.

The relationship between the Cartesian (x, y, z) and polar coordinates (r, ν, φ) is given by (DMK/DPK, 1977):

$$\begin{aligned} r &= \sqrt{x^2 + y^2 + z^2} \\ \sin \nu &= \frac{z}{r} \\ \cos \varphi &= \frac{x}{r} \quad \sin \varphi = \frac{y}{r} \end{aligned} \quad (6.5)$$

If only one measurement from one look direction is available, the 3-dimensional displacement vector can be only computed if a displacement or “flow” direction is known. We represent this flow direction by the unity vector $\mathbf{f} = (f_x, f_y, f_z)$ defined by its elevation (slope) angle ν_f and its orientation angle φ_f :

$$\begin{aligned} f_x &= \cos \varphi_f \sin \nu_f \\ f_y &= \sin \varphi_f \sin \nu_f \\ f_z &= \cos \nu_f \end{aligned} \quad (6.6)$$

Displacement in the flow direction of \mathbf{f} means that the displacement is on the straight line defined by the equations:

$$\begin{aligned} x &= c \cdot f_x \\ y &= c \cdot f_y \\ z &= c \cdot f_z \end{aligned} \quad (6.7)$$

In this case the system of equations to solve for the displacement vector is given by equation (6.7) (in the case of a measurement from a descending track). The system can only be solved if flow and look directions are not perpendicular to each other, because in this case the SAR measurement is not sensitive to the displacement. The magnitude r of the 3-dimensional displacement vector can be computed by:

$$r = \frac{v}{\sin \theta} \quad (6.8)$$

where r_d is the magnitude of the displacement in the look direction of the SAR and $\theta_d = (90^\circ - \nu_d)$ and φ_d are the incidence and orientation angles, respectively, of the SAR observation.

SAR data are often acquired in two independent look directions, those of ascending and descending tracks. In this case, only one additional restriction of the deformation geometry is required. Typical restrictions are displacement in horizontal direction or along the surface plane. For the 3-dimensional interpretation of measurements of ascending and descending tracks, it is suitable to first characterize the two available displacement components and then to combine them with an assumption about a third direction.

In order to obtain a 3-dimensional deformation vector field, observations from three different look directions are required. However, SAR data are only acquired in two independent look directions, those of ascending and descending tracks. As a consequence, an additional restriction of the deformation geometry is needed. In many cases the knowledge of the deformation process allows to find such a geometric restriction. Typical restrictions are displacement in vertical or horizontal direction or along the surface plane. For the 3-dimensional interpretation of measurements of ascending and descending tracks, it is suitable to first characterize the two available displacement components and then to combine them with an assumption about a third direction.

Displacement components r_a measured in the look-direction of SAR data acquired in ascending mode (elevation angle ν_a and orientation angle φ_a) and r_d measured in the look-direction of SAR data acquired in descending mode (elevation angle ν_d and its orientation angle φ_d) result in plane equations:

$$a_x \cos \varphi_d \sin \nu_d + a_y \sin \varphi_d \sin \nu_d + a_z \cos \nu_d = r_d \quad (6.9)$$

where the x , y , and z components of the vector $\mathbf{a} = (a_x, a_y, a_z)$ are:

$$\begin{aligned} a_x &= r_d \cos \varphi_d \sin \nu_d \\ a_y &= r_d \sin \varphi_d \sin \nu_d \\ a_z &= r_d \cos \nu_d \end{aligned} \quad (6.10)$$

and

$$d_x \cos \varphi_d \sin \nu_d + d_y \sin \varphi_d \sin \nu_d + d_z \cos \nu_d = r_d \quad (6.11)$$

where the x , y , and z components of the vector $\mathbf{d} = (d_x, d_y, d_z)$ are:

$$\begin{aligned} d_x &= r_d \cos \varphi_d \sin \nu_d \\ d_y &= r_d \sin \varphi_d \sin \nu_d \\ d_z &= r_d \cos \nu_d \end{aligned} \quad (6.12)$$

Typical elevation angles of SAR data are between 70° and 50° (in this context the displacement vector in look direction points upwards). As the vertical component of motion is much smaller than the horizontal ones, we can set vertical component to zero:

$$z = 0 \quad (6.13)$$

Equations (6.9) and (6.11) form a system of two equations which can be solved for the two unknowns x and y representing the east and north coordinates of the displacement vector. The assumption of displacement along the surface normal can be useful in glaciology when flow is

nearly parallel to the surface of the glacier. The unity surface normal vector \mathbf{n} (i.e. perpendicular to the surface) is computed from a DEM and can be expressed with its orientation and elevation angles ν_n and φ_n , respectively, as:

$$\begin{aligned} n_x &= \cos \varphi_n \sin \nu_n \\ n_y &= \sin \varphi_n \sin \nu_n \\ n_z &= \cos \nu_n \end{aligned} \quad (6.14)$$

Displacement along the surface plane means that the displacement is on a plane perpendicular to \mathbf{n}

$$\mathbf{n} \cdot \mathbf{d} = 0 \quad (6.15)$$

Equations (6.9), (6.11) and (6.12) are a system of three equations for the three unknown x , y and z representing the Cartesian coordinates of the displacement vector.

SAR offset-tracking provides the shift of features in slant range and azimuth (across track) direction. As for InSAR, using data of ascending and descending orbits, an additional restriction about the deformation geometry is required. The displacement vector in slant range, \mathbf{r}_g , and azimuth direction, \mathbf{d}_{az} , observed at a pixel, is related to the 3D displacement on the Earth surface according to

$$\begin{aligned} v_x &= |\mathbf{r}_{LOS}| \sin \nu \cos \varphi + |\mathbf{r}_{az}| \sin \varphi \\ v_y &= |\mathbf{r}_{LOS}| \sin \nu \sin \varphi + |\mathbf{r}_{az}| \cos \varphi \\ v_z &= |\mathbf{r}_{LOS}| \cos \nu \end{aligned} \quad (6.16)$$

The azimuth shift observed by offset-tracking is not sensitive to the vertical component of the displacement that is observed in the ablation zone of glaciers with significant ice melt (causing a net-decrease of surface elevation) and can thus be converted directly into horizontal motion. The slant range shift observed by offset-tracking includes both the horizontal and vertical motion, which cannot be resolved without additional information.

6.2.2 Surface displacements from repeat optical data

Surface displacements from optical data are derived by finding similarities between two (or more) images. A general flow chart for the processing is shown in Fig. 6.4. Even if in some cases feature-based methods can provide good results, block-matching techniques are preferred due to the typical glacier surfaces that often lack distinct geometric features such as crevasses, but rather contain less sharp radiometric features, e.g. from dust or debris deposits. The selected offset-tracking algorithms are listed in section 6.4. The main difference between the design of offset-tracking algorithms for SAR amplitude images and optical images are the higher robustness against noise (radar speckle) that SAR offset-tracking algorithms need to have. Thus, the same principles can be used for both types of images, but with different parameterisations (e.g. template size), and different evaluation criteria for their performance. Due to that, the different sensors used, the different pre-and post-processing procedures, and, importantly, the different imaging geometries and, thus, sensitivities to geometric errors, offset tracking based on optical and SAR data are treated in separate chapters.

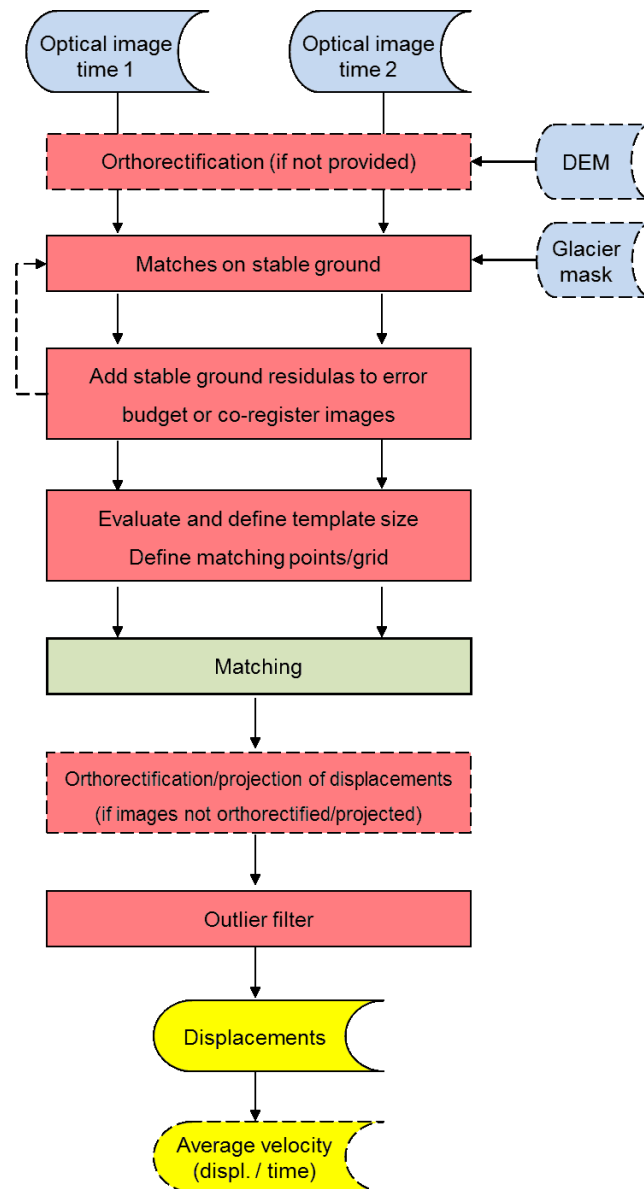


Fig. 6.4: Flow chart for glacier velocity from repeat optical images.

Usually, orthorectified optical data will be matched so that the raw displacements are already in the desired projection. A proper orthorectification is therefore crucial to the positional accuracy of the matches. The main error influences to orthoprojection are errors in the sensor position and attitude information (either in the auxiliary data or from orientation based on ground control points) and propagated elevation errors from the DEM used for orthoprojection. Offsets on stable ground allow definition of the level of propagated DEM errors, and for evaluation and partial correction of orientation errors. Though, it is crucial to keep in mind that these errors, in particular the propagated DEM errors, cannot be simply corrected by coregistration because the misregistrations are not linear (also not linear in the sense of a higher order polynomial). Rather, stable ground offsets give the background error to be expected from the matches on the moving glacier and to be added to the total error budget.

Since displacements are usually tracked from orthoprojected images, the tracked positions can be defined as a raster in e.g. UTM or geographic coordinates, or as points of special interest, for instance positions of ground measurements, such as GNSS, or fixed positions or flux gates

for time series analysis. The matching template sizes can be chosen after iterative tests on the images, or from a list of typically optimal sizes for specific image types and resolutions. An automatic choice is in principle possible, but very time consuming and only particularly effective for high-resolution data, less for medium resolution such as Landsat (Debella-Gilo and Kääb, 2012). The matching itself is to find in image of time 2 the most similar location to a template of image of time 1 (Fig. 6.5). The available algorithms differ among others in the similarity measure and the normalisation used.

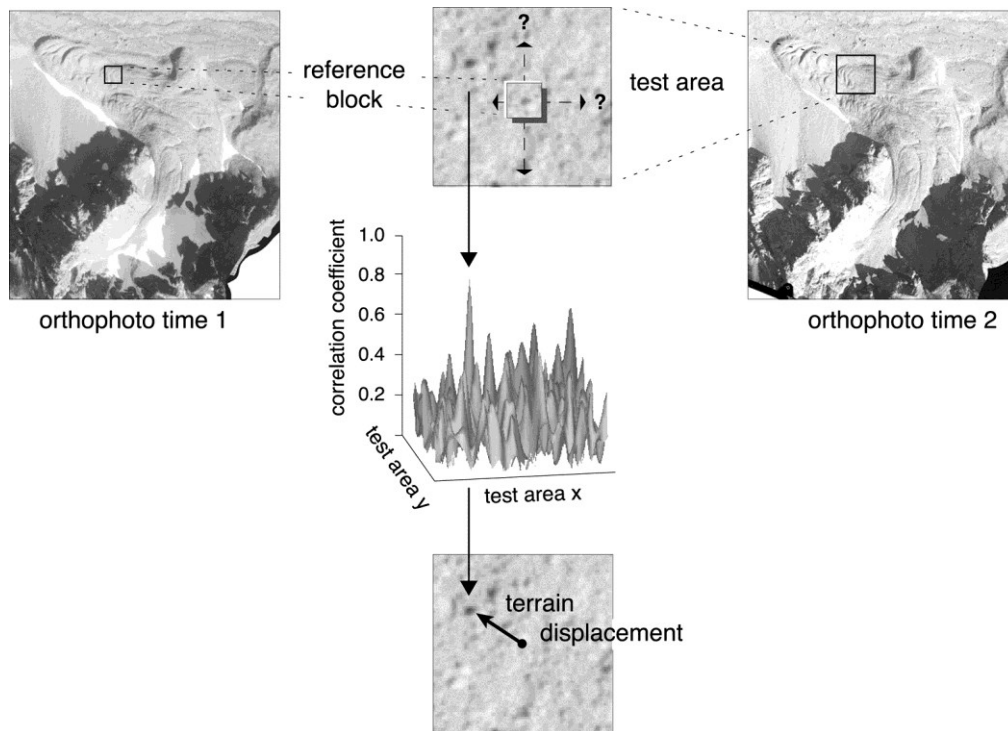


Fig. 6.5: Principle of matching between two repeat optical orthoimages within the offset-tracking process.

In the case the input images have not been orthorectified beforehand, the tracked displacements would have to be projected/orthorectified. This step requires reconstruction of the acquisition geometry and in most cases heavy operator interaction and specialized processing software. Glaciers_cci does not therefore work with un-orthorectified optical images before the offset tracking process. The raw displacements can be filtered for outliers, and average velocities be computed over the observation time period. The final displacements/velocities are horizontal movement components in the projection chosen for the orthoimages. This projection can be easily changed in standard software as the displacements are point information with attributes.

6.3 Justification on the algorithm chosen

The purpose of the round robin was to compare algorithms and their potential embedding in a processing system with robust global-scale applications based on varying sensors in mind, rather than a review of the algorithms themselves on the strictly technical level (e.g. comparing advanced filtering methods for displacements). Moreover, projections to different three-dimensional movement components are not analysed, as the users prefer raw

displacements in UTM or geographic projection. Hence, the main evaluation criteria for the assessment of glacier offset-tracking methods were:

- robustness of the method under different surface conditions;
- robustness of the method under different sensor resolutions (high & medium resolution);
- robustness of the method under different imaging frequencies (X-, C-, L-band);
- suitability of the method for a high degree of automation;
- accuracy requirements as outlined in the PSD (Glaciers_cci, 2011b);
- user requirements as outlined in the URD (Glaciers_cci, 2011a).

The round robin for the optical data suggest that no one matching method clearly outperforms all other methods investigated under all circumstances, but rather that a set of two methods should be combined depending on the image conditions and the glacier characteristics. Based on the evaluation criteria and algorithm comparisons the further steps (algorithm implementation, etc.) will be based on NCC and CCF-O. The normalized cross-correlation in spatial domain (NCC) is a matching method that is often used when studying glacier velocities. This is much due to its simplicity and robustness. The first image is taken as the reference image and a template out of this image is searched for in the second image, or the search image. The peak of the cross-correlation surface indicates the displacement between the images. This cross-correlation is normalized.

The NCC algorithm is simple and robust and can be applied to both optical and SAR data. As a consequence of the normalization of images with different illumination conditions the correlation coefficient from different correlation attempts can be compared. The original precision of this algorithm is only on the pixel-level, but this can be improved by interpolation of the correlation peak or image template interpolation beforehand correlation. Because this method operates in the spatial domain (as a convolution operation), the computation is time-consuming compared to computations in the frequency domain. In addition, the NCC method is easily dominated by large differences in the image brightness, which is a major issue with optical images only where different snow and dark rock conditions on glaciers during the acquisition of the two images might be present.

CCF-O computes cross-correlation in the frequency domain. One major advantage of CCF-O is that it is illumination invariant, i.e. the correlation is not affected by uniform areas. This is a desired property in glaciological research because uniform areas are common. For the same reason the method is also capable to match striped Landsat images after the failure of the scan line corrector (SLC-off) which traditional image matching techniques (i.e. NCC) are not capable of. The main disadvantage of CCF-O is in regions of large velocity gradients (i.e. ice deformation) and especially narrow glacier tongues in which the algorithm may often match valley sides rather than the glacier or the method returns a mismatch (Heid and Käab, 2012).

Results from the round robin for SAR data demonstrated that the cross-correlation of chips in amplitude SAR images performs better compared to the other SAR methods (fringe-visibility, InSAR and Multiple Aperture InSAR), in particular regarding its wider application to different glaciers and SAR data. In terms of algorithm efficiency, pre- and post-processing are very efficient procedures with processing durations of a few minutes, but main processing might be quite computationally intense (e.g. between one hour to a few days for a whole SAR scene depending on window size, pixels spacing and oversampling factor).

6.4 Processing line for optical data

6.4.1. Pre-processing

6.4.1.1 Geometric pre-processing

The most crucial pre-processing step before offset-tracking is the accurate co-registration of the data to be matched. Offsets over stable ground measured using the same algorithms as evaluated below (though often with different parameterizations) form the base of co-registration. The search (slave) image(s) can be either transformed to the geometry of the reference (master) image or (e.g. polynomial) transformation parameters can be computed and applied to the matching results without transforming the images. Co-registration transformation has the advantage to make offset-tracking and other usages of the images (e.g. time-series analysis) easier, but increases the computational time and storage and may introduce loss of information.

A polynomial transformation from a working image with coordinates (u,v) to the reference image (x,y) is given by:

$$\begin{aligned} u &= \sum_{l=0}^m \sum_{j=0}^i a_{lj} x^l y^{j-1} \\ v &= \sum_{l=0}^m \sum_{j=0}^i b_{lj} x^l y^{j-1} \end{aligned} \quad (6.17)$$

Where a and b are the polynomial parameters, and m and i the order of the polynomial used, in image registration typically up to 5th order. Note that (polynomial, and other) higher-order coregistration is not fully the appropriate model when tracking offsets in orthorectified images (see 6.2.2), but only when images in sensor geometry or in ellipsoid projected format are used. For orthoimages, a lower-order polynomial co-registration is used (lateral shift, rotation of significant), as orthoimages contain propagated DEM errors that vary locally and un-systematic.

6.4.1.2 Radiometric pre-processing

A number of radiometric pre-processing steps in offset-tracking have been proposed such as:

- i. Normalizations of the images (Heid and Käab, 2012a);
- ii. Tracking based on derivatives of the image data rather than the raw data (e.g. filtered versions, gradient images) (Heid and Käab, 2012a);
- iii. Interest operators to select suitable tracking targets (Förstner, 2000; Debella-Gilo and Käab, 2012);
- iv. Selection of most suitable band or radar frequency, if available, or derivatives of multiple bands (e.g. principle components).

Some of these pre-processing possibilities can only be applied to very specific input data (iv) and do not meet the evaluation criteria described in section 6.3. Other potential pre-processing procedures (i, ii) are actually built-in in some tracking algorithms. Further procedures (ii, iii) depend much on the data resolution and noise level, and thus also do not meet the evaluation criteria. As a consequence only radiometric pre-processing procedures that are largely independent of input data are considered. Since their applicability depends much on the tracking algorithm, they are considered together with these algorithms in the next section.

6.4.2 Selected algorithms for glacier velocity

The tables below summarize the main characteristics of the two selected algorithms NCC (Table 6.1) and CCF-O (Table 6.2).

<i>Abbreviation</i>	NCC
<i>Algorithm</i>	Normalized cross-correlation in spatial domain
	$CC(i, j) = \frac{\sum_{k,l} (s(i+k, j+l) - \mu_s)(r(k, l) - \mu_r)}{\sqrt{\sum_{k,l} (s(i+k, j+l) - \mu_s)^2 \sum_{k,l} (r(k, l) - \mu_r)^2}} \quad (6.18)$
	where (i,j) indicates the position in the search area, (k,l) the position in the reference area, r the pixel value of the reference chip, s the pixel value of the search chip, μ_r the average pixel value of the reference chip and μ_s the average pixel value of the search chip.
<i>Reference Applications</i>	Kääb and Vollmer (2002), Heid and Kääb (2012a)
<i>Description</i>	Kääb (2005)
	NCC is a matching method that is often used when studying glacier velocities. This is mostly due to its simplicity and robustness. The first image is taken as the reference image, and a template out of this image is searched for in the second image, or the search image. The peak of the cross-correlation surface indicates the displacement between the images. This cross-correlation is normalized.
<i>Advantages</i>	<ul style="list-style-type: none"> - The algorithm is simple and robust. - The algorithm can be applied to optical and SAR data. - Effects of normalization: Firstly, images with different illumination conditions can be better compared, and secondly, the correlation coefficient from different correlation attempts can be compared.
<i>Disadvantages</i>	<ul style="list-style-type: none"> - Original precision is only on the pixel-level. - Because this method operates in the spatial domain (as a convolution operation), the computation is time-consuming compared to computations in the frequency domain. - The NCC method is easily dominated by large differences in the digital numbers. If large differences exist within the reference or the search template, large differences also have to exist in the opposite window (i.e. the search or the reference template, respectively). We hypothesize that this is a major drawback with this method for glacier applications using optical data. Glacier areas usually contain large differences in digital numbers, because white snow and black rocks etc. are present. This would not be a problem if these differences were present in both images and also represented the displacement. However, it is common that snow patches in one image disappears in the next image, or that rocks move independently of the glacier movement by rolling or sliding at the glacier surface. Situations where large intensity differences are not present in both images or where large intensity differences do not represent the displacement are hence hypothesized to create erroneous matches for the NCC method.

- Improvements*
- The original pixel-level precision of NCC can be improved by interpolation of the correlation peak or image template interpolation beforehand correlation (Debella-Gilo and Käab, 2012). In glaciers_cci, image intensity interpolation of the matching templates will be used.
 - Entire scenes or scene sections will be matched, but a glacier mask will be added as data layer indicating which matches are on a glacier or not, according to the glacier outlines available.
 - The algorithm will contain an image-pyramid of 2-3 levels in which a coarse (but potentially more robust) initial measurement is followed by one or two more precise local refinements.

Table 6.1: Summary of the NCC algorithm for the glacier velocity product.

<i>Abbreviation</i>	CCF-O
<i>Algorithm</i>	Cross-correlation on gradient images in frequency domain $f_o(x, y) = \text{sgn}\left(\frac{\partial f(x, y)}{\partial x} + i\frac{\partial f(x, y)}{\partial y}\right)$ $g_o(x, y) = \text{sgn}\left(\frac{\partial g(x, y)}{\partial x} + i\frac{\partial g(x, y)}{\partial y}\right)$ $\text{where } \text{sgn}(x) = \begin{cases} 0 & \text{if } x = 0 \\ \frac{x}{ x } & \text{otherwise} \end{cases} \quad (6.19)$
<i>Reference</i>	Fitch et al. (2002)
<i>Applications</i>	Heid and Käab (2011)
<i>Description</i>	CCF-O computes first image intensity gradients in both dimensions, x and y. The new gradient images, called orientation images, are complex and hence consist of one real and one imaginary part, where the intensity differences in the x-direction represent the real matrix and the intensity differences in the y-direction represent the imaginary matrix. These orientation images are then matched using cross-correlation operated in the frequency domain.
<i>Advantages</i>	- Orientation correlation is illumination invariant. Because the orientation vector (and hence both orientation images) has zero value in uniform areas and a length of one in non-uniform areas, the correlation is not affected by uniform areas. This is a desired property in glaciological research because uniform areas are common. We also hypothesize this to be important when it comes to matching striped Landsat images after the failure of the scan line corrector (SLC-off) because the stripes are ignored when using orientation correlation.
<i>Disadvantages</i>	Not known (besides general image matching problems).
<i>Improvements</i>	Not yet known.

Table 6.2: Summary of the CCF-O algorithm for the glacier velocity product.

6.4.3 Post-processing

None of the algorithms above directly provides consistently accurate and reliable results. Errors and outliers cannot be avoided because of non-perfect image and ground conditions and have to be detected and filtered as much as possible.

Most of the above tracking algorithms provide, together with the offset with highest score, the correlation coefficient (CC) or signal-to-noise ratio (SNR) of the resulting offset. This measure can directly be used to estimate the potential quality of a match, and filters based on CC or SNR thresholds. Since CC and SNR, however, depend not only on the quality of a match but also on the image texture, such filters are not strictly conclusive and should be used with care and only in combination with other post-processing measures. The glaciers_cci product on optical glacier velocity will contain a layer of CC or SNR values that allows the user to set the according thresholds on the complete raw data.

The resulting displacement field will be low-pass filtered (e.g. mean, median, Gaussian, etc.) in order to filter out individual outliers. Similar to a resolution pyramid, the raw displacements can be compared to a low-pass filtered version of the field and measurements marked as outliers when the difference exceeds a given threshold on displacement magnitude and direction. This procedure is very successful over dense fields, but may fail where successful matches are only scattered, or where entire groups of displacements have a similar bias. The Glaciers_cci product on optical glacier velocity will contain a layer of values that indicate the difference between the raw and low-pass filtered version, which allows the user to set the thresholds for measurement acceptance by themselves.

It should be noted that in our opinion glaciologically sound and useful glacier displacements can only be obtained when the automatic results undergo a final expert check and, potentially, editing (similar to the well acknowledged and good practice in multispectral glacier mapping). Thus, the aim of displacement filters is to support the analyst in removing the obvious errors as much as possible to focus on details that require glaciological expert judgment. Some examples of the algorithm results and the filtering techniques discussed above are presented in Figs. 6.6 to 6.8 for the test site Karakoram.

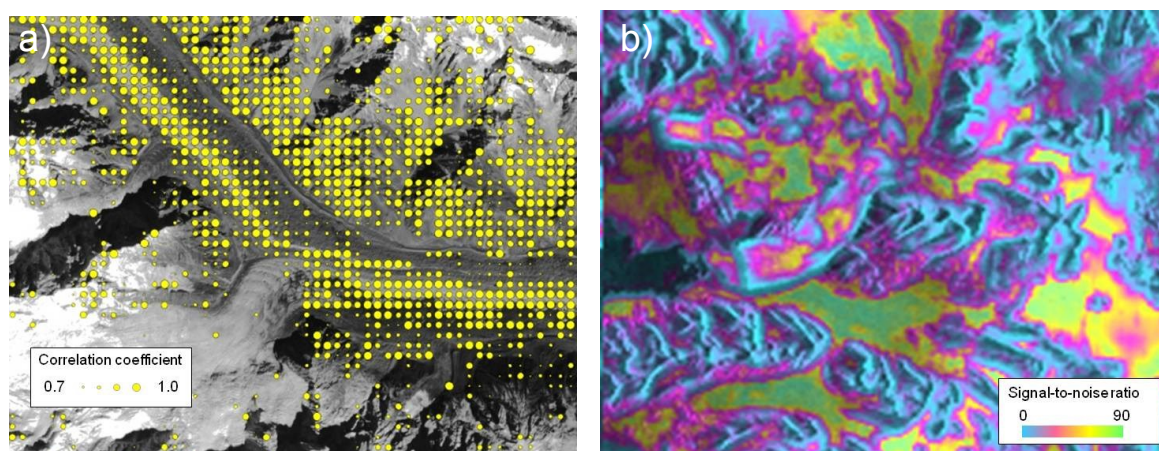


Fig 6.6: a) Cross-correlation coefficients for a 2000-2001 Landsat ETM+ image pair over Batura glacier, Karakoram. Small circles 0.7, maximum circles 1.0, correlation coefficients < 0.7 are removed (image width: 15 km). b) Signal-to-noise ratio (SNR) of offset-tracking between two ERS SAR images of 5 Apr and 10 May 1996 over Kronebreen, Svalbard. SNR values increase from blue over red to yellow and green (image width: 45 km). North is at top.

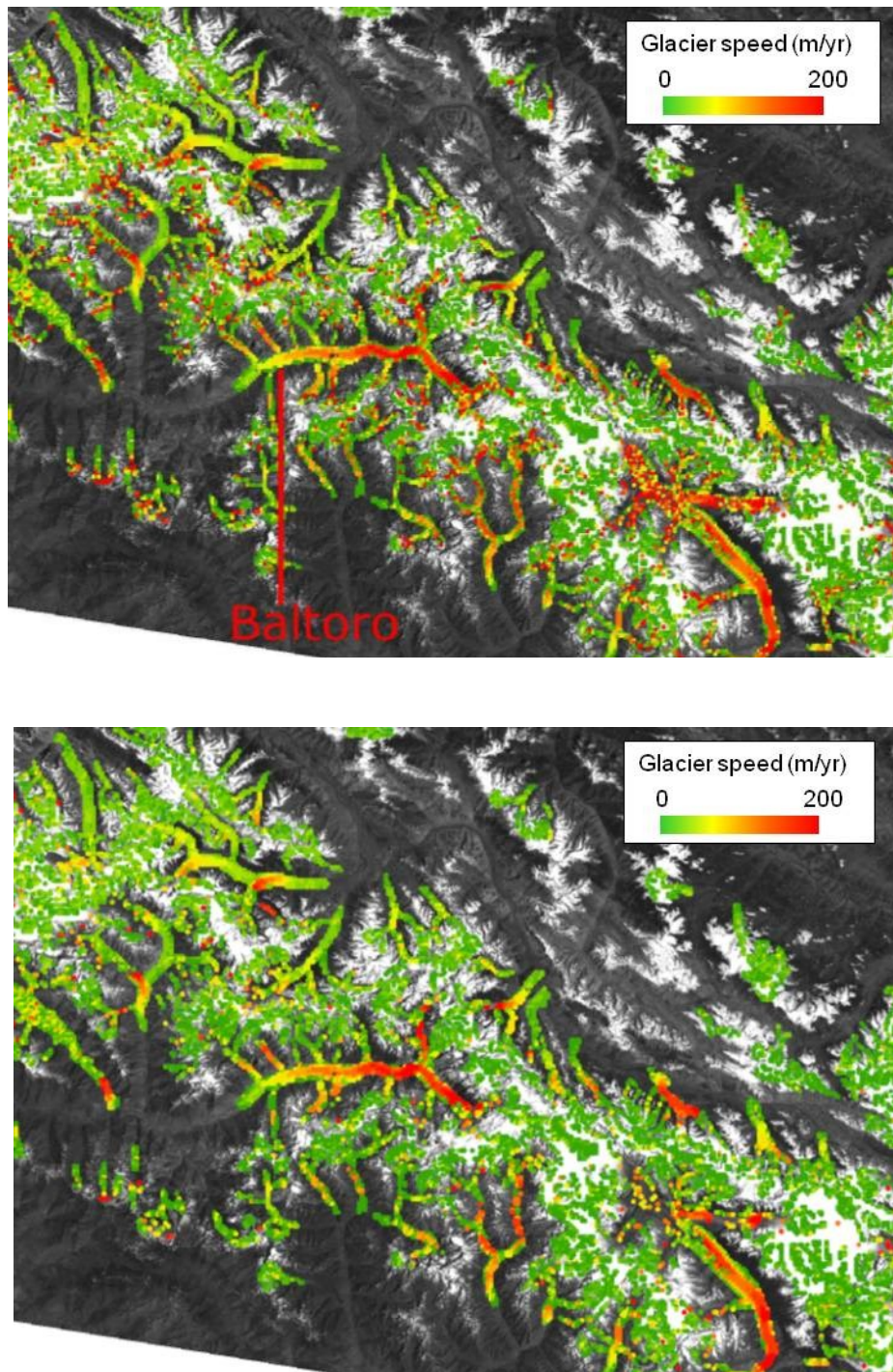


Fig. 6.7: Upper panel: Raw glacier speeds 2000-2001 as derived from a Landsat ETM+ image pair using CCF-O. Lower panel: Glacier speeds from the upper panel automatically filtered using a threshold on differences between the raw measurements and a low-pass filtered version of them. Maximum speed (red) is up to 200 m / year. Image width: 170 km, North is at top.

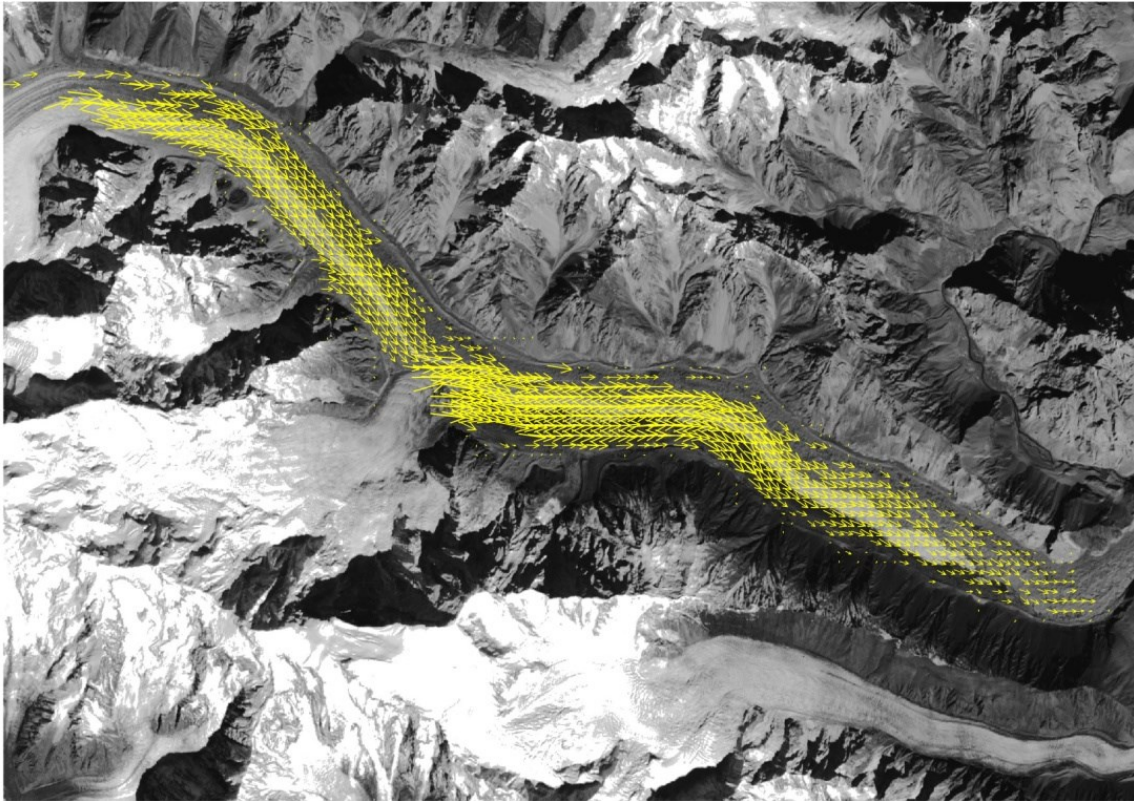


Fig. 6.8: Typical output of optical image matching after outlier filtering, displayed as vectors of velocity magnitude and direction (Batura glacier, Karakorum). North to the top. Image width: 30 km. Maximum speeds up to 140 m/yr.

6.5 Processing line for microwave data (SAR)

In addition to the core NCC algorithm as the main processing module (see description in 6.4.2), the flow diagram of SAR offset-tracking (Fig. 6.9) visualizes important pre- and post-processing issues for SAR data.

6.5.1 Pre-processing

In the pre-processing step data import and quality check (e.g. missing line detection) are first performed. The most crucial pre-processing step is then the accurate co-registration of the data to be matched. Offsets measured using the same NCC algorithms as the main processing (though often with different parametrizations, e.g. with much more limited number of sampling to reduce the computational borders) or using another algorithm (e.g. based on orbital data only or on fringe visibility) form the base of co-registration. A glacier outline mask can be optionally employed to limit the search over stable ground. A DEM can be optionally considered in the co-registration step in order to compensate for the stereo offsets relevant for the range offset field. The search (slave) image can be then either transformed to the geometry of the reference (master) image or (e.g. polynomial) transformation parameters can be computed and applied to the matching results without transforming the images. Co-registration transformation has the advantage to make offset-tracking and other usages of the images (e.g. time-series analysis of SAR data) easier, but increases the computational time and storage and may introduce loss of information, even if this is marginal for SAR data. A polynomial transformation from a working image with coordinates (u,v) to the reference image (x,y) is given by Equation (6.17).

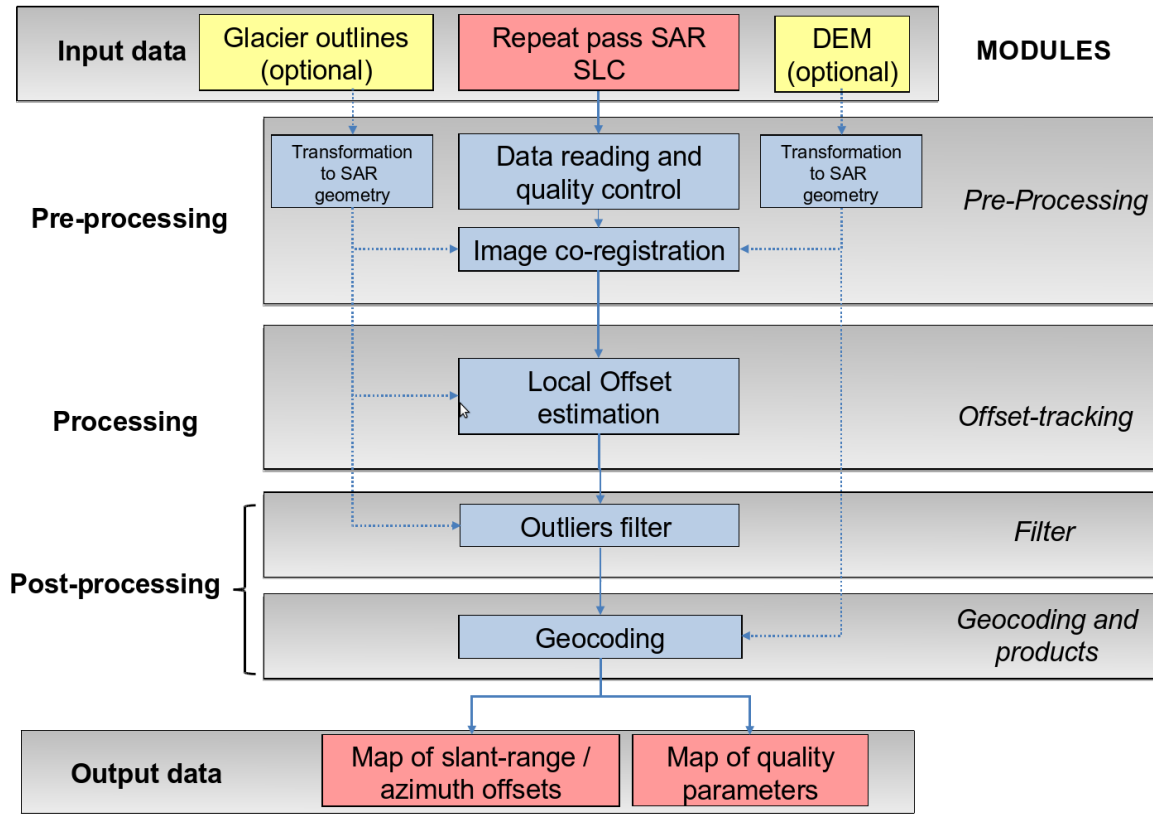


Fig. 6.9: Flow diagram outlining the principal processing steps of SAR offset tracking, including a first tentative indication of processing modules.

6.5.2 Main processing (Offset-tracking)

Once co-registered repeat-pass SAR images are available, NCC is employed to estimate offset-fields in slant-range and azimuth directions. In its mathematical framework the normalized cross-correlation in spatial domain is given in Equation (6.18). Offsets are measured using patches that are $M1 \times M2$ (range \times azimuth) pixels at a set of positions in the scene. The locations may be uniformly distributed over the image frame but for deformation mapping a specific region (i.e. glaciers) can be also selected for dense sampling. After global co-registration, the residual offsets should not be larger than a small fraction of the patch size that will be used for measuring the offset field. Typical values for $M1$ and $M2$ are in the range of 16 to 256 depending on the noise level, sensor resolution and specific application.

Data covering the patch is extracted from each SLC (single look complex) and the patch SLC data might be over-sampled by a factor of 2 or 4 using FFT interpolation to substantially improve the accuracy (Werner et al., 2005). The location of the maximum of the 2D correlation function yields the desired range and azimuth offsets. In order to obtain an accurate estimate of the correlation peak, the correlation function values over a $(m1 \times m2)$ region can be fitted using a bi-quadratic polynomial surface. The SNR of the offset measurement is obtained by taking the ratio of the peak value divided by the average correlation level outside the $(m1 \times m2)$ peak region. Typical values for $m1$ and $m2$ are in the order 3.

6.5.3 Post processing step 1: Filtering

Similarly to working with optical images, also SAR offset-tracking does not provide accurate and reliable results. Errors and outliers have therefore to be detected and filtered (see example in Fig. 6.10). Post-processing steps of SAR offset-tracking is similar to that of optical images, which was described in Section 6.4.3 and is thus not repeated here.

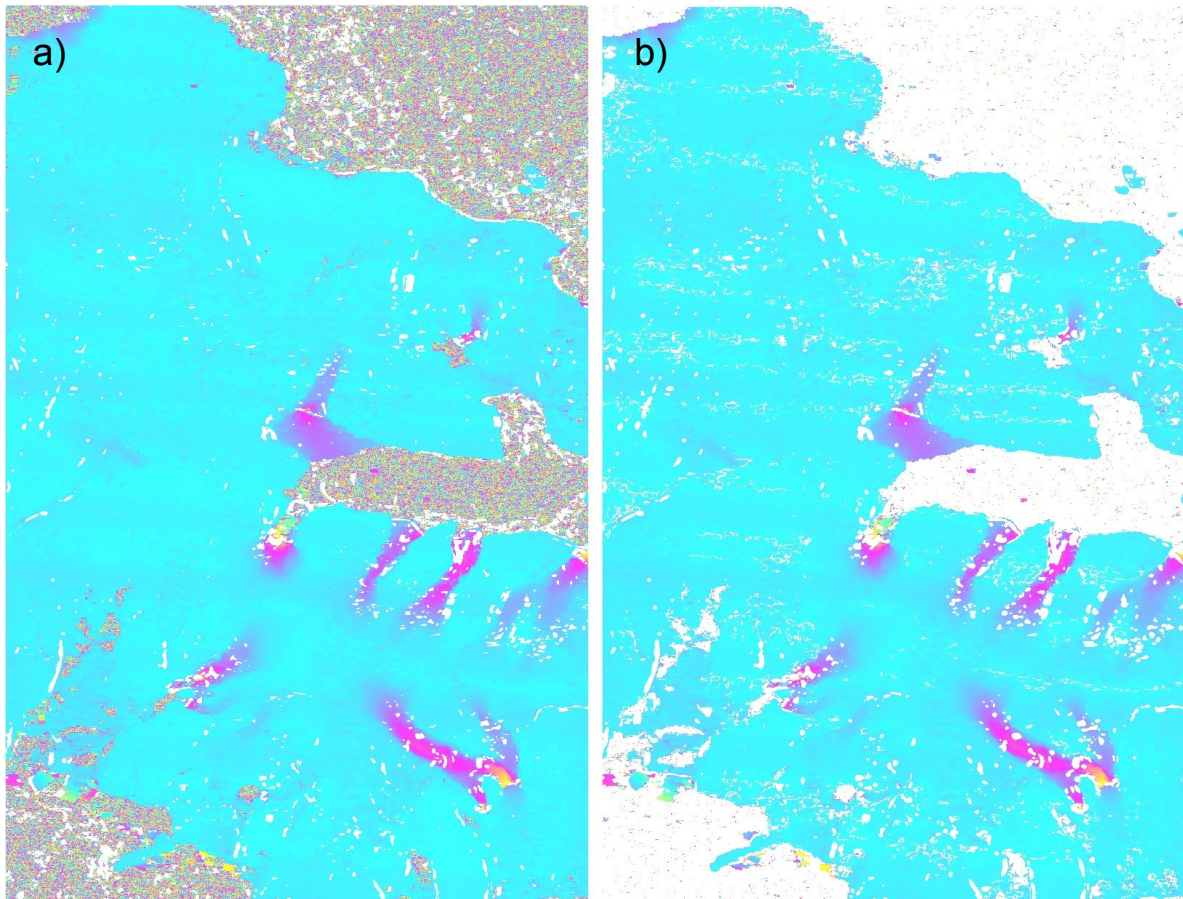


Fig. 6.10: Amplitude offset-tracking of an ALOS PALSAR pair from 1 February to 18 March 2008 over Vestfonna (Svalbard), (a) without outlier filtering and (b) with outlier filtering. Maximum speed (yellow/green) is up to 500 m/yr. The scene width is c. 70 km and the image is in the original radar geometry.

Geometric constraints such as maximum magnitude or direction sectors can be also used as filters. They are, however, not very useful for large-scale applications that include glaciers with different speeds and orientations. Also, for instance, gradients in glacier velocities could be used to filter, but they are very different from region to region due to the large variety of glaciers. Filtering the displacements based on the assumption that glaciers flow down-slope is considered to be impossible globally, because the required accurate elevation models are not available in all glacierized areas, and because of physical reasons where this assumption does not simply hold, such as in confluence areas or for supraglacial ice topography. It should be finally noted that in our opinion glaciologically sound and useful glacier displacements can only be obtained when the automatic results undergo an expert check and, potentially, editing (similar to the well acknowledged and good practice in multispectral glacier mapping). The

displacement filters should thus support the analyst in removing obvious errors as much as possible to focus on details that require glaciological expert judgement.

6.5.4 Post-processing step 2: Geocoding

Prior to delivery, the displacement fields are geocoded. Geocoding of SAR images is acknowledged as an automatic procedure that requires however special attention because of two typical characteristics of the SAR images: the range-doppler image geometry and the speckle. Geocoding of SAR images can be performed in a three steps procedure (Werner et al., 2002).

- In a first step, a parametric description of the orbit, the SAR imaging geometry, the map projection, and the local terrain height (which requires a DEM in a strict procedure but that can be also accomplished on an ellipsoidal height) are used to calculate an initial geocoding lookup table. The lookup table contains for each pixel of the map (i.e. the geocoded images in the desired map projection) the corresponding coordinate in the SAR range-Doppler geometry.
- Errors in the available orbit data, the SAR system parameters, and uncertainties in the map projection definition usually result in slight geocoding errors, which are corrected in a refinement step. As fine registration function a bi-linear function (range and azimuth offsets are linear functions of range and azimuth) is usually used.
- In the final step, the data files are resampled using the computed lookup table with advanced interpolation algorithms.

The refinement step is usually based on cross-correlation analysis between the SAR image to be geocoded and a SAR image simulated from a DEM. A SAR backscatter image is simulated from the local geometry and resampled into the SAR coordinates using inverse geocoding. Rather than having a small set of points, the simulated image can provide hundreds of features suitable for automated matching. The local offsets between the simulated and actual images are measured throughout the image. Then a least-square fit of the offsets is performed to obtain a polynomial transformation used to refine the lookup table. The values in the refined lookup table give the precise mapping between the SAR image and DEM. Modification of the lookup table values avoids having to resample the data a second time when generating a precise geocoded image. Considering that glaciers in high mountainous regions are exposed to large topographic relief and sometimes fast elevation changes (e.g. from ice melt), the quality, resolution and release date of the DEM nominally affects the final accuracy of the geocoding.

6.6 Input data and algorithm output

The focus of the round robin was on the selection of algorithms for highly automated and robust global-scale applications based on various sensors. Hence, the datasets for product generation must be globally available, provide regular acquisitions, and have no or uncomplicated access restrictions. Consequently, all current and future planned satellite SAR data as well as data from several optical sensors can be considered for production of glacier displacements:

- ERS-1/2 SAR, Envisat ASAR, Radarsat-1/2, Sentinel-1 (planned) at C-band;
- JERS-1 SAR, ALOS PALSAR and ALOS-2 (planned) at L-band;
- TerraSAR-X, Tandem-X and CosmoSkymed at X-band;

- Landsat (15-30 m), ASTER (15 m), Sentinel-2 (planned), Landsat 8 (after 1 June 2013);

While Landsat data are already orthorectified (L1T product); ASTER data can be ordered with and without orthorectification, with the former being used in Glaciers_cci. The data have different co-registration accuracies in the subpixel level, i.e. pixel geolocation accuracies that can be estimated by stable ground matches, and have to be added to the error budget.

Data from the following sensors have in general to be orthorectified and are considered for product and algorithm validation only, due to low spatial and temporal availability, limited coverage, usage restrictions, etc.:

- Optical: ALOS AVNIR and PRISM (have to be orthorectified), SPOT (orthorectified), commercial high-resolution sensors (have to be orthorectified), Google Maps screenshots;
- SAR: TerraSAR-X, Radarsat high-resolution, Cosmo-Skymed.

In response to the URD (Glaciers_cci, 2011) and the surveys conducted in the requirement definition process, the algorithm outputs are raw displacements in the slant range and azimuth direction (or x and y for optical) in UTM or geographic projection, i.e. without projection to a certain flow direction, and a map of quality parameters (e.g. SNR or score). As detailed in the PSD (Glaciers_cci, 2011), the data files are either in csv format or as a raster product (GeoTiff). As the data file consists of points with a user ID and coordinates, it can also be converted to a (point) shape file with the attribute information as for the raster product.

The standard output will contain the following information (see PSD, Glaciers_cci, 2011b)

- Header with metadata (coordinate system information, images used, processing dates and types, etc.)
- A group of results from NCC
- A group of results from CCF-O

The NCC and CCF-O result groups will contain:

- Two dimensional raw displacements
- CC and SNR for NCC, SNR for CCF-O
- Difference between raw displacements and low-pass filtered ones
- Glacier mask, indicating if the displacements are on glacier or outside (roughly, as the glacier mask will not always fully coincide with the image dates used for offset tracking)

6.7 Error budget estimates

The algorithm evaluation showed that most algorithms and implementations are in principle able to achieve precisions far into the sub-pixel range. That makes clear that the actual error budget is in practice and in most cases not dominated by the algorithm itself. The error budget of glacier displacement measurements from optical and SAR data consists of:

- the algorithm precision (subpixel, down to 1/5th to 1/10th of a pixel);
- image co-registration, including stereo offsets in the slant-range direction resulting from the different satellite orbit configurations of the two SAR images (to be checked over stable terrain where the accuracy close to matching precision possible);

- azimuth positional shifts caused by ionospheric phase delay variations (“azimuth streaking” with stronger effects at lower frequencies);
- surface changes and transformations (i.e. representativeness of surface features for ice particle displacement; e.g. shift of surface feature at sub-pixel or pixel level);
- geometric sensor noise (theoretical image-to-image registration error; sub-pixel level, but often larger than algorithm precision);
- mismatches due to similar but not corresponding features (e.g. self-similar ogives, crevasses or seracs; errors of many pixels possible);
- ability of post-processing procedures to eliminate measurement noise and mismatches;
- geocoding accuracy (e.g. influence from the DEM used for orthorectification).

6.8 Expected accuracy

The accuracy of individual glacier displacement measurements from repeat satellite data using optical offset-tracking is in the order of one pixel, with areas with better accuracy, but also areas and points of much lower accuracy. We estimate the reliability of the NCC algorithm to return co-registration parameters in a typical application over glacierized regions as accurate as 1/10th of a SAR image pixel. This corresponds for the ALOS PALSAR and TerraSAR-X data separated by a temporal interval (t_i) of 46 and 11 days, respectively, to an accuracy of about 6 to 10 m/yr and for the ENVISAT ASAR data with $t_i = 35$ days to an accuracy of about 15 m/yr (based on pixel sizes in ground range and azimuth direction of 7×3 , 2×2 and 14×4 m, respectively, and using the equation (for ASAR) $\text{accuracy} = \sqrt{1.4^2 \cdot 0.4^2} * [365/t_i]$). Reliability of the results is reduced due to frequent outliers that require special attention for optical and SAR data.

6.9 Practical considerations for implementation

The purpose of the algorithms is to allow for a high degree of automation over large regions. In offset tracking, operator intervention can be useful, but is not necessary, for

- accepting the stable ground co-registration,
- setting the matching template sizes and search window sizes (maximum displacement expected), and
- choosing a matching algorithm.

For a final processing scheme two complementary algorithms will be used. It is open to discussion if matching template sizes will be set by an operator, or if a set of default parameters will be used depending on the sensor type and the region of the scene (i.e. glacier type). It is also open to discussion, if a first-order filter will be applied to the result groups, providing an additional layer containing a quality flag based on CC, SNR and low-pass filtered displacements, or if even measurements assumed to be erroneous from the filter will be removed completely.

References

- Abermann, J., Fischer, A., Lambrecht, A. and Geist, T. (2010): On the potential of very high-resolution repeat DEMs in glacial and periglacial environments. *The Cryosphere*, 4, 53-65.
- Abshire, J.B., Sun, X.L., Riris, H., Sirota, J.M., McGarry, J.F., Palm, S., Yi, D.H. and Liiva, P. (2005): Geoscience Laser Altimeter System (GLAS) on the ICESat mission: On-orbit measurement performance, *Geophysical Research Letters*, 32, L21S02, 1-4.
- Albert, T.H. (2002): Evaluation of remote sensing techniques for ice-area classification applied to the tropical Quelccaya Ice Cap, Peru. *Polar Geography*, 26 (3), 210-226.
- Andreassen, L.M. (1999): Comparing traditional mass balance measurements with long-term volume change extracted from topographical maps: a case study of Storbreen glacier in Jotunheimen, Norway, for the period 1940–1997. *Geografiska Annaler*, 81A (4), 467-476.
- Andreassen, L.M., Paul, F., Kääb, A. and Hausberg, J.E. (2008): Landsat-derived glacier inventory for Jotunheimen, Norway, and deduced glacier changes since the 1930s. *The Cryosphere*, 2, 131-145.
- Aniya, M., Sato, H., Naruse, R., Skvarca, P. and Casassa, G. (1996): The use of satellite and airborne imagery to inventory outlet glaciers of the Southern Patagonia Icefield, South America. *Photogrammetric Engineering and Remote Sensing*, 62, 1361-1369.
- Atwood, D., Meyer, F. and Arendt, A. (2010): Using L-band SAR coherence to delineate glacier extent. *Canadian Journal of Remote Sensing*, 36, S186-S195.
- Bayr, K. J., Hall, D.K. and Kovalick, W.M. (1994): Observations on glaciers in the eastern Austrian Alps using satellite data. *International Journal of Remote Sensing*, 15, 1733-1742.
- Berthier, E., Arnaud, Y., Vincent, C. and Rémy, F. (2006): Biases of SRTM in high-mountain areas: Implications for the monitoring of glacier volume changes. *Geophys. Res. Lett.*, 33, L08502.
- Berthier, E., Arnaud, Y., Kumar, R., Ahmad, S., Wagnon, P. and Chevallier, P. (2007): Remote sensing estimates of glacier mass balances in the Himachal Pradesh (Western Himalaya, India). *Remote Sensing of Environment*, 108, 327-338.
- Berthier, E. and Toutin, T. (2008): SPOT5-HRS digital elevation models and the monitoring of glacier elevation changes in North-West Canada and South-East Alaska. *Remote Sensing of Environment*, 112, 2443-2454.
- Berthier, E., Schiefer E., Clarke, G.K.C., Menounos, B. and Rémy, F. (2010): Contribution of Alaskan glaciers to sea-level rise derived from satellite imagery. *Nature Geoscience*, 3 (2), 92-95.
- Binaghi, E., Madella, P., Montesano, M.P. and Rampini, A. (1997): Fuzzy contextual classification of multisource remote sensing images. *IEEE Transactions on Geoscience and Remote Sensing*, GE-35 (2), 326-339.
- Bishop, M.P., Barry, R.G., Bush, A.B.G., Copeland, L., Dwyer, J.L., Fountain, A.G., Haeberli, W., Hall, D.K., Kääb, A., Kargel, J.S., Molnia, B.F., Olsenholler, J.A., Paul, F., Raup, B.H., Shroder, J.F., Trabant, D.C., Wessels, R. (2004): Global Land Ice Measurements from Space (GLIMS): Remote sensing and GIS investigations of the Earth's cryosphere. *Geocarto International*, 19 (2), 57-85.
- Bouillon, A., Bernard, M., Gigord, P., Orsoni, A., Rudowski, V. and Baudoin, A. (2006): SPOT 5 HRS geometric performances: Using block adjustment as a key issue to improve

- quality of DEM generation. *ISPRS Journal of Photogrammetry and Remote Sensing*, 60, 134-146.
- Brown G. S. (1977): The average impulse response of a rough surface and its applications. *IEEE Transactions on Antennas Propagation*, AP-25, 67-74.
- Chavez, P. (1988): An improved dark-object subtraction technique for atmospheric scattering correction of multispectral data. *Remote Sensing of Environment*, 24, 459-479.
- Cox, L.H. and March, R.S. (2004): Comparison of geodetic and glaciological mass-balance techniques, Gulkana Glacier, Alaska, USA. *Journal of Glaciology*, 50 (170), 363-370.
- Davis, C. H. (1996): Comparison of Ice-Sheet Satellite Altimeter Retracking Algorithms. *IEEE Transactions on Geoscience and Remote Sensing*, 34, (1), 229-236.
- Debella-Gilo, M. and Käab, A. (2012): Locally adaptive template sizes in matching repeat images of Earth surface mass movements. *ISPRS Journal of Photogrammetry and Remote Sensing*, 69, 10-28.
- DMK/DPK (Deutscheschweizerische Mathematikkommision/Physikkommision) (1977): Formeln und Tafeln. *Mathematik - Statistik - Physik*. Zürich, Orell Füssli Verlag.
- Dozier, J. (1989): Spectral signature of alpine snow cover from Landsat 5 TM. *Remote Sensing of Environment*, 28, 9-22.
- Duda, D.P., Spinhirne, J.D. and Eloranta, E.W. (2001): Atmospheric multiple scattering effects on GLAS altimetry. I. Calculations of single pulse bias. *IEEE Transactions on Geoscience and Remote Sensing*, 39(1), 92 -101.
- Eloranta, E. W. (1998): A practical model for lidar multiple scattering. *Appl. Opt.*, 37, 2464-2472.
- Elsberg, D.H., W.D. Harrison, K.A. Echelmeyer and R.M. Krimmel (2001): Quantifying the effects of climate and surface change on glacier mass balance. *Journal of Glaciology*, 47 (159), 649-658.
- ESA Online News Bulletin (2007): Sentinel-3 The Ocean and Medium-Resolution Land Mission for GMES Operational Services, *ESA Bulletin* 131.
- Farr, T. G., Rosen, P. A., Caro, E., Crippen, R., Duren, R., Hensley, S., Kobrick, M., Paller, M., Rodriguez, E., Roth, L., Seal, D., Shaffer, S., Shimada, J., Umland, J., Werner, M., Oskin, M., Burbank, D. and Alsdorf, D. (2007): The Shuttle Radar Topography Mission. *Rev. Geophys.*, 45, RG2004.
- Fitch, A.J., Kadyrov, A., Christmas, W.J. and Kittler, J. (2002): Orientation correlation. *British Machine Vision Conference*, 133-142.
- Frey, H. Paul, F. and Strozzi, T. (2012): Compilation of a glacier inventory for the western Himalayas from satellite data: Methods, challenges and results. *Remote Sensing of Environment*, 124, 832-843.
- Fricker, H.A., Borsa, A., Minster, B., Carabajal, C., Quinn, K. and Bills, B. (2005): Assessment of ICESat performance at the Salar de Uyuni, Bolivia. *Geophysical Research Letters*, 32 (L21S06), 1-5.
- Fujisada, H., Bailey, G., Kelly, G., Hara, S. and Abrams, M. (2005): ASTER DEM performance. *IEEE Transactions on Geoscience and Remote Sensing*, 43, 2707-2714.
- Förstner, W. (1982): On the geometric precision of digital image correlation. *ISPRS Symposium Mathematical Models, Accuracy Aspects and Quality Control*, 176-189.
- Förstner, W. (2000): Image preprocessing for feature extraction in digital intensity, color and range images. In: A. Dermanis, A. Grün and F. Sansò (Eds.), *Geomatic Methods for the Analysis of Data in the Earth Sciences*. Lecture Notes in Earth Sciences. Springer. 165-189.

- Gardelle, J., Berthier, E. and Arnaud, Y. (2012): Impact of resolution and radar penetration on glacier elevation changes computed from DEM differencing. *Journal of Glaciology*, 58 (208), 419-422.
- Gardner, A.S., Moholdt, G., Wouters, B., Wolken, G., Burgess, D. Sharp, M., Cogley, J., Braun, C. and Labine, C. (2011): Sharply increased mass loss from glaciers and ice caps in the Canadian Arctic Archipelago. *Nature*, 473, 357-360.
- Geist, T., E. Lutz and J. Stötter. (2003): Airborne laser scanning technology and its potential for applications in glaciology. In *Proceedings of the ISPRS Workshop on 3-D Reconstruction from Airborne Laserscanner and INSAR Data*. Dresden, International Society for Photogrammetry and Remote Sensing, 101-106.
- Geist, T., Elvehøy, H., Jackson, M. and Stötter, J. (2005): Investigations on intra-annual elevation changes using multi-temporal airborne laser scanning data: case study Engabreen, Norway. *Annals of Glaciology*, 42, 195-201.
- Gjermundsen, E.F., Mathieu, R., Kääb, A., Chinn, T., Fitzharris, B. and Hagen, J.O. (2011): Assessment of multispectral glacier mapping methods and derivation of glacier area changes, 1978-2002, in the central Southern Alps, New Zealand, from ASTER satellite data, field survey and existing inventory data. *Journal of Glaciology*, 57 (204), 667-683.
- Glaciers_cci (2011a): User Requirements Document (URD): Prepared by the Glaciers_cci consortium, 45 pp.
- Glaciers_cci (2011b): Product Specifications Document (PSD): Prepared by the Glaciers_cci consortium, 43 pp.
- Glaciers_cci (2011c): Data Access Requirements Document (DARD): Prepared by the Glaciers_cci consortium, 46 pp.
- Glaciers_cci (2012a): Algorithm Theoretical Basis Document version 0 (ATBDv0): Prepared by the Glaciers_cci consortium, 95 pp.
- Glaciers_cci (2012b): Product Validation and Algorithm Selection Report (PVASR): Prepared by the Glaciers_cci consortium, 113 pp.
- Glaciers_cci (2013a): Algorithm Theoretical Basis Document version 0 (ATBDv1): Prepared by the Glaciers_cci consortium, 96 pp.
- Glaciers_cci (2013b): Input/Output Data Definition version 1 (IODDv1): Prepared by the Glaciers_cci consortium, 26 pp.
- Glaciers_cci (2013c): Detailed Processing Model version 1 (DPMv1): Prepared by the Glaciers_cci consortium, 86 pp.
- Glaciers_cci (2013d): Uncertainty Characterisation Report v1 (ATBDv1): Prepared by the Glaciers_cci consortium, 22 pp.
- Haeberli, W. (2006): Integrated perception of glacier changes: a challenge of historical dimensions. In: Knight, P.G. (ed.): *Glacier science and environmental change*. Oxford: Blackwell Publishing, 423-430.
- Hagen, J.O., Eiken, T., Kohler, J. and Melvold, K. (2005): Geometry changes on Svalbard glaciers: mass-balance or dynamic response? *Annals of Glaciology*, 42, 255-261.
- Hall, D.K., Chang, A.T.C. and Siddalingaiah, H. (1988): Reflectances of glaciers as calculated using Landsat 5 Thematic Mapper data. *Remote Sensing of Environment*, 25, 311-321.
- Hall, D.K., Williams, R.S., Barton, J.S. Sigurdsson, O. Smith, L.C. and Garvin, J.B. (2000): Evaluation of remote-sensing techniques to measure decadal-scale changes of Hofsjokull ice cap, Iceland. *Journal of Glaciology*, 46 (154), 375-388.
- Heid, T. and Kääb, A. (2012a): Evaluation of different image matching methods for deriving glacier surface displacements globally from optical satellite imagery. *Remote Sensing and Environment*, 118, 339-355.

- Heid, T. and Kääb, A. (2012b): Repeat optical satellite images reveal widespread and long term decrease in land-terminating glacier speeds. *The Cryosphere*, 6, 467-478.
- Hirano, A., Welch, R. and Lang, H. (2003): Mapping from ASTER stereo image data: DEM validation and accuracy assessment. *ISPRS Journal of Photogrammetry and Remote Sensing*, 57, 356-370.
- Howat, I.M., Smith, B.E., Joughin, I. and Scambos, T.A. (2008): Rates of southeast Greenland ice volume loss from combined ICESat and ASTER observations. *Geophysical Research Letters*, 35, L17505.
- Huss, M., Bauder, A. and Funk, M. (2009): Homogenization of long term mass-balance time series. *Annals of Glaciology*, 50 (50), 198-206.
- Huss, M. (2011): Present and future contribution of glaciers to runoff from macroscale drainage basins in Europe. *Water Resources Research*, 47, W07511.
- IGOS (2007): Integrated Global Observing Strategy Cryosphere theme report - For the monitoring of our environment from space and from Earth. Geneva: World Meteorological Organization. WMO/TD-No. 1405, 100 pp.
- Iwasaki, A. and Fujisada, H. (2005): ASTER geometric performance, *Geoscience and Remote Sensing. IEEE Transactions on Geoscience and Remote Sensing*, 43, 2700-2706.
- Jacobs, J.D., Simms, E.L. and Simms, A. (1997): Recession of the southern part of Barnes Ice Cap, Baffin Island, Canada, between 1961 and 1993, determined from digital mapping of Landsat TM. *Journal of Glaciology*, 43 (143), 98-102.
- JPL (2011): ASTER spectral library Version 2.0. Online at: <http://speclib.jpl.nasa.gov/>
- Kaufmann, V. and Ladstädter, R. (2003): Quantitative analysis of rock glacier creep by means of digital photogrammetry using multi-temporal aerial photographs: two case studies in the Austrian Alps. Eighth International Conference on Permafrost. 1. Balkema. 525-530.
- Korona, J., Berthier, E., Bernard, M., Rémy, F. and Thouvenot, E. (2009): SPIRIT. SPOT 5 stereoscopic survey of Polar Ice: Reference Images and Topographies during the fourth International Polar Year (2007-2009): *ISPRS Journal of Photogrammetry and Remote Sensing*, 64, 204-212.
- Kääb, A. and Vollmer, M. (2000): Surface geometry, thickness changes and flow fields on creeping mountain permafrost: automatic extraction by digital image analysis. *Permafrost and Periglacial Processes*. 11(4), 315-326.
- Kääb, A., Paul, F., Maisch, M., Hoelzle, M. and Haeberli, W. (2002): The new remote-sensing-derived Swiss glacier inventory: II. First Results. *Annals of Glaciology*, 34, 362-366.
- Kääb, A., Huggel, C., Paul, F., Wessels, R., Raup, B., Kieffer, H. and Kargel, J. (2002): Glacier monitoring from ASTER imagery: Accuracy and Applications. *Proceedings of EARSeL-LISSIG Workshop Observing our Cryosphere from Space*, 2,43-53.
- Kääb, A., Huggel, C., Fischer, L., Guex, S., Paul, F., Roer, I., Salzmann, N., Schlaefli, S., Schmutz, K., Schneider, D., Strozzì, T. and Weidmann, W. (2005): Remote sensing of glacier- and permafrost-related hazards in high mountains: an overview. *Natural Hazards and Earth System Sciences*, 5, 527-554.
- Kääb, A. (2005): Remote Sensing of Mountain Glaciers and Permafrost Creep. *Schriftenreihe Physische Geographie. Glaziologie und Geomorphodynamik*. 48. University of Zurich, Zurich.
- Kääb, A. (2008): Glacier Volume Changes Using ASTER Satellite Stereo and ICESat GLAS Laser Altimetry, A Test Study on Edgeya, Eastern Svalbard, *IEEE Transactions on Geoscience and Remote Sensing*, 46, 2823-2830.

- Larsen, C.F., Motyka, R.J., Arendt, A.A., Echelmeyer, K.A. and Geissler, P.E. (2007): Glacier changes in southeast Alaska and northwest British Columbia and contribution to sea level rise. *Journal of Geophysical Research-Earth Surface*, 112, F01007.
- Le Bris, R., Paul, F., Frey, H. and Bolch, T. (2011): A new satellite-derived glacier inventory for western Alaska. *Annals of Glaciology*, 52 (59), 135-143.
- Leprince, S., Ayoub, F., Klingler, Y. and Avouac, J.P. (2007): Co-Registration of Optically Sensed Images and Correlation (COSI-Corr): an operational methodology for ground deformation measurements. *IGARSS: 2007 IEEE International Geoscience and Remote Sensing Symposium*, Vols 1-12, 1943-1946.
- Lillesand, T., Kiefer, R. and Chipman, J. (2004): *Remote Sensing and Image Interpretation*, 5 edition, John Wiley & Sons, Inc., Hoboken, NJ.
- Martin, T.V., Zwally, H.J., Brenner A.C. and Bindschadler R.A. (1983): Analysis and retracking of continental ice sheet radar altimetry wave-forms. *Journal of Geophysical Research*, 88, 1608-1616.
- Mavrocordatos C., Berruti B., Aguirre M. and Drinkwater M. (2007): The Sentinel-3 mission and its Topography element. *Proceeding of IEEE IGARSS 2007*, Barcelona, Spain.
- Moholdt, G., Hagen, J.O., Eiken, T. and Schuler, T.V. (2010a): Geometric changes and mass balance of the Austfonna ice cap, Svalbard. *The Cryosphere*, 4, 21-34.
- Moholdt, G., Nuth, C., Hagen, J.O. and Kohler, J. (2010b): Recent elevation changes of Svalbard glaciers derived from ICESat laser altimetry. *Remote Sensing of Environment*, 114 (11), 2756-2767.
- Mohr, J.J. and Madsen, S.N. (1996) Multi-pass interferometry for studies of glacier dynamics, *ESA Workshop Applicat. ERS SAR Interferometry: FRINGE'96*: Univ. Zurich.
- Müller, K. (2011): *Microwave penetration in polar snow and ice: Implications for GPR and SAR*, PhD Thesis: Department of Geosciences, University of Oslo.
- Nuth, C., Moholdt, G., Kohler, J., Hagen, J.O. and Kääb, A. (2010): Svalbard glacier elevation changes and contribution to sea level rise. *Journal of Geophysical Research*, 115 (F1), F01008.
- Nuth, C. and Kääb, A. (2011): Co-registration and bias corrections of satellite elevation data sets for quantifying glacier thickness change. *The Cryosphere*, 5, 271-290.
- Nuth C., Schuler T.V., Kohler J., Altena B. and Hagen J.O. (*in press*): Estimating the long term calving flux of Kronebreen, Svalbard, from geodetic elevation changes and mass balance modelling, *Journal of Glaciology*.
- Paul, F. (2001): Evaluation of different methods for glacier mapping using Landsat TM. *EARSeL Workshop on Remote Sensing of Land Ice and Snow*, Dresden, 16.-17.6.2000. *EARSeL eProceedings*, 1, 239-245.
- Paul, F. (2002): Changes in glacier area in Tyrol, Austria, between 1969 and 1992 derived from Landsat 5 TM and Austrian Glacier Inventory data. *International Journal of Remote Sensing*, 23 (4), 787-799.
- Paul, F. (2008): Calculation of glacier elevation changes with SRTM: is there an elevation-dependent bias? *Journal of Glaciology*, 54 (188), 945-946.
- Paul, F. (2010): Towards a global glacier inventory from satellite data. *Geographica Helvetica*, 65 (2), 103-112.
- Paul, F. and Kääb, A. (2005): Perspectives on the production of a glacier inventory from multispectral satellite data in the Canadian Arctic: Cumberland Peninsula, Baffin Island. *Annals of Glaciology*, 42, 59-66.
- Paul, F. and Haerberli, W. (2008): Spatial variability of glacier elevation changes in the Swiss Alps obtained from two digital elevation models, *Geophysical Research Letters*, 35, L21502.

- Paul, F. and Andreassen, L.M. (2009): A new glacier inventory for the Svartisen region, Norway, from Landsat ETM+ data: challenges and change assessment. *Journal of Glaciology*, 55 (192), 607-618.
- Paul, F. and Hendriks, J. (2010): Optical remote sensing of glaciers. In: Pellikka, P. and Rees, W.G (Eds.), *Remote Sensing of Glaciers - Techniques for Topographic, Spatial and Thematic Mapping of Glaciers*. CRC Press, Taylor and Francis Group, Leiden, 137-152.
- Paul, F., Kääb, A., Maisch, M., Kellenberger, T. and Haerberli, W. (2002): The new remote-sensing-derived Swiss glacier inventory: I. Methods. *Annals of Glaciology*, 34, 355-361.
- Paul, F., Huggel, C., Kääb, A. and Kellenberger, T. (2003): Comparison of TM-derived glacier areas with higher resolution data sets. *EARSeL Workshop on Remote Sensing of Land Ice and Snow, Bern, 11.-13.3.2002*. EARSeL eProceedings, 2, 15-21.
- Paul, F., Huggel, C. and Kääb, A. (2004): Combining satellite multispectral image data and a digital elevation model for mapping of debris-covered glaciers. *Remote Sensing of Environment*, 89 (4), 510-518.
- Paul, F., Barry, R., Cogley, G., Frey, H., Haerberli, W., Ohmura, A., Ommanney, S., Raup, B., Rivera, A., Zemp, M. (2009): Recommendations for the compilation of glacier inventory data from digital sources. *Annals of Glaciology*, 50 (53), 119-126.
- Paul, F. and Hendriks, J. (2010): Optical remote sensing of glaciers. In: Pellikka, P. and Rees, W.G (Eds.), *Remote Sensing of Glaciers - Techniques for Topographic, Spatial and Thematic Mapping of Glaciers*. CRC Press, Taylor and Francis Group, Leiden, 137-152.
- Paul, F., Andreassen, L.M. and Winsvold, S.H. (2011): A new glacier inventory for the Jostedalbreen region, Norway, from Landsat TM scenes of 2006 and changes since 1966. *Annals of Glaciology*, 52 (59), 144-153
- Paul, F., Frey, H. and Le Bris, R. (2011): A new glacier inventory for the European Alps from Landsat TM scenes of 2003: Challenges and results. *Annals of Glaciology*, 52 (59), 144-152.
- Pritchard, H., Murray, T., Luckman, A., Strozzi, T and Barr, S. (2005): Glacier surge dynamics of Sortebræ, east Greenland, from synthetic aperture radar feature tracking. *Journal of Geophysical Research*, 110, F03005.
- Pritchard, H.D., Arthern, R.J., Vaughan, D.G. and Edwards, L.A. (2009): Extensive dynamic thinning on the margins of the Greenland and Antarctic ice sheets. *Nature*, 461, 971-975.
- Quincey, D.J. and Glasser, N.F. (2009): Morphological and ice-dynamical changes on the Tasman Glacier, New Zealand, 1990-2007. *Global and Planetary Change*, 68(3), 185-197.
- Qunzhu, Z., Meisheng, C., Xuezhi, F., Fengxian, L., Xianzhang, C. and Wenkuna, S. (1983): A study of spectral reflection characteristics for snow, ice and water in the north of China. *IAHS*, 145, 451-462.
- Rabus, B., Eineder, M., Roth, A. and Bamler, R. (2003): The shuttle radar topography mission - a new class of digital elevation models acquired by spaceborne radar. *ISPRS Journal of Photogrammetry and Remote Sensing*, 57, 241-262.
- Racoviteanu, A.E., Williams, M.W. and Barry, R.G. (2008): Optical remote sensing of glacier characteristics: a review with focus on the Himalaya. *Sensors*, 8, 3355-3383.
- Racoviteanu, A.E., Paul, F., Raup, B., Khalsa, S.J.S. and Armstrong, R. (2009): Challenges in glacier mapping from space: recommendations from the Global Land Ice Measurements from Space (GLIMS) initiative. *Annals of Glaciology*, 50 (53), 53-69.
- Rignot, E., Echelmeyer, K. and Krabill, W. (2001): Penetration depth of interferometric synthetic-aperture radar signals in snow and ice, *Geophysical Research Letters*, 28, 3501-3504.
- Rignot, E., Rivera, A. and Casassa, G. (2003): Contribution of the Patagonia Icefields of South America to sea level rise. *Science*, 302, 434-437.

- Rodriguez, E., Morris, C.S. and Belz, J.E. (2006): A global assessment of the SRTM performance. *Photogrammetric Engineering and Remote Sensing*, 72, 249-260.
- Rosen, P. A., Hensley, S., Joughin, I. R., Li, F. K., Madsen, S. N., Rodriguez, E. and Goldstein, R. M. (2000): Synthetic aperture radar interferometry - Invited paper, *Proceedings IEEE*, 88, 333-382.
- Rosmorduc, V., Benveniste, J., Bronner, E., Dinardo, S., Lauret, O., Maheu, C., Milagro, M. and Picot, N. (2011): Radar Altimeter Tutorial, J. Benveniste, N. Picot, Editors.
- Rott, H. and Markl, G. (1989): Improved snow and glacier monitoring by the Landsat Thematic Mapper. *Proceedings of a workshop on Landsat Thematic Mapper applications*, ESA, SP-1102, 3-12.
- Rott, H., Müller, F., Nagler, T. and Floricioiu, D. (2010): The imbalance of glaciers after disintegration of Larsen B ice shelf, Antarctic Peninsula. *The Cryosphere*. 4, 1607–1633, 2010.
- Sauber, J., Molnia, B., Carabajal, C., Luthcke, S. and Muskett, R. (2005): Ice elevations and surface change on the Malaspina Glacier, Alaska, *Geophysical Research Letters*, 32, L23S01.
- Scambos, T.A., Dutkiewicz, M.J., Wilson, J.C. and Bindschadler, R.A. (1992): Application of image cross-correlation to the measurement of glacier velocity using satellite image data. *Remote Sensing of Environment*, 42 (3), 177-186.
- Schenk, T. (1999): *Digital Photogrammetry*, 1, TerraScience, Laurelville, Ohio.
- Scherler, D., Leprince, S. and Strecker, M.R. (2008): Glacier-surface velocities in alpine terrain from optical satellite imagery - Accuracy improvement and quality assessment. *Remote Sensing of Environment*, 112 (10), 3806-3819.
- Schiefer, E., Menounos, B. and Wheate, R. (2007): Recent volume loss of British Columbian glaciers, Canada. *Geophysical Research Letters*, 34, L16503.
- Schutz, B.E., Zwally, H.J., Shuman, C.A., Hanock, D. and DiMarzio, J.P. (2005): Overview of the ICESat Mission. *Geophysical Research Letters*, 32, L21S01.
- Shepherd, A., Wingham, D., Ridout, A. and Muir, A. (2010): Initial Assessment of CryoSat-2 Performance over Continental Ice. *Proc. of American Geophysical Union, Fall Meeting 2010*.
- Shukla, A., M.K. Arora and R.P. Gupta (2011): Synergistic approach for mapping debris-covered glaciers using optical-thermal remote sensing data with inputs from geomorphometric parameters. *Remote Sensing of Environment*, 114 (7), 1378-1387.
- Sidjak, R.W. and Wheate, R.D. (1999): Glacier mapping of the Illecillewaet icefield, British Columbia, Canada, using Landsat TM and digital elevation data. *International Journal of Remote Sensing*, 20, 273-284.
- Skvarca, P., Raup, B. and De Angelis, H. (2003): Recent behaviour of Glaciar Upsala, a fast-flowing calving glacier in Lago Argentino, southern Patagonia. *Annals of Glaciology*. 36, 184-188.
- Slobbe, D.C., Lindenbergh, R.C. and Ditmar, P. (2008): Estimation of volume change rates of Greenland's ice sheet from ICESat data using overlapping footprints. *Remote Sensing of Environment*, 112, 4204-4213.
- Strozzi T., Murray, T., Wegmüller, U. and Werner, C. (2002): Glacier Motion Estimation Using SAR Offset-Tracking Procedures. *IEEE Transactions on Geoscience and Remote Sensing*, 40 (11), 2384-2391.
- Strozzi, T., Paul, F. and Käab, A. (2010): Glacier mapping with ALOS PALSAR data within the ESA GlobGlacier project. *Proceedings of the ESA Living Planet Symposium*, 28 June - 2 July 2010, Bergen, Norway, ESA SP-686.

- Stuefer, M. (1999) Investigations on mass balance and dynamics of Moreno Glacier based on field measurements and satellite imagery. PhD Thesis, Univ. of Innsbruck, Austria.
- Thibert, E., Blanc, R., Vincent, C. and Eckert, N. (2008): Glaciological and volumetric mass-balance measurements: error analysis over 51 years for Glacier de Sarennes, French Alps. *Journal of Glaciology*, 54 (186), 522-532.
- Toutin, T. (2002): Three-dimensional topographic mapping with ASTER stereo data in rugged topography. *IEEE Transactions on Geoscience of Remote Sensing*, 40, 2241-2247.
- Toutin, T. (2004): Review article: Geometric processing of remote sensing images: models, algorithms and methods. *International Journal of Remote Sensing*, 25, 1893-1924.
- Toutin, T. (2008): ASTER DEMs for geomatic and geoscientific applications: a review. *International Journal of Remote Sensing*, 29, 1855-1875.
- Tsang, L., Kong, J.A. and Shin, R.T. (1985): *Theory of Microwave Remote Sensing*. New York: Wiley-Interscience.
- Ulaby, F.T., Moore, R.K. and Fung, A.K., *Microwave remote sensing: active and passive*, Addison-Wesley Publishing Company, London [etc.], (1982).
- Werner, C., Strozzi T., U. Wegmüller, and A. Wiesmann (2002): SAR geocoding and multi-source image registration, *Proceedings of IGARSS 2002*, Toronto, Canada, 24-28 June 2002.
- Werner C., U. Wegmüller, T. Strozzi and A. Wiesmann, (2005): Precision estimation of local offsets between SAR SLCs and detected SAR images, *Proceedings of IGARSS 2005*, Seoul, Korea, 25-29 July 2005.
- WGMS (1989): World glacier inventory - Status 1988. In: Haeberli, W., Bösch, H., Scherler, K., Østrem, G. and Wallén, C. C. (eds.), *IAHS (ICSU) / UNEP / UNESCO, World Glacier Monitoring Service*, Zurich, Switzerland: 458 pp.
- Wilson, J. and Gallant, J. (2000): *Terrain Analysis, Principles and Applications*, John Wiley & Sons, Inc., New York.
- Wingham, D.J., Rapley, C.G. and Griffiths, H. (1986): New techniques in satellite altimeter tracking systems, *Proc. IGARSS'86*, 1, 185-190.
- Wingham, D.J. (1995): The limiting resolution of ice-sheet elevations derived from pulse-limited satellite altimetry. *Journal of Glaciology*, 41 (138), 413-422.
- Wingham, D.J., Ridout, A.J., Scharroo, R., Arthern, R.J. and Shum, CK. (1998): Antarctic elevation change from 1992 to 1996. *Science*, 282, 456-458.
- Wu, Q. X. (1995): A correlation-relaxation-labelling framework for computing optical flow-Template matching from a new perspective. *IEEE Transactions on Pattern Analysis and Machine Intelligence*, 17, 843-853.
- Zappa, M. and Kan, C. (2007): Extreme heat and runoff extremes in the Swiss Alps. *Natural Hazards and Earth System Sciences*, 7, 375-389.
- Zemp, M., Paul, F., Hoelzle, M. and Haeberli, W. (2008): Alpine glacier fluctuations 1850-2000: An overview and spatio-temporal analysis of available data and its representativity. In: Orlove, B., Wiegandt, E. and Luckman, B. (eds.): *Darkening Peaks: Glacier Retreat, Science, and Society*. University of California Press, Berkeley and Los Angeles, 152-167.
- Zlotnicki, V., Fu, L.L. and Patzert, W. (1989): Seasonal variability in global sea level observed with Geosat altimetry. *Journal of Geophysical Research*, 94, C12, 17959-18237.
- Zwally, H.J., Schutz, B., Abdalati, W., Absihre, J., Bentley, C., Brenner, A., et al. (2002): ICESat's laser measurements of polar ice, atmosphere, ocean and land. *Journal of Geodynamics*, 34, 405-445.

Abbreviations

ALOS	Advanced Land Observing Satellite
AOI	Area Of Interest
ASAR	Advanced SAR
ASTER	Advanced Spaceborne Thermal Emission and Reflection radiometer
CC	Correlation Coefficient
CCF	Cross Correlation in the Frequency domain
CGIAR	The Consultative Group on International Agricultural Research
CRL	Correlation Relaxation Labelling
GCP	Ground Control Point
GIS	Geographic Information System
GLIMS	Global Land Ice Measurements from Space
GNSS	Global Navigation Satellite System
GTN-G	Global Terrestrial Networks - Glaciers
DARD	Data Access Requirement Document
DEM	Digital Elevation Model
DInSAR	Differential InSAR
DMRT	Dense Medium Radiative Transfer
DN	Digital Number
DOS	Dark Object Subtraction
ECV	Essential Climate Variable
ERS	European Remote-sensing Satellite
ETM+	Enhanced Thematic Mapper plus
FCDR	Fundamental Climate Data Record
InSAR	Interferometric repeat-pass SAR
kHz	kilo Hertz
LIDAR	Laser Detection and Ranging
LOS	Line Of Sight
LRM	Low Resolution Mode
NED	National DEM
NCC	Normalized Cross-Correlation
NIR	Near-InfraRed part of the electromagnetic spectrum
NDSI	Normalized Difference Snow Index
NDVI	Normalized Difference Vegetation Index
PALSAR	Phased Array type L-band SAR



PCA	Principle Component Analysis
PSD	Product Specifications Document
RADAR	Radio Detection And Ranging
RGB	Red Green Blue
RMSE	Root Mean Square Error
RSS	Root Sum of Squares
SAR	Synthetic Aperture Radar
SB-SAR	Satellite-Borne repeat pass SAR
SLC	Single Look Complex(for SAR)
SLC-off	Scan Line Corrector off (for Landsat 7)
SNR	Signal-to-Noise Ratio
SPOT	System Pour l'Observation de la Terre
SRTM	Shuttle Radar Topography Mission
SWIR	Short Wave InfraRed
THz	Tera Hertz
TOA	Top of Atmosphere
TM	Thematic Mapper
URD	User Requirement Document
USGS	United States Geological Survey
UTM	Universal Transverse Mercator
VIS	VISible part of the electromagnetic spectrum
VNIR	Visible to Near-InfraRed part of the electromagnetic spectrum
WGI	World Glacier Inventory
WGMS	World Glacier Monitoring Service